

# Microscopic description of nuclear deformations

---

**Lotina, Luka**

**Doctoral thesis / Doktorski rad**

**2024**

*Degree Grantor / Ustanova koja je dodijelila akademski / stručni stupanj:* **University of Zagreb, Faculty of Science / Sveučilište u Zagrebu, Prirodoslovno-matematički fakultet**

*Permanent link / Trajna poveznica:* <https://um.nsk.hr/um:nbn:hr:217:069400>

*Rights / Prava:* [In copyright](#)/[Zaštićeno autorskim pravom.](#)

*Download date / Datum preuzimanja:* **2025-03-02**



*Repository / Repozitorij:*

[Repository of the Faculty of Science - University of Zagreb](#)





University of Zagreb  
Faculty of Science  
Department of Physics

Luka Lotina

# **Microscopic description of nuclear deformations**

DOCTORAL THESIS

Zagreb, 2024



University of Zagreb  
Faculty of Science  
Department of Physics

Luka Lotina

# **Microscopic description of nuclear deformations**

DOCTORAL THESIS

Supervisor:  
dr. sc. Kosuke Nomura

Zagreb, 2024



Sveučilište u Zagrebu  
Prirodoslovno-matematički fakultet  
Fizički odsjek

Luka Lotina

# **Mikroskopski opis deformacija atomske jezgre**

DOKTORSKI RAD

Mentor:  
dr. sc. Kosuke Nomura

Zagreb, 2024

# Supervisor information

Kosuke Nomura is currently an Associate Professor at the Department of Physics, Hokkaido University, Japan and a Director of the Nuclear Reaction Data Center, Hokkaido University. His research focuses on the theoretical study of low-lying nuclear structure and dynamics. He obtained a Master's Degree in 2009 and a PhD in 2012 at the University of Tokyo, Japan. He was a JSPS Fellow at the University of Tokyo (04/2009-03/2012), a JSPS Fellow for Research Abroad at the University of Cologne, Germany (04/2012-08/2013), a Marie-Curie Fellow at GANIL, CEA/CNRS, France (09/2013-08/2015), a postdoc at IPN Orsay, CNRS, France (09/2015), a postdoc at the University of Zagreb, Croatia (10/2015-03/2016 and 01/2018-11/2018), a JSPS Fellow at the University of Tsukuba, Japan (04/2016-10/2017), and Tenure-Track Researcher at the Japan Atomic Energy Agency, Japan (12/2018-04/2019). Before moving to the current position at the Hokkaido University, he was an Assistant Professor and Head of the Laboratory at the University of Zagreb (05/2019-02/2023). His PhD thesis was published by Springer Theses as a part of the Recognizing Outstanding PhD Research series. He has a total of 96 publications which were cited a total of 2,160 times, according to the Google Scholar, and he has a h-index of 25.

# Acknowledgements

This work is financed within the Tenure Track Pilot Programme of the Croatian Science Foundation and the École Polytechnique Fédérale de Lausanne, and the project TTP-2018-07-3554 Exotic Nuclear Structure and Dynamics, with funds from the Croatian-Swiss Research Programme. The author expresses gratitude to the project for funding the research as well as various trips to workshops and schools, which were very helpful.

I would like to thank my supervisor, Professor Kosuke Nomura, for being an excellent advisor, who was always supportive and ready to help with any of the problems I had encountered during my research, and who was always willing to give advice on what should be done in order to make the research better. Without his help, this thesis would not have been successfully completed. I would like to thank my institutional supervisor, Professor Tamara Nikšić for all of her help regarding the administration, as well as for helping me understand the mean-field models and codes better. I also want to thank Dr. Konstantinos Karakatsanis for providing me with the MDCRHB code and helping me learn how to use it, which was crucial for this research, and Dr. Bhoomika Maheshwari for helping me better understand the details of the IBM, which was also necessary for this work. Finally, I would like to thank my family for being extremely supportive of me throughout my life. A special thanks go to all of my close friends, who made these 4 years very fun and enjoyable.

This work is dedicated to the memory of my grandmother Ivka, who was kind and loving, and who always supported my choice of pursuing a career in physics.

# Abstract

In this thesis, a microscopic model, based on the nuclear energy density functional, which can be used to analyse hexadecapole correlations in nuclei, is constructed and presented. Using the model, axial hexadecapole deformations were explored in the rare-earth region, as well as the effects those deformations have on the low-lying energy spectra and transition strengths of even-even rare-earth nuclei. A self-consistent mean-field calculation with a relativistic energy density functional DD-PC1 was performed on even-even isotopes of Nd, Sm, Gd, Dy and Er ( $Z = 60 - 68$ ) in the  $N \approx 90$  region, with constraints on axial quadrupole and hexadecapole deformation parameters  $\beta_{20}$  and  $\beta_{40}$ . The low-lying excitation energies and transition strengths were calculated by constructing the mapped  $sdg$  interacting boson model, whose parameters were derived by fitting them to the potential energy surface from the mean-field calculation. The results show that the mapped  $sdg$  interacting boson model can be successfully constructed and applied to even-even rare-earth nuclei, and that including the hexadecapole deformations in the model is necessary in order to successfully reproduce the energies of the ( $J^\pi \geq 6^+$ ) yrast states for nuclei with the neutron number near the magic number  $N = 82$ . The description of  $B(E2)$  transitions between the higher-lying yrast states, is improved by this model, compared to the simpler model which does not include  $g$  bosons. It is also shown that the inclusion of the  $g$  boson in the interacting boson model is necessary if one wants to reproduce large  $B(E4)$  transition strengths from higher-lying  $4^+$  states to the  $0^+$  ground state, however, the experimental data on such transitions in rare-earth nuclei is limited.

Keywords: axial hexadecapole deformations, rare-earth nuclei, relativistic energy density functional,  $sdg$  interacting boson model, low-lying spectra, yrast states, transition strengths

# Prošireni sažetak

U ovom radu predstavljen je mikroskopski model, temeljen na nuklearnom energijskom funkcionalu gustoće, koji se može koristiti za analizu heksadekapolnih korelacija u atomskim jezgrama. Koristeći ovaj model, analizirane su aksijalne heksadekapolne deformacije u području rijetkih zemnih metala, kao i učinci navedenih deformacija na niskoležeći spektar pobuđenih stanja i na snage prijelaza među pobuđenim stanjima u parno-parnim jezgrama iz skupine rijetkih zemnih metala. Izračuni u okviru samokonzistentnog modela srednjeg polja, s relativističkim energijskim funkcionalom gustoće DD-PC1, provedeni su na parno-parnim izotopima Nd, Sm, Gd, Dy i Er ( $Z = 60 - 68$ ) u području oko  $N = 90$ , s ograničenjima postavljenima na aksijalne kvadrupolne i heksadekapolne deformacijske parametre  $\beta_{20}$  i  $\beta_{40}$ . Energije niskoležećih pobuđenih stanja i snage prijelaza izračunate su pomoću *sdg* modela interagirajućih bozona, pri čemu su vrijednosti parametara Hamiltonijana danog modela određene mapiranjem površine potencijalne energije, izračunate pomoću modela srednjeg polja, na Hamiltonijan modela interagirajućih bozona. Dobiveni rezultati pokazuju da se mapirani *sdg* model interagirajućih bozona može uspješno konstruirati i primijeniti na parno-parne jezgre rijetkih zemnih metala, te da je uključivanje heksadekapolnih korelacija u model interagirajućih bozona nužno da bi se uspješno reproducirale izmjerene vrijednosti energija viših stanja  $J^\pi \geq 6^+$  iz vrpce osnovnog stanja, u jezgrama s neutronske brojem blizu  $N = 82$  magičnog broja. Također, *sdg* model može uspješnije predvidjeti  $B(E2)$  snage prijelaza između viših stanja u vrpce osnovnog stanja, u usporedbi s jednostavnijim *sd* modelom. Pokazano je i da je uključivanje *g* bozona u model interagirajućih bozona nužno za izračun velikih vrijednosti  $B(E4)$  snaga prijelaza između viših  $4^+$  stanja i osnovnog stanja, međutim, veoma je malo eksperimentalnih podataka vezanih uz te prijelaze u jezgrama rijetkih zemnih metala.

Ključne riječi: aksijalne heksadekapolne deformacije, jezgre rijetkih zemnih metala, relativistički energijski funkcional gustoće, *sdg* model interagirajućih bozona, niskoležeći spektar pobuđenih stanja, vrpca osnovnog stanja, snage prijelaza



## Uvod

Atomska jezgra je kompleksni kvantni višestruki sustav sastavljen od protona i neutrona koji primarno međudjeluju putem jake sile, pri čemu nezanemarljiv utjecaj na procese u jezgri imaju i elektroslaba te Coulombova sila. S obzirom na kompleksnost navedenog sustava, često se koriste teorijski modeli koji izbjegavaju direktno modeliranje sila. Jedan od najpopularnijih takvih modela je model ljusaka [1, 2], koji aproksimira jezgru kao sustav nukleona kvantiziranih energija, pri čemu se svaki od nukleona nalazi u određenoj "ljusci". Jezgre kojima su sve ljuske potpuno popunjene, nazivaju se dvostruko-magičnim jezgrama i karakterizira ih to da su jače vezane u odnosu na susjedne jezgre i da su sferičnog oblika u osnovnom stanju. Model ljusaka je jednočestični model u kojem se pobuđena stanja opisuju preko pomicanja nukleona u više ljuske.

Osim jednočestičnih pobuđenja, kolektivna pobuđenja, opisana preko deformacija oblika jezgre u odnosu na sferični oblik, također igraju važnu ulogu u stvaranju pobuđenih stanja [3, 4]. Deformacije jezgara tema su brojnih eksperimentalnih istraživanja [5–8], te predstavljaju iznimno važnu temu u nuklearnoj fizici. Najčešći oblik deformacija koje se javljaju u jezgrama su kvadrupolne deformacije, aksijalne prolatne, aksijalne oblatne te triaksijalne, koje utječu na energije pobuđenih stanja pozitivnog pariteta [9]. Drugi red deformacija koje utječu na stanja pozitivnog pariteta su heksadekapolne deformacije, čiji su efekti često zasjenjeni jakim kvadrupolnim efektima, no njihova prisutnost je ipak opažena u mnogim jezgrama, od rasponu od lakih do teških [10–19]. Glavni efekti heksadekapolnih korelacija u parno-parnim jezgrama su pojava  $K^\pi = 4^+$  vrpce u niskoležećem spektru pobuđenih stanja, te jake  $B(E4)$  snage prijelaza iz navedenih  $4^+$  stanja u osnovno stanje. Osim toga, heksadekapolne deformacije bi, prema teorijskim predviđanjima, trebale igrati važnu ulogu u brojnim reakcijama koje su predmet proučavanja u nuklearnoj fizici [19–21]. S obzirom na navedeno, teorijsko proučavanje heksadekapolnih korelacija u jezgrama vrlo je važno, posebice u okviru tzv. mikroskopskih modela, koji svojstva jezgre proučavaju na temelju nekih fundamentalnih međunukleonskih interakcija ili putem nukleonskih gustoća [22]. Posebna vrsta mikroskopskih modela su samokonzistentni modeli srednjeg polja (SCMF modeli) koji koriste energijske funkcionalne gustoće (EDF) [23]. Posebna vrsta SCMF modela su relativistički modeli srednjeg polja (RMF) koji koriste relativističke EDF-ove (REDF) [24, 25], kombinirane s relativističkom Hartree-Bogoliubovljevom teorijom kojom se opisuju korelacije sparivanja u jezgrama [26]. Ono što takav model omogućuje je izračun površine potencijalne energije (PES), gdje je energija jezgre prikazana kao funkcija odabranih deformacijskih parametara.

S obzirom da SCMF izračuni nužno vode do slamanja određenih simetrija, ne mogu se

samostalno koristiti za izračun energija pobuđenih stanja i snaga prijelaza, već se moraju kombinirati s drugim modelima, npr. metodom generirajućih koordinata (GCM) [27] ili kolektivnim Hamiltonijanom [28–30]. Model kojim se bavi ovaj rad je model interagirajućih bozona (IBM) [31], u kojem je jezgra aproksimirana kao sustav koji se sastoji od dvostruko magične sredice i valentnih nukleona uparenih u bozone. U standardnom IBM-u nukleoni se uparuju u  $s$ , ( $J^\pi = 0^+$ ) i  $d$  ( $J^\pi = 2^+$ ) bozone, te se ovakav model može uspješno koristiti za opise kvadrupolnih korelacija u jezgrama [32–35]. Za uključivanje heksadekapolnih korelacija u IBM potrebno je uvesti  $g$  bozon ( $J^\pi = 4^+$ ). Ovakvo proširenje modela pokazalo se nužnim za opisivanje nekih svojstava niskoležećeg spektra u određenim jezgrama [35–40].

Premda je  $sdg$ -IBM detaljno proučavan kao fenomenološki model, dosada još nije pokušano izvesti parametre  $sdg$ -IBM Hamiltonijana iz mikroskopskog modela. Koristeći nedavno osmišljenu metodu mapiranja [41–47], parametri  $sdg$ -IBM Hamiltonijana izvedeni su mapiranjem PES, izračunatih u okviru RMF modela s DD-PC1 funkcionalom gustoće [24, 48] s ograničenjima postavljenima na aksijalne kvadrupolne i heksadekapolne deformacijske parametre, na  $sdg$ -IBM Hamiltonijan. Model je primijenjen na parno-parne jezgre  $^{144-156}\text{Nd}$ ,  $^{146-158}\text{Sm}$ ,  $^{148-160}\text{Gd}$ ,  $^{150-162}\text{Dy}$  i  $^{152-164}\text{Er}$ , koje su odabrane zbog činjenice da nema značajne prisutnosti triaksijalnih kvadrupolnih korelacija u danim jezgrama [42, 49]. Izračunate energije i snage prijelaza uspoređene su s rezultatima jednostavnijeg modela  $sd$ -IBM, kao i sa eksperimentalnim podacima s NNDC stranice [50].

## Teorijski okvir

Deformacije se mogu uvesti putem parametrizacije radijusa, zadane u jednadžbi (2.1). Ako se uzmu u obzir samo aksijalne ( $\mu = 0$ ) deformacije, tada kvadrupolnim deformacijama odgovara  $\lambda = 2$ , oktupolnim deformacijama [51] odgovara  $\lambda = 3$ , a heksadekapolnim  $\lambda = 4$ . Navedene deformacije prikazane su na Slici 2.1.

## RMF model

Teoriju funkcionala gustoće (DFT) utemeljili su Hohenberg i Kohn za potrebe opisivanja svojstava nehomogenog elektronskog plina [52]. Kohn i Sham proširili su DFT na općeniti kvantni sustav više čestica [53]. SCMF predstavlja analog Kohn-Shamovoj teoriji za jezgre. U RMF modelima, energijski funkcional zadan je preko Lagranžijana [24, 54, 55] iz jednadžbe (2.8), iz kojeg se variranjem po spinoru  $\bar{\psi}$  može dobiti jednonukleonska Diracova jednadžba (2.9). Funkcional DD-PC1 konstruiran je tako da su 3 parametra  $\alpha_{S,V,TV}$  izražena preko 9 parametara

čije su vrijednosti namještene tako da se mogu uspješno reproducirati eksperimentalni podaci o masama jezgara [56]. Korelacije sparivanja uključuju se u izračune putem RHB modela, u kojem se osnovno stanje jezgre aproksimira kvazičestičnim vakuumom. Energije sparivanja izvode se iz Dirac-Hartree-Bogoliubovljeve jednadžbe (2.21) [54], pri čemu se polje sparivanja, definirano u jednadžbi (2.22), konstruira preko tenzora sparivanja  $\kappa$  i efektivne interakcije  $V^{pp}$ , definiranim u jednadžbama (2.23) i (2.25). Konačno, ograničenja na deformacijske parametre se postavljaju preko jednadžbi (2.33 - 2.36) [54, 55], koje se rješavaju iterativno, dok ne dođe do konvergenije. Nedavno su razvijeni modeli s višedimenzionalnim ograničenjima (MDC-RMF modeli) [54, 55, 57, 58], koji omogućuju provođenje RMF izračuna s ograničenjima postavljenima na veliki broj deformacijskih parametara, uključujući aksijalne kvadrupolne i aksijalne heksadekapolne parametre. U ovom radu, RMF izračuni provedeni su s ograničenjima na prethodno spomenute parametre, te su kao konačan rezultat dobivene PES u prostoru aksijalnih kvadrupolnih i heksadekapolnih deformacijskih parametara.

## IBM

U IBM-u, bozonske interakcije izražene su preko tenzorskih produkata [59], prikazanih u jednadžbama (2.39, 2.40). U *sd*-IBM-u, 36 tenzorskih produkata čini generatore grupe  $U(6)$  [31]. Ukoliko se pretpostave određeni simetrijski limiti, Hamiltonijan IBM-a može se prikazati preko Casimirovih operatora grupa i podgrupa u određenom simetrijskom lancu [60]. U *sd*-IBM-u, simetrijski lanci su  $U(5)$ ,  $SU(3)$  i  $O(6)$  [31, 45], prikazani u jednadžbama (2.43 - 2.48). Uz pretpostavku spomenutih simetrijskih lanaca, za *sd*-IBM Hamiltonijan može se odabrati onaj definiran jednadžbama (2.49, 2.50). U *sdg*-IBM-u, 225 tenzorskih produkata generira grupu  $U(15)$  [31]. Simetrijski limiti koji se najčešće razmatraju u *sdg*-IBM-u su  $[U(6) \supset U(5)] \otimes U(9)$ ,  $SU(3)$  i  $O(15)$  [61–64], predstavljeni u jednadžbama (2.52-2.57). Odabrani *sdg*-IBM Hamiltonijan definiran je u jednadžbama (2.61-2.63) i sličan je Hamiltonijanu iz [65].

Kvadrupolne, heksadekapolne i monopolne [66] snage prijelaza u IBM-u, definirane su jednadžbama (2.64-2.70). Pri izračunu kvadrupolnih i heksadekapolnih snaga prijelaza, vrijednosti efektivnih naboja se namještaju tako da se mogu uspješno reproducirati snage prijelaza iz  $2_1^+$  i  $4_1^+$  stanja u vrpici osnovnog stanja, u  $0_1^+$  osnovno stanje. Vrijednosti parametara u monopolnim prijelazima fiksirane su za sve jezgre po uzoru na [66].

## Nukleon-bozon mapiranje

IBM se može povezati s geometrijskim modelom, u kojem je energija predstavljena kao funkcija deformacijskih parametara, putem tzv. bozonskih koherentnih stanja [67–70]. Očekivana vri-

jednost *sd*-IBM Hamiltonijana u koherentnom stanju dana je u jednadžbi (2.75) [71, 72], koja se, ukoliko se pretpostavi da nema triaksijalnih deformacija, svodi na jednadžbu (2.76).

U *sdg*-IBM-u, bozonsko koherentno stanje definirano je jednadžbom (2.77). Za razliku od *sd*-IBM koherentnog stanja, ovdje se javljaju i aksijalni heksadekapolni parametar te dva triaksijalna heksadekapolna parametra [73]. Da bi se pojednostavnio izraz za osnovno stanje, triaksijalni heksadekapolni deformacijski parametri mogu se izraziti preko triaksijalnog kvadrupolnog deformacijskog parametra [74]. Koherentno stanje u tom slučaju poprima oblik prikazan u jednadžbi (2.78) [65]. Očekivana vrijednost Hamiltonijana iz jednadžbe (2.61), u koherentnom stanju, dana je u jednadžbi (2.80).

U metodi nukleon-bozon mapiranja, vrijednosti parametara IBM Hamiltonijana namještaju se tako da PES dobiven iz IBM-a aproksimira PES dobiven iz RMF modela što je bolje moguće. Pri tome je pokazano da se bozonski i fermionski deformacijski parametri mogu povezati linearno, kao što je prikazano u jednadžbi (2.82) [41, 42, 45, 47]. Ilustrativni prikaz metode mapiranja nalazi se na Slici 2.2.

## Rezultati

U ovom poglavlju predstavljeni su rezultati dobiveni putem mapiranog *sdg*-IBM-a, koji su uspoređeni s rezultatima dobivenima pomoću jednostavnijeg *sd*-IBM-a te s eksperimentalnim podacima [50]. SCMF izračuni provedeni su uz pomoć koda MDCRHB [54], dok je za IBM izračune korišten kod ARBMODEL [75].

### SCMF izračuni i metoda mapiranja

PES izotopa  $^{144-154}\text{Nd}$ ,  $^{146-156}\text{Sm}$ ,  $^{148-158}\text{Gd}$ ,  $^{150-160}\text{Dy}$  i  $^{152-162}\text{Er}$ , dobiveni preko SCMF izračuna, prikazani su na Slikama 3.1-3.5. Slike se mogu pronaći i u radu [76]. Dobiveni SCMF rezultati konzistentni su s prijašnjim SCMF izračunima u području rijetkih zemnih elemenata [74, 77, 78]. Izračuni za Gd izotope mogu se pronaći i u radu [79]. IBM aproksimacije SCMF izračuna mogu se pronaći na Slikama 3.6-3.10. Iz navedenih slika vidljivo je da *sdg*-IBM zadovoljavajuće aproksimira SCMF izračune te uspješno reproducira neka od svojstava, kao što su položaj apsolutnog minimuma, položaj sedlene točke u području oblatnih kvadrupolnih deformacija  $\beta_2 < 0$ , te općeniti izgled PES za pojedinu jezgru. Vrijednosti parametara *sdg*-IBM Hamiltonijana prikazane su kao funkcije broja valentnih bozona  $N_B$  na Slici 3.11. Parametar  $\sigma$  nije prikazan jer on iznosi  $\sigma = 3.5$  u  $^{144,146}\text{Nd}$  i  $^{146,148}\text{Sm}$ , te  $\sigma = 2.8$  u preostalim Nd i Sm izotopima. Što se tiče težih jezgara, vrijednost parametra iznosi  $\sigma = 1.0$  u svim Gd, Dy i Er

izotopima.

Rezultati mapiranja SCMF izračuna po  $\beta_4 = 0$  liniji na *sd*-IBM Hamiltonijan prikazani su na slikama 3.12-3.16. Iz priloženih slika vidljivo je da *sd*-IBM dobro aproksimira SCMF izračune, te su uspješno reproducirani položaj apsolutnog minimuma, položaj i energija sedlene točke u području oblatnih deformacija, i energija maksimuma u položaju  $\beta_2 = 0$ . Parametri *sd*-IBM Hamiltonijana prikazani su kao funkcija broja valentnih bozona na Slici 3.17.

## Rezultati spektroskopskih izračuna

Na Slici 3.18 prikazane su energije stanja  $2^+ - 14^+$  iz vrpce osnovnog stanja kao funkcija broja neutrona  $N$ . Iz slike je vidljivo da *sdg*-IBM značajno poboljšava opis energija  $J^\pi \geq 6^+$  stanja u odnosu na *sd*-IBM u  $N = 84, 86$  jezgrama. U izotopima Nd i Sm, poboljšanja su vidljiva i u težim jezgrama s neutronske brojevima  $N \geq 90$ . Tablica 3.1 prikazuje  $R_{4/2}$  omjere energija  $4^+$  i  $2^+$  stanja u  $N = 84, 86$  jezgrama. Iz tablice je vidljivo da *sdg*-IBM može uspješno predvidjeti omjere  $R_{4/2} < 2$  u  $N = 84$  jezgrama, za razliku od *sd*-IBM-a. U  $N = 86$  jezgrama, omjeri postaju veći od 2, te *sdg*-IBM samo donekle bolje predviđa vrijednosti omjera u odnosu na *sd*-IBM u tim jezgrama. Činjenica da *sdg*-IBM poboljšava izračune energija određenih stanja i  $R_{4/2}$  omjera može se objasniti time da je prisutnost  $g$  bozona predviđena u valnim funkcijama tih stanja, kao što se može vidjeti na Slici 3.19. Također, činjenica da kolektivni model, kao što je *sdg*-IBM, može dobro opisati energije u vrpce osnovnog stanja u sferično-vibracijskim jezgrama, pokazuje da ovakav kolektivni model može uzeti u obzir i jednočestična pobuđenja koja su očekivana u takvim jezgrama. Treba napomenuti i da su, prema drugim teorijskim izračunima, stanja  $2_1^+$  i  $4_1^+$  u nekim  $N = 84$  jezgrama, poput  $^{144}\text{Nd}$  i  $^{146}\text{Sm}$ , predviđena kao stanja kolektivne prirode [80].

Slika 3.20 prikazuje stanja  $0_2^+$ ,  $2_3^+$  i  $4_3^+$ , koja čine  $0^+$  vrpcu u deformiranim jezgrama, kao funkcije neutronske broja  $N$ . Kao što se može vidjeti iz slike, *sdg*-IBM ne daje značajno različite rezultate od *sd*-IBM-a za ovu vrpcu. Energije stanja  $2_3^+$  i  $4_3^+$  su bliže eksperimentalnim vrijednostima u  $N = 84, 86$  jezgrama, no činjenica da *sdg*-IBM predviđa da su te energije gotovo jednake u navedenim jezgrama nije u skladu s eksperimentalnim podacima.

Slika 3.21 prikazuje stanja  $2_2^+$ ,  $3_1^+$  i  $4_2^+$ , koja čine  $\gamma$ -vibracijsku vrpcu u deformiranim jezgrama, kao funkcije neutronske broja  $N$ . Ono što se može vidjeti sa slike je da *sdg*-IBM ne poboljšava opis energija navedenih stanja, te u jezgrama blizu  $N = 82$  zatvorene neutronske ljuske, predviđa vrlo niska  $4_2^+$  stanja, energetske vrlo bliska  $2_2^+$  stanjima, što nije u skladu s izmjerenim podacima.

Slika 3.22 prikazuje vrijednosti  $e_2^{sdg, sd}$  i  $e_4^{sdg, sd}$  efektivnih naboja za kvadrupolne i heksadekapolne prijelaze kao funkcije broja valentnih bozona  $N_B$ . Vrijednosti kvadrupolnih efek-

tivnih naboja namještene su da bi se uspješno reproducirala  $B(E2; 2^+ \rightarrow 0^+)$  snaga prijelaza u vrpici osnovnog stanja, dok su vrijednosti heksadekapolnih efektivnih naboja namještene tako da se uspješno reproducira  $B(E4; 4^+ \rightarrow 0^+)$  snaga prijelaza u istoj vrpici. Vrijednosti  $e_2^{sdg}$  i  $e_2^{sd}$  ne razlikuju se značajno, što se može objasniti činjenicom da u  $2^+$  stanju nije predviđena značajna prisutnost  $g$  bozona. S druge strane,  $e_4^{sdg}$  i  $e_4^{sd}$  se značajno razlikuju, posebice u  $N \leq 88$  jezgrama gdje  $sd$ -IBM predviđa iznimno velike i nefizikalne vrijednosti  $e_4^{sd}$  efektivnih naboja. Ovo potvrđuje nužnost uključivanja  $g$  bozona u izračune  $B(E4)$  snaga prijelaza.

Na Slici 3.23 prikazane su  $B(E2)$  snage prijelaza u vrpici osnovnog stanja u  $N = 90, 92$  jezgrama. U jezgrama Nd i Sm,  $sdg$ -IBM bolje opisuje prijelaze između  $J^\pi \geq 6^+$  stanja u odnosu na  $sd$ -IBM, što se može ponovno objasniti gledajući prisutnost  $g$  bozona u tim stanjima na Slici 3.19, kao i činjenicom da su vrijednosti parametra  $\sigma$  prilično velike u tim izotopima, zbog čega  $(d^\dagger \times \tilde{g} + g^\dagger \times \tilde{d})^{(2)}$  član u operatoru  $\hat{Q}^{(2)}$  iz jednadžbe (2.62) ima značajan doprinos u izračunu  $B(E2)$  snaga prijelaza. U jezgrama Gd, Dy i Er nema značajnijih razlika između dva modela, te su također velike vrijednosti pogrešaka u eksperimentalnim podacima, što onemogućava da se precizno odredi koji od dva modela bolje predviđa snage prijelaza u navedenim jezgrama.

Slika 3.24 prikazuje  $B(E4; 4_n^+ \rightarrow 0^+)$  snage prijelaza iz  $4_{n=1,2,3,4}^+$  stanja u osnovno stanje  $0^+$ , kao funkcije broja nukleona  $A$ . Značajna razlika između  $sdg$ - i  $sd$ -modela je u tome što  $sdg$ -IBM može predvidjeti jake snage prijelaza iz  $4_{n \geq 2}^+$  stanja u  $0^+$  osnovno stanje. To odgovara činjenici da heksadekapolne korelacije u jezgri uzrokuju nastajanje  $K^\pi = 4^+$  vrpce s jakim  $B(E4)$  snagama prijelaza u osnovno stanje, što model koji razmatra isključivo kvadrupolne korelacije ne može predvidjeti.

Na Slici 3.25 prikazane su kvadrirane monopolne snage prijelaza  $\rho^2(E0; 0_i^+ \rightarrow 0_j^+)$  kao funkcije broja neutrona  $N$ , pri čemu vrijedi  $i = 2, 3$  te  $j = 1, 2$ . Izračuni su prikazani za izotope Sm i Gd. Eksperimentalni podaci preuzeti su iz [50, 81]. Iz navedene slike može se vidjeti da  $sdg$ -IBM donekle poboljšava snagu  $0_3^+ \rightarrow 0_2^+$  prijelaza u  $^{152}\text{Sm}$ , kao i snagu  $0_3^+ \rightarrow 0_1^+$  prijelaza u  $^{158}\text{Gd}$ , te da dalje od toga nema značajnijih razlika između 2 modela.

## Zaključak

Ovaj rad predstavlja prvi pokušaj da se sistematski proučavaju efekti aksijalnih kvadrupolnih i heksadekapolnih efekata u jezgrama, u okviru mikroskopskog modela. Pokazano je da se  $g$  bozon može uključiti mikroskopski u IBM, pomoću metode nukleon-bozon mapiranja. Model je primijenjen na parno-parne jezgre Nd, Sm, Gd, Dy i Er, te je pokazano da  $sdg$ -IBM pruža neka značajna poboljšanja u odnosu na jednostavniji  $sd$ -IBM. Kao prvo, izračunate energije  $J^\pi \geq 6^+$ , iz vrpce osnovnog stanja, se značajno bolje slažu s izmjerenim podacima u  $N \leq 88$  jezgrama

u odnosu na one dobivene pomoću *sd*-IBM-a, te je također pokazano da *sdg*-IBM poboljšava izračunate omjere energija  $R_{4/2}$  između prvih dvaju stanja iz osnovne vrpce u  $N = 84$  jezgrama. Demonstrirano je i da navedeni model poboljšava opis  $B(E2)$  snaga prijelaza u vrpci osnovnog stanja između  $J^\pi \geq 6^+$  stanja u  $N = 90, 92$  jezgrama, te da model može u jezgrama predvidjeti postojanje  $K^\pi = 4^+$  vrpce s izraženim  $B(E4)$  snagama prijelaza u osnovno stanje. S druge strane, model ne daje značajna poboljšanja u odnosu na jednostavniji *sd*-IBM u opisu stanja  $0^+$  vrpce i  $\gamma$ -vibracijske vrpce. To je i očekivano s obzirom da su heksadekapolni efekti često zasjenjeni jakim kvadrupolnim efektima. Unatoč tome, ovaj rad pokazuje da je uključivanje heksadekapolnih korelacija nužno za precizno opisivanje mnogih svojstava atomske jezgre, te da bi njihovo uključivanje trebalo predstavljati integralni dio bilo kojeg teorijskog proučavanja kojem je cilj postići precizan opis energija i snaga prijelaza u rijetkim zemnim elementima.

U budućnosti, ovaj model može se proširiti tako da se omogući opisivanje svojstava neparno-parnih i neparno-neparnih jezgara. To bi moglo omogućiti i proučavanje utjecaja heksadekapolnih korelacija na  $\beta$ -raspade u području rijetkih zemnih jezgara. Model se također može proširiti tako da se u korelacije uključe i triaksijalne kvadrupolne korelacije. Takav model mogao bi biti primijenjen na izotope Pt i Os te na aktinide. Konačno, navedeni model može biti proširen u *sdg*-IBM-2, u kojem su protonski i neutronski bozoni promatrani kao različite čestice. Takav model mogao bi se koristiti za proučavanje fenomena koji su nedostupni modelima kao što je IBM-1, primjerice, tzv. "modovi škara" (scissor modes).

# Contents

<b>1</b>	<b>Introduction</b>	<b>1</b>
<b>2</b>	<b>Theoretical framework</b>	<b>6</b>
2.1	Quadrupole and hexadecapole deformations . . . . .	6
2.2	Relativistic mean field models . . . . .	7
2.3	The interacting boson model, <i>sd</i> and <i>sdg</i> . . . . .	12
2.3.1	<i>sd</i> -IBM . . . . .	13
2.3.2	<i>sdg</i> -IBM . . . . .	15
2.3.3	Electric transitions in the IBM . . . . .	18
2.4	Nucleon-to-boson mapping . . . . .	20
2.4.1	Geometric interpretation of the <i>sd</i> -IBM . . . . .	20
2.4.2	Geometric interpretation of the <i>sdg</i> -IBM . . . . .	21
2.4.3	The mapping method . . . . .	23
<b>3</b>	<b>Results</b>	<b>25</b>
3.1	SCMF calculations and the mapping method . . . . .	25
3.1.1	SCMF calculations . . . . .	25
3.1.2	Mapping the SCMF calculations onto the <i>sdg</i> -IBM space . . . . .	29
3.1.3	Mapping the SCMF calculations onto the <i>sd</i> -IBM space . . . . .	34
3.2	Results of the spectroscopic calculations . . . . .	38
3.2.1	Excitation energies . . . . .	39
3.3	Transition strengths . . . . .	45
3.3.1	Effective charges . . . . .	45
3.3.2	Quadrupole transitions . . . . .	46
3.3.3	Hexadecapole transitions . . . . .	49
3.3.4	Monopole transitions . . . . .	49
<b>4</b>	<b>Thesis summary and outlook</b>	<b>52</b>
4.1	Summary of this Thesis . . . . .	52
4.2	Outlook . . . . .	53
	<b>Curriculum vitae</b>	<b>62</b>



# List of Figures

2.1	The most common axial nuclear deformations. From left to right, first row: quadrupole deformation, octupole deformation. Second row: positive hexadecapole deformation, negative hexadecapole deformation. Figure is taken from Ref. [4]. . . . .	7
2.2	An illustration of the mapping method in the axial quadrupole-hexadecapole plane. The SCMF PES is shown on the left, and the IBM approximation of the SCMF PES is shown on the right. The energy is shown up to 3 MeV. . . . .	24
3.1	Axially-symmetric quadrupole ( $\beta_{20}$ ) and hexadecapole ( $\beta_{40}$ ) constrained energy surfaces for the $^{144-154}\text{Nd}$ isotopes calculated within the relativistic Hartree-Bogoliubov method using the DD-PC1 energy density functional and the pairing force of finite range. Energy difference between neighbouring contours is 0.1 MeV, and the absolute minimum is indicated by an open triangle. Figure is taken from Ref. [76] . . . . .	26
3.2	Same as the caption for Fig. 3.1, but for $^{146-156}\text{Sm}$ . . . . .	27
3.3	Same as the caption for Fig. 3.1, but for $^{148-158}\text{Gd}$ . SCMF calculations for Gd can also be found in Ref. [79]. . . . .	27
3.4	Same as the caption for Fig. 3.1, but for $^{150-160}\text{Dy}$ . . . . .	28
3.5	Same as the caption for Fig. 3.1, but for $^{152-162}\text{Er}$ . . . . .	28
3.6	The <i>sdg</i> -IBM axially-symmetric quadrupole ( $\beta_{20}$ ) and hexadecapole ( $\beta_{40}$ ) PESs of $^{144-154}\text{Nd}$ isotopes. The energies are shown up to 2.7 MeV, and the energy difference between the neighbouring contours is 0.1 MeV. Figure is taken from Ref. [76]. . . . .	30
3.7	Same as the caption for Fig. 3.6, but for $^{146-156}\text{Sm}$ . . . . .	31
3.8	Same as the caption for Fig. 3.6, but for $^{148-158}\text{Gd}$ . The <i>sdg</i> -IBM PES calculations for Gd can also be found in Ref. [79]. . . . .	31
3.9	Same as the caption for Fig. 3.6, but for $^{150-160}\text{Dy}$ . . . . .	32
3.10	Same as the caption for Fig. 3.6, but for $^{152-162}\text{Er}$ . . . . .	32
3.11	Parameters of the <i>sdg</i> -IBM Hamiltonian of Eq. (2.61), and the $C_2, C_4$ parameters relating fermionic and bosonic deformation parameters. The figure can be found in Ref. [76]. . . . .	33

3.12	The energies of the SCMF calculations (solid black line) and $sd$ -IBM approximations of those energies (solid red line), as functions of the axial quadrupole deformation parameter $\beta_2$ for $^{144-154}\text{Nd}$ isotopes. The energies are shown up to 14 MeV. . . . .	35
3.13	Same as the caption for Fig. 3.12, but for $^{146-156}\text{Sm}$ . . . . .	36
3.14	Same as the caption for Fig. 3.12, but for $^{148-158}\text{Gd}$ . . . . .	36
3.15	Same as the caption for Fig. 3.12, but for $^{150-160}\text{Dy}$ . . . . .	37
3.16	Same as the caption for Fig. 3.12, but for $^{152-162}\text{Er}$ . . . . .	37
3.17	Parameters of the $sd$ -IBM Hamiltonian of Eq. (2.49), and the $C_2$ parameter relating the fermionic and bosonic $\beta_2$ deformation parameter. The figure can be found in Ref. [76]. . . . .	38
3.18	Calculated excitation energies of the yrast band states up to spin $J^\pi = 14^+$ as functions of the neutron number $N$ within the mapped $sdg$ -IBM (left column) and $sd$ -IBM (right column), represented by solid symbols connected by solid lines. Experimental data are taken from Ref. [50], and are depicted as open symbols connected by dotted lines. The figure is taken from Ref. [76]. . . . .	40
3.19	The expectation value of the $g$ boson number operator $\hat{n}_g$ in yrast band states up to $J^\pi = 14^+$ , plotted as a function of the neutron number $N$ . . . . .	41
3.20	Same caption as Figure 3.18, but for the $0_2^+, 2_3^+$ and $4_3^+$ states. . . . .	43
3.21	Same caption as Figure 3.18, but for the $2_2^+, 3_1^+$ and $4_2^+$ states. . . . .	44
3.22	First row: The values of the quadrupole effective charges $e_2^{sdg}$ (left) and $e_2^{sd}$ (right). Second row: The values of the hexadecapole effective charges $e_4^{sdg}$ (left) and $e_4^{sd}$ (right). All effective charges are plotted as a function of the valence boson number $N_B$ . . . . .	47
3.23	$B(E2)$ transition strengths in the ground state band of the well-deformed $N = 90$ (left) and $N = 92$ (right) isotopes as functions of spin $J$ , calculated with the mapped $sdg$ -IBM (solid curves) and $sd$ -IBM (dotted curves). The experimental data, represented by solid circles, are adopted from Ref. [50]. The figure is taken from Ref. [76]. . . . .	48
3.24	$B(E4)$ transition strengths in W.u. for transitions between the first (panels (a) and (b)), second (panels (c) and (d)), third (panels (e) and (f)) and the fourth (panels (g) and (h)) $4^+$ states and the $0^+$ ground state, plotted as functions of the nucleon number $A$ . The $sdg$ -IBM results are shown in the left column, while the $sd$ -IBM results are shown in the right column. The experimental data, represented by solid circles, are adopted from Refs. [14–16, 50]. The figure is taken from Ref. [76]. . . . .	50
3.25	Squared values of the monopole strengths $\rho^2(E0; 0_i^+ \rightarrow 0_j^+)$ in Sm and Gd isotopes, plotted as functions of the neutron number $N$ . The experimental data, represented by solid circles, are taken from Refs. [50, 81]. The figure is taken from Ref. [76]. . . . .	51

# List of Tables

3.1	Energy ratios $R_{4/2} = E_x(4_1^+)/E_x(2_1^+)$ for $N=84$ and 86 isotones calculated with the mapped $sd$ - and $sdg$ -IBM, and compared to the experimental values [50]. The table is taken from Ref. [76]. . . . .	42
-----	---	----

# Chapter 1

## Introduction

The atomic nucleus represents a complex quantum many-body system, composed of protons and neutrons, which interact via a strong nuclear force that has a very complex form. Aside from the strong force, the weak and the electromagnetic force also play an important role in nuclear interactions. Due to such complexity of the system, describing various nuclear properties, e.g. excitation energy spectra and transitions, becomes a complicated task. In order to avoid the explicit modelling of forces inside the nucleus, various models are developed. One of the most important models of nuclear structure, developed in the last century, is the shell model [1, 2]. In the shell model, a nucleus is approximated as a system of independent nucleons moving in an average potential, with the energies being quantized, such that each nucleon occupies a particular nuclear orbital, called a shell. The nuclei with nucleon numbers corresponding to the so-called "magic numbers" 2, 8, 20, 28, 50, 82 and 126, have completely filled shells, making them more stable and harder to excite compared to their neighbouring nuclei. These nuclei are called magic nuclei, or double-magic nuclei, if both proton and neutron numbers are magic, and are characterized by a spherical shape in the ground state. The shell model is a single-particle model, which means that the excited states are described by nucleons moving up from the shells they occupied in the ground state, to the shells above.

Aside from single-particle excitations, collective modes are known to play an important role in describing nuclear properties, particularly in nuclei with non-magic nucleon numbers and exotic nuclei [3, 4]. As was mentioned before, the magic nuclei are characterized by a spherical shape in the ground state. If more nucleons are added or subtracted, or if enough energy is added to the system, deformations from the spherical shape can occur. These deformations represent the collective modes of motion in the nucleus, and are among the most important topics of research in nuclear physics today. Experiments researching deformations in various nuclei, from light to superheavy are performed at some of the world-leading laboratory facilities for

nuclear and particle physics, such as ISOLDE CERN in Switzerland [5], RIKEN RIBF in Japan [6, 7] and TRIUMF in Canada [8]. This provides a good reason to develop theoretical models that examine deformations in nuclei and predict their effects on various nuclear properties.

The most common type of nuclear deformation present in the nucleus is the quadrupole deformation. The quadrupole deformations can be divided into axial quadrupole and triaxial quadrupole shapes, with axial shapes further divided into prolate (rugby ball shape) and oblate (discus shape). The quadrupole correlations have been extensively studied, and their effects on the positive parity states and electromagnetic transitions between them in the low-lying excitation energy spectrum of nuclei is well known [9]. The next leading order of deformations that affect positive parity states, the hexadecapole deformations, have been much less studied, due to the fact that their effects on the low-lying excitation spectra of a nucleus are often overshadowed by large quadrupole effects. Nevertheless, the presence of hexadecapole deformations has been observed in a wide range of nuclei, including light nuclei [10, 11], rare-earth nuclei [12–16], and actinides [17–19]. The most pronounced effect of hexadecapole deformations in nuclei is the appearance of the low-lying  $K^\pi = 4^+$  band in even-even nuclei, with an enhanced  $B(E4; 4^+ \rightarrow 0^+)$  transition strength from the  $4^+$  state to the ground state. Another important effect of hexadecapole deformations can be observed in even-even rare-earth nuclei with the neutron number being near  $N = 82$  shell closure. In these nuclei, the ratio between the energies of the ground state band states  $4^+$  and  $2^+$ ,  $R_{4/2} = E_x(4^+)/E_x(2^+)$  is less than 2 in value. Besides the two main effects, hexadecapole deformations were observed to play a role in heavy ion collisions at the Relativistic Heavy Ion Collider [19], and are predicted to play a role in fission [20] and in the predicted neutrinoless double beta decay [21].

The fact that hexadecapole correlations have some significant effects on properties of the nucleus provides a good reason for a theoretical study of such correlations, particularly in the framework of a microscopic model, which starts from some fundamental nucleon-nucleon (NN) interaction and builds the properties of a nucleus in a self-consistent way [22]. A special class of microscopic models are the self-consistent mean-field (SCMF) models, which avoid explicitly modelling the NN interaction by approximating the nucleus as a system of independent nucleons moving in a self-consistent potential which corresponds to the actual density distribution of a given nucleus [23]. SCMF models use an energy density functional (EDF), approximated with powers and gradients of the ground state nucleon densities [24]. A special class of SCMF models are the relativistic mean-field (RMF) models, which use a relativistic energy density functional (REDF) based on the framework of quantum hadrodynamics (QHD) [24]. The RMF models have been successfully applied in describing various nuclear properties, e.g. charge radii, binding energies, neutron separation energies etc., in a wide spectrum of nuclei, ranging

from those in the valley of  $\beta$ -stability to exotic nuclei [25]. In description of open shell nuclei, the RMF models have been improved by the development of the relativistic Hartree-Bogoliubov (RHB) model, that takes into account the pairing correlations in those nuclei [26]. The important feature of the RMF models with REDFs to this work is their ability to describe the energy of a nucleus as a function of deformation parameters, by calculating the potential energy surface (PES) in the plane of deformation parameter values. Details of this model will be described in Chapter 2.

Since SCMF models necessarily break several symmetries, e.g. translational and rotational, they alone cannot be used to calculate properties such as the low-lying excitation energy spectra and transition strengths. To restore broken symmetries and enable the calculation of aforementioned properties, the most effective symmetry restoring method to use is the generator coordinate method (GCM), which generates intrinsic wave functions from the calculated multipole moments [27]. However, due to the complexity of the GCM, the calculations can be extremely time-consuming, which presents a problem when the calculation of the complete low-lying spectra is required. To solve this problem, the GCM calculations are often replaced with simpler models, such as the collective Hamiltonian models, which make use of deformation parameter values, derived from the SCMF calculations, to calculate energies and transition strengths [28–30]. Another very successful model in describing excitation energies and transition strengths in nuclei is the interacting boson model [31], developed by Iachello and Arima.

In the IBM, a nucleus is viewed as a system composed of a double-magic core nucleus and valence nucleons. The main assumptions of the IBM are that the valence nucleons are coupled into bosons, and that the main contribution to the low-lying excitation energy spectra and transitions comes from the pairing correlations between the bosons. The two main versions of the IBM are the IBM-1 and IBM-2, the main difference being that the IBM-1 treats neutron and proton bosons as being identical, while the IBM-2 does not [31]. Different versions of the IBM can also be constructed based on the types of bosons nucleons couple into. The most commonly employed version of the IBM, called *sd*-IBM, takes into account *s* bosons ( $J^\pi = 0^+$ ) and *d* bosons ( $J^\pi = 2^+$ ). The *sd*-IBM (both -1 and -2) has been successfully applied to a wide range of nuclei [32–34], and has been shown to be able to accurately describe the effects of quadrupole deformations in nuclei [35]. In order to incorporate hexadecapole correlations in IBM, it is necessary to introduce a new degree of freedom via the *g* boson ( $J^\pi = 4^+$ ). The need for including the *g* boson in the IBM, for the purpose of describing excitation energies and transitions in certain nuclei, has been recognized for decades [35, 36], and the calculations with the *sdg*-IBM have been successfully performed and were shown to provide an improvement over the simpler *sd*-IBM in describing the low-lying spectra in certain nuclei [37–40]. Since

hexadecapole correlations are the topic of interest in this work, the *sdg*-IBM-1 model is used in calculations. It should be noted that, while a more complex *sdg*-IBM-2 model could have been used, the calculations would have become significantly more time-consuming due to the large increase in dimension of the Hamiltonian matrix, and the IBM-1 and -2 are expected to yield similar results for most of the low-lying excited energy states, the most significant difference being the neutron-proton mixed symmetry states. The *sdg*-IBM-2 is therefore left for a different study.

While successful, the IBM was constructed as a phenomenological model, with parameters of the Hamiltonian being determined by fitting them to the experimental data on low-lying excitation spectra. This presents a problem if the goal is to describe the properties of a nucleus in a purely microscopic framework. Recently, a method has been developed that derives the parameters of the IBM Hamiltonian by fitting them to the PES calculated with the SCMF model [41]. This way, the IBM is derived from a microscopic model. The method has been successfully applied to study the effects of quadrupole axial and triaxial deformations [41–45], as well as axial octupole deformations [46, 47]. It should also be noted that the method was found to be successful in the framework of both non-relativistic [41] and relativistic EDFs [47]. While quadrupole and octupole collectivity in nuclei have been investigated with the aforementioned method, the hexadecapole collectivity has yet to be explored. Due to the fact that hexadecapole correlations have significant effects on the low-lying spectra in certain nuclei, and due to the fact that the *sdg*-IBM has been shown to be an important model, applying the aforementioned method to the *sdg*-IBM presents itself as a timely and interesting study, which could bring us closer to a better understanding of the microscopic origin of the hexadecapole collectivity in nuclei. For those reasons, the topic of this thesis is the construction of the mapped *sdg*-IBM model, derived from the RMF calculations, with the REDF of choice being the density dependent point coupling functional DD-PC1 [24, 48]. The constructed mapped *sdg*-IBM was applied to even-even rare-earth isotopes of Nd, Sm, Gd, Dy and Er ( $Z = 60 - 68$ ) with neutron number in range  $N = 84 - 96$ , so that both spherical vibrational, transitional and well deformed nuclei could be studied. The choice of studying even-even rare-earth nuclei was made due to the fact that hexadecapole correlations have been observed in them, as well as due to the fact that previous SCMF calculations showed that triaxiality does not have a significant presence in them [42, 49], making these nuclei the perfect candidates for SCMF calculations with constraints set on axial quadrupole and axial hexadecapole deformation parameters. The mapped *sdg*-IBM was used to calculate the low-lying excitation energy spectra, as well as quadrupole, hexadecapole and monopole transition strengths. The results were compared with the experimental data, mostly taken from the Brookhaven National Nuclear Data Center (NNDC) [50],

as well as with the results obtained with a simpler  $sd$ -IBM, in order to see the effects of the  $g$  boson on the excitation energies and transitions.

The thesis is organized in the following way. In Chapter 2, a detailed description of the theoretical framework is given. A theory is provided on how nuclear deformations are described. The RMF models with and the DD-PC1 REDF are also described in detail. A detailed description of both the  $sd$ - and  $sdg$ -IBM is given, with the latter being presented as an extension of the former. Finally, a mapping method for both models is given. In Chapter 3, the results of the mapped  $sdg$ -IBM are presented and discussed. The importance of the constructed model is explained by comparing the results to both the  $sd$ -IBM results and the experimental data. Lastly, in Chapter 4, a summary of the thesis and the outlook are given.



# Chapter 2

## Theoretical framework

### 2.1 Quadrupole and hexadecapole deformations

Nuclear deformations can be introduced in the framework of the liquid drop model through the parametrization of the nuclear radius [4]:

$$R(\theta, \phi) = R_0 \left( 1 + a_{00} + \sum_{\lambda=1}^{\infty} \sum_{\mu=-\lambda}^{\lambda} a_{\lambda\mu}^* Y_{\lambda\mu}(\theta, \phi) \right), \quad (2.1)$$

where  $R_0$  represents a radius of a sphere of the same volume. The term  $a_{00}$  is a constant, which can be determined by demanding that the volume of a nucleus should be constant:

$$V = \frac{4}{3} R_0^3 \pi. \quad (2.2)$$

The dipole terms  $a_{1\mu}$  can also be fixed by fixing the origin of the coordinate system to the centre of mass [4]:

$$\int \mathbf{r} d^3 r = 0. \quad (2.3)$$

If only axial deformations ( $\mu = 0$ ) are considered, the parameters of Eq. (2.1) can be redefined as  $a_{\lambda 0} \equiv \beta_\lambda$ , with parameters  $\beta_\lambda$  being called the deformation parameters. The most commonly considered deformations are quadrupole ( $\lambda = 2$ ), which can be prolate ( $\beta_2 > 0$ ) or oblate ( $\beta_2 < 0$ ), octupole ( $\lambda = 3$ ) and hexadecapole ( $\lambda = 4$ ), which can, just like quadrupole deformations, also be positive or negative. These shapes can be seen in Fig. 2.1.

Both quadrupole and hexadecapole deformations affect the low-lying positive parity states and transitions between those states, while the most pronounced effect of the octupole deformations is on the low-lying negative parity states [51]. This means that, for a complete and

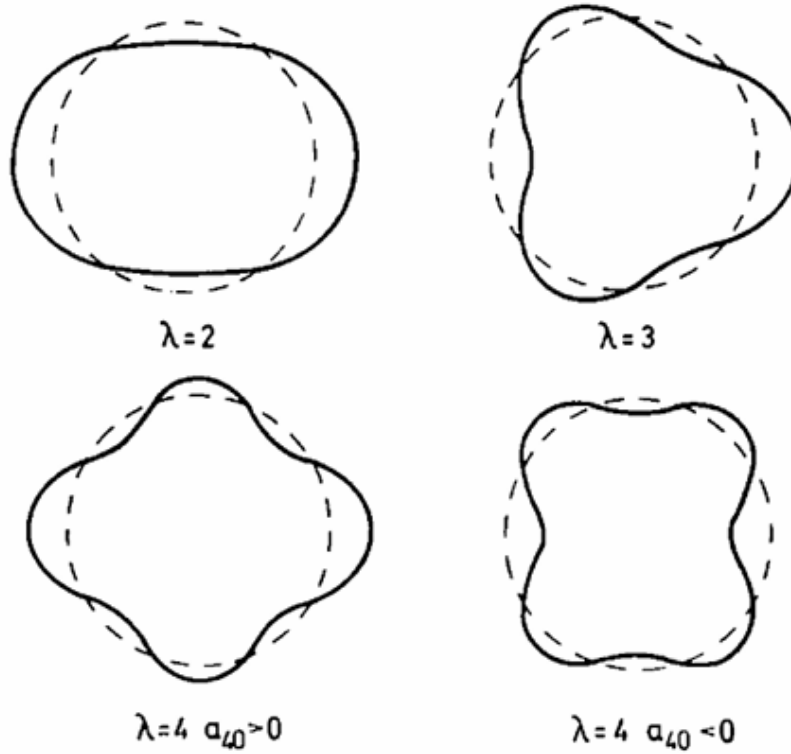


Figure 2.1: The most common axial nuclear deformations. From left to right, first row: quadrupole deformation, octupole deformation. Second row: positive hexadecapole deformation, negative hexadecapole deformation. Figure is taken from Ref. [4].

accurate description of the low-lying excitation energy spectra, all the mentioned deformations would have to be included, as well as the triaxial ( $\mu = 2$ ) ones, however, this would significantly complicate the model used in this thesis, and such calculations are beyond the scope of this study. As was previously mentioned in Chapter 1, hexadecapole correlations are expected to play a role in the description of low-lying yrast states in rare-earth nuclei with  $N$  being near  $N = 82$  shell closure (spherical vibrational nuclei), and are expected to play a role in the description of E2 and E4 transition systematics in well deformed isotopes.

## 2.2 Relativistic mean field models

The SCMF models can be understood as analogues of the Kohn-Sham density functional theory (DFT) [24]. The DFT was established by Hohenberg and Kohn, for the purpose of describing an inhomogeneous electron gas, with the Hohenberg-Kohn theorem stating that, for a given system, there exists a unique energy functional of the density, such that the variational equation yields the exact ground state density of a given system [52]. The Hohenberg-Kohn theorem was later

expanded by Kohn and Sham [53] to quantum many-body systems in general, by stating that for any interacting quantum many-body system, there exists a unique single-particle potential  $v_s(\mathbf{r})$ , such that the exact ground state density of the interacting system equals the ground state density of the auxiliary non-interacting system [24, 53]:

$$\rho(\mathbf{r}) = \rho_s(\mathbf{r}) = \sum_i^N |\phi_i(\mathbf{r})|^2, \quad (2.4)$$

with the number  $N$  representing the number of lowest occupied single-particle orbitals. These single-particle wave functions are the solutions of Kohn-Sham equations [24, 53]:

$$\left[ -\frac{1}{2m} \nabla^2 + v_s(\mathbf{r}) \right] \phi_i(\mathbf{r}) = \varepsilon_i \phi_i(\mathbf{r}), \quad (2.5)$$

and are unique functionals of the density  $\phi_i(\mathbf{r}) = \phi_i([\rho]; \mathbf{r})$ . In an atomic nucleus, the EDF can be expressed in the following way [24]:

$$F(\rho) = T_s(\rho) + E_H(\rho) + E_{xc}(\rho), \quad (2.6)$$

with  $T_s(\rho)$  corresponding to the kinetic energy of the non-interacting system of nucleons,  $E_H(\rho)$  representing the Hartree energy, and  $E_{xc}(\rho)$  being the exchange correlation energy, which contains all the remaining many-body effects.

A special class of the SCMF models are the RMF models. These models employ REDFs, which are built with nucleon densities and currents that are bilinear in the Dirac spinor field  $\psi$  of the nucleon [24]:

$$\bar{\psi} O_\tau \Gamma \psi, \quad O_\tau \in \{1, \tau_i\}, \quad \Gamma \in \{1, \gamma_\mu, \gamma_5, \gamma_5 \gamma_\mu, \sigma_{\mu\nu}\}, \quad (2.7)$$

with  $\tau_i$  representing the isospin Pauli matrices and  $\Gamma$  representing the Dirac matrices. In order to derive the relativistic Kohn-Sham equations, a Lagrangian needs to be constructed. The Lagrangian is usually constructed with four-fermion interaction terms in isoscalar-scalar  $(\bar{\psi}\psi)^2$ , isoscalar-vector  $(\bar{\psi}\gamma_\mu\psi)(\bar{\psi}\gamma^\mu\psi)$  and isovector-vector  $(\bar{\psi}\vec{\tau}\gamma_\mu\psi)(\bar{\psi}\vec{\tau}\gamma^\mu\psi)$  channels [24]. A typical RMF Lagrangian can be written in the following way [24, 54]:

$$\begin{aligned} \mathcal{L} = & \bar{\psi}(i\gamma \cdot \partial - m)\psi \\ & - \frac{1}{2} \alpha_S(\hat{\rho})(\bar{\psi}\psi)(\bar{\psi}\psi) - \frac{1}{2} \alpha_V(\hat{\rho})(\bar{\psi}\gamma^\mu\psi)(\bar{\psi}\gamma_\mu\psi) - \frac{1}{2} \alpha_{TV}(\hat{\rho})(\bar{\psi}\vec{\tau}\gamma^\mu\psi)(\bar{\psi}\vec{\tau}\gamma_\mu\psi) \\ & - \frac{1}{2} \delta_S(\partial_\nu \bar{\psi}\psi)(\partial^\nu \bar{\psi}\psi) - e \bar{\psi}\gamma \cdot A \frac{(1 - \tau_3)}{2} \psi. \end{aligned} \quad (2.8)$$

The first term is a free nucleon term, with  $m$  being the nucleon mass, while the next three terms represent the isoscalar-scalar, isoscalar-vector and isovector-vector point-coupling terms, respectively. The final two terms are the derivative coupling term, which accounts for the finite range effects [24, 54], and the coupling of the proton to the electromagnetic field. In principle, it is possible to expand the Lagrangian by including the isovector-scalar term, as well as non-linear coupling terms [55], however, the Lagrangian from Eq. (2.8) has been shown to be adequate in describing the ground state properties of a nucleus. By varying the Lagrangian with respect to  $\bar{\Psi}$ , a relativistic single-nucleon Dirac equation is obtained [24]:

$$[\gamma_\mu(i\partial^\mu - \Sigma^\mu - \Sigma_R^\mu) - (m + \Sigma_S)] \Psi = 0, \quad (2.9)$$

with nucleon self-energies being defined as:

$$\Sigma^\mu = \alpha_V(\rho_v)j^\mu + e\frac{1-\tau_3}{2}A^\mu, \quad (2.10)$$

$$\Sigma_R^\mu = \frac{1}{2}\frac{j^\mu}{\rho_v} \left\{ \frac{\partial\alpha_S}{\partial\rho}\rho_s^2 + \frac{\partial\alpha_V}{\partial\rho}j_\mu j^\mu + \frac{\partial\alpha_{TV}}{\partial\rho}\vec{j}_\mu \vec{j}^\mu \right\}, \quad (2.11)$$

$$\Sigma_S = \alpha_S(\rho_v)\rho_s - \delta_S\Box\rho_s \quad (2.12)$$

$$\Sigma_{TV}^\mu = \alpha_{TV}(\rho_v)\vec{j}^\mu. \quad (2.13)$$

In the ground state of a nucleus  $|\phi_0\rangle$ , the isoscalar 4-current, the isovector 4-current and the scalar density are respectively defined as:

$$j_\mu = \langle\phi_0|\bar{\Psi}\gamma_\mu\Psi|\phi_0\rangle = \sum_{k=1}^N v_k^2 \bar{\Psi}_k \gamma_\mu \Psi_k, \quad (2.14)$$

$$\vec{j}_\mu = \langle\phi_0|\bar{\Psi}\gamma_\mu\vec{\tau}\Psi|\phi_0\rangle = \sum_{k=1}^N v_k^2 \bar{\Psi}_k \gamma_\mu \vec{\tau} \Psi_k, \quad (2.15)$$

$$\rho_s = \langle\phi_0|\bar{\Psi}\Psi|\phi_0\rangle = \sum_{k=1}^N v_k^2 \bar{\Psi}_k \Psi_k, \quad (2.16)$$

with  $v_k^2$  corresponding to occupation factors.

The three parameters  $\alpha_S$ ,  $\alpha_V$  and  $\alpha_{TV}$  in the DD-PC1 functional, are constructed with 9 parameters [24]:

$$\alpha_S(\rho) = a_S + (b_S + x c_S)e^{-d_S x}, \quad (2.17)$$

$$\alpha_V(\rho) = a_V + b_V e^{-d_V x}, \quad (2.18)$$

$$\alpha_{TV}(\rho) = b_{TV} e^{-d_{TV} x}, \quad (2.19)$$

where  $x = \rho/\rho_{sat}$ . The parameter  $\rho_{sat}$  represents the saturation density of symmetric nuclear matter. These 9 parameters are determined by fitting them to the experimental data on masses of 64 axially deformed nuclei in the regions  $A \approx 150 - 180$  and  $A \approx 230 - 250$  [56].

In order to account for pairing effects in open shell nuclei, the RMF model is extended to include the RHB model of pairing. In the RHB model, the ground state of a nucleus is approximated by a quasiparticle vacuum  $|\Phi\rangle$  [26], and the quasiparticle operators are constructed with creation and annihilation operators:

$$\alpha_k^\dagger = \sum_l U_{lk} c_l^\dagger + V_{lk} c_l, \quad (2.20)$$

with  $U$  and  $V$  corresponding to Hartree-Bogoliubov wave functions. Using the Green function technique, a relativistic Dirac-Hartree-Bogoliubov equation can be derived [54]:

$$\int d^3 \mathbf{r}' \begin{pmatrix} h - \lambda & \Delta \\ -\Delta^* & -h + \lambda \end{pmatrix} \begin{pmatrix} U_k \\ V_k \end{pmatrix} = E_k \begin{pmatrix} U_k \\ V_k \end{pmatrix}, \quad (2.21)$$

where  $E_k$  is the quasiparticle energy,  $\lambda$  is the chemical potential, determined from the condition that the expectation value of the particle number operator in the ground state equals the nucleon number, and  $h$  is the single-particle Hamiltonian from Eq. (2.9). The pairing field  $\Delta$  is, in the case of a general two-body interaction, defined as [54]:

$$\Delta_{p_1 p_2}(\mathbf{r}_1 \sigma_1, \mathbf{r}_2 \sigma_2) = \int d^3 \mathbf{r}'_1 d^3 \mathbf{r}'_2 \sum_{\sigma'_1, \sigma'_2}^{p'_1, p'_2} V_{p_1, p_2, p'_1, p'_2}^{pp}(\mathbf{r}_1 \sigma_1, \mathbf{r}_2 \sigma_2, \mathbf{r}'_1 \sigma'_1, \mathbf{r}'_2 \sigma'_2) \times \kappa_{p'_1, p'_2}(\mathbf{r}'_1 \sigma'_1, \mathbf{r}'_2 \sigma'_2), \quad (2.22)$$

with  $V^{pp}$  being the effective pairing interaction, and

$$\kappa_{\alpha' \alpha}(\mathbf{r}_1 \sigma_1, \mathbf{r}_2 \sigma_2) = \sum_{k > 0} V_{\alpha k}^*(\mathbf{r}_1 \sigma_1) U_{\alpha' k}(\mathbf{r}_2 \sigma_2) \quad (2.23)$$

being the pairing tensor. The  $p = f, g$  represent the large and small components of quasiparticle Dirac spinors [24]:

$$U(\mathbf{r}, s, t) = \begin{pmatrix} f_U(\mathbf{r}, s, t) \\ ig_U(\mathbf{r}, s, t) \end{pmatrix}, \quad V(\mathbf{r}, s, t) = \begin{pmatrix} f_V(\mathbf{r}, s, t) \\ ig_V(\mathbf{r}, s, t) \end{pmatrix}. \quad (2.24)$$

Usually, only  $ff$  components are considered [54].

In the pp channel, the pairing interaction reads [24, 54]:

$$V(\mathbf{r}_1\sigma_1, \mathbf{r}_2\sigma_2, \mathbf{r}'_1\sigma'_1, \mathbf{r}'_2\sigma'_2) = -G\delta(\mathbf{R} - \mathbf{R}')P(r)P(r')\frac{1}{2}(1 - P_\sigma), \quad (2.25)$$

where  $G$  is the pairing strength,  $\mathbf{R} = (\mathbf{r}_1 + \mathbf{r}_2)/2$  and  $\mathbf{r} = \mathbf{r}_1 - \mathbf{r}_2$  are the centre of mass and relative coordinates, respectively, and

$$P(\mathbf{r}) = (4\pi a^2)^{-3/2} e^{-r^2/4a^2} \quad (2.26)$$

is the Gaussian function, with  $a$  being the effective range of the pairing force. Both  $G$  and  $a$  are fixed in order to reproduce the neutron pairing gaps and pairing energies calculated with the Gogny D1S force. The RHB equation (2.21) is solved by expanding the components of Dirac spinors in the basis of the axially deformed harmonic oscillator (ADHO) [54]:

$$U_k(\mathbf{r}\sigma) = \begin{pmatrix} \sum_\alpha f_U^{k\alpha} \Phi_\alpha(\mathbf{r}\sigma) \\ \sum_\alpha g_U^{k\alpha} \Phi_\alpha(\mathbf{r}\sigma) \end{pmatrix}, \quad V_k(\mathbf{r}\sigma) = \begin{pmatrix} \sum_\alpha f_V^{k\alpha} \Phi_\alpha(\mathbf{r}\sigma) \\ \sum_\alpha g_V^{k\alpha} \Phi_\alpha(\mathbf{r}\sigma) \end{pmatrix}, \quad (2.27)$$

with

$$\Phi_\alpha(\mathbf{r}\sigma) = C_\alpha \phi_{n_z}(z) \phi_{n_r}^{m_l}(\rho) \frac{1}{\sqrt{2\pi}} e^{im_l\phi} \chi_{m_s}(\rho), \quad (2.28)$$

being the eigensolutions of the Schrödinger equation in the ADHO potential

$$V_B(\rho, z) = \frac{1}{2} M(\omega_\rho^2 \rho^2 + \omega_z^2 z^2). \quad (2.29)$$

Here,  $\alpha = \{n_z, n_r, m_l, m_s\}$  are the quantum numbers and  $\omega_z$  and  $\omega_\rho$  are oscillator frequencies along and perpendicular to the  $z$ -axis [54]. The pairing energy is calculated by the following expression [54]:

$$E_{\text{pair}} = \frac{1}{2} \sum_{12, 1'2'} V_{12, 1'2'} \kappa_{12}^* \kappa_{1'2'}. \quad (2.30)$$

Along with the pairing energy, another form of energy added to Eq. (2.9) is the centre of mass correction in the quasiparticle vacuum [54]:

$$E_{\text{c.m.}} = -\frac{\langle P^2 \rangle}{2MA}, \quad (2.31)$$

where  $P$  is the total linear momentum and  $A$  is the nucleon number. The expression for the  $E_{\text{c.m.}}$

can also be given phenomenologically as [54]:

$$E_{c.m} \approx -\frac{3}{4} \times 41A^{1/3} \text{ MeV}. \quad (2.32)$$

In order to calculate the PES as a function of desired deformation parameters, a quadratic constraint method is applied. In this method, the energy of the nucleus is calculated in the following way [55]:

$$E' = E_{RMF} + \sum_{\lambda\mu} C_{\lambda\mu} (\langle \hat{Q}_{\lambda\mu} \rangle - m_{\lambda\mu})^2, \quad (2.33)$$

with  $E_{RMF}$  representing the calculated energy in the RMF model, with pairing and centre of mass correction energy added,  $\langle \hat{Q}_{\lambda\mu} \rangle$  representing the expectation value of the multipole moment operator and  $m_{\lambda\mu}$  representing the desired value of the multipole moment operator. If the parametrization

$$\beta_{\lambda\mu} = \frac{4\pi}{3AR^\lambda} \langle \hat{Q}_{\lambda\mu} \rangle \quad (2.34)$$

is used, with  $R = 1.2 \times A^{1/3}$  fm being the nuclear radius, the constrained calculation can be written in a modified form as [55]:

$$E' = E_{RMF} + \frac{1}{2} \sum_{\lambda\mu} C_{\lambda\mu} Q_{\lambda\mu}, \quad (2.35)$$

where the values of  $C_{\lambda\mu}$  change during the iteration in the following way:

$$C_{\lambda\mu}^{(n+1)} = C_{\lambda\mu}^{(n)} + k_{\lambda\mu} (\beta_{\lambda\mu}^{(n)} - \beta_{\lambda\mu}). \quad (2.36)$$

Here,  $k_{\lambda\mu}$  is the spring constant, whose value needs to be set in order to ensure that the convergence will happen, and the  $\beta_{\lambda\mu}$  represents the desired value of the deformation parameter. Recently, multidimensionally constrained (MDC-RMF) models have been developed [54, 55, 57, 58], that allow for the quadratic constraint calculations to be performed for a wide range of desired deformation parameters, including the axial quadrupole  $\beta_{20}$  and hexadecapole  $\beta_{40}$  parameters, which were used in this work.

## 2.3 The interacting boson model, *sd* and *sdg*

The IBM was developed by Iachello and Arima [31], in order to describe various properties of the nucleus, e.g. excitation energies and transition strengths. Since its development, it has been one of the most successful and widely used models in nuclear structure. As was men-

tioned in Chapter 1, the main assumption of the model is that the nucleus is composed of an inert doubly-magic core and valence nucleons, which could be represented by both particles and holes, depending on the closest magic number. For example, in even-even isotopes of  $^{144-156}\text{Nd}$ ,  $^{146-158}\text{Sm}$ ,  $^{148-160}\text{Gd}$  and  $^{150-162}\text{Dy}$  ( $Z = 60 - 66$ ,  $N = 84 - 96$ ), the core nucleus corresponds to the doubly magic nucleus  $^{132}\text{Sn}$  ( $Z = 50, N = 82$ ), while for even-even  $^{152-164}\text{Er}$  ( $Z = 68, N = 84 - 96$ ) isotopes, the core nucleus corresponds to the ( $Z = 82, N = 82$ ) nucleus, and the valence nucleons are treated as being hole-like. The coupling of valence nucleus into bosons and the interaction between the bosons is what generates the low-lying excitation spectra and its properties. In the IBM-1 version of the model, which is the one used in this work, the proton and neutron bosons are treated as identical particles. The choice of bosons the nucleons couple to represents the building blocks of the IBM [31].

### 2.3.1 *sd*-IBM

In the simplest version of the model, *sd*-IBM, valence nucleons are grouped into  $s$  ( $J^\pi = 0^+$ ) and  $d$  ( $J^\pi = 2^+$ ) bosons. This makes for a total of 6 bosonic operators [31]:

$$s, d_\mu; \mu = \{-2, -1, 0, 1, 2\}. \quad (2.37)$$

These bosonic operators satisfy the commutation relations:

$$[b_{lm}, b_{l'm'}^\dagger] = \delta_{ll'} \delta_{mm'}, \quad l = 0, 2, \quad m \in [-l, l]. \quad (2.38)$$

It is useful to look at the conditions, under which the solutions to the eigenenergies of the Hamiltonian are analytical, the so-called dynamical symmetries. The *sd*-IBM Hamiltonian is defined by up to 36 bilinear tensor products of bosonic operators:

$$G_{\mathbf{k}}^{(k)}(l, l') = [b_l^\dagger \times \tilde{b}_{l'}]_{\mathbf{k}}^{(k)}, \quad (2.39)$$

with  $\tilde{b}_{lm} = (-1)^{l+m} b_{l,-m}$ . The tensor product is defined as [59]:

$$[\hat{T}^{(k_1)} \times \hat{T}^{(k_2)}]_{\mathbf{k}}^{(k)} = \sum_{\mathbf{k}_1, \mathbf{k}_2} (k_1 k_2 \mathbf{k}_1 \mathbf{k}_2 | k \mathbf{k}) \hat{T}_{\mathbf{k}_1}^{(k_1)} \hat{T}_{\mathbf{k}_2}^{(k_2)}, \quad (2.40)$$

with  $(k_1 k_2 \mathbf{k}_1 \mathbf{k}_2 | k \mathbf{k})$  being the Clebsch-Gordan coefficients. The scalar product corresponds to the tensor product with  $k = 0$ . The 36 operators  $G_{\mathbf{k}}^{(k)}(l, l')$  represent the 36 generators of the U(6) group. When the operators of the Hamiltonian are generators of a group  $G$ , and its subgroups



$G', G'', \dots$ , the Hamiltonian can be expressed through Casimir operators  $\hat{C}_G, \hat{C}_{G'}, \hat{C}_{G''}, \dots$ , which are the operators that commute with all the generators of a particular group or subgroup  $G$  [60]:

$$\hat{H} = a\hat{C}_G + b\hat{C}_{G'} + c\hat{C}_{G''} + \dots, \quad (2.41)$$

with

$$G \supset G' \supset G'' \supset \dots \quad (2.42)$$

representing a chain of group  $G$  and its subgroups. These chains are called dynamical symmetries, and each chain is characterized by specific quantum numbers. Since the rotational invariance of the nucleus implies the  $O(3)$  symmetry, the three possible symmetry limits of the *sd*-IBM are the  $U(5)$ ,  $SU(3)$  and  $O(6)$  symmetries [31, 45].

In the  $U(5)$  chain:

$$U(6) \supset U(5) \supset O(5) \supset O(3) \supset O(2), \quad (2.43)$$

the quantum numbers are the  $d$  boson number  $n_d$ , the  $d$  boson seniority  $\nu$ , the number of triple bosons  $n_\Delta$  coupled to  $J^\pi = 0^+$ , the total angular momentum  $L$  and the  $z$ -component of the angular momentum  $M$ , in the laboratory frame [45]. The Casimir operator of the  $U(5)$  group is the  $d$  boson number operator  $\hat{n}_d = \sqrt{5} [d^\dagger \times \tilde{d}]^{(0)}$ . The energy eigenvalues are expressed as [31]:

$$E(n_d, \nu, n_\Delta, L, M) = \varepsilon n_d + \alpha \frac{1}{2} n_d (n_d - 1) + \beta (n_d - \nu) (n_d + \nu + 3) + \gamma [L(L + 1) - 6n_d]. \quad (2.44)$$

These eigenvalues give rise to a level structure which resembles a phonon [31, 45]. The parameters  $\varepsilon, \alpha, \beta$  and  $\gamma$  are fitted to the experimentally observed low-lying spectra.

In the  $SU(3)$  chain:

$$U(6) \supset SU(3) \supset O(3) \supset O(2), \quad (2.45)$$

the quantum numbers are  $L$  and  $M$ , as well as  $\lambda, \mu$  and  $K$ , which represents the  $z$ -component of the angular momentum in the intrinsic frame [31]. The energy eigenvalues are:

$$E(\lambda, \mu, L, M) = \alpha L(L + 1) - \beta [\lambda^2 + \mu^2 + \lambda\mu + 3(\lambda + \mu)]. \quad (2.46)$$

Once again,  $\alpha$  and  $\beta$  are fitted to the measured energy levels. The  $SU(3)$  chain eigenvalues give rise to rotational bands of axially deformed nuclei [31, 45].

Finally, the  $O(6)$  chain:

$$U(6) \supset O(6) \supset O(5) \supset O(3) \supset O(2), \quad (2.47)$$

is defined by the quantum numbers  $\sigma$ , which characterizes the irreducible representation of the  $O(6)$  group, the  $d$  boson seniority  $\tau$  of the  $O(5)$  group,  $\nu_\Delta$ , which is the same as  $n_\Delta$  in the  $U(5)$  chain,  $L$  and  $M$  [31]. The energy eigenvalues:

$$E(\sigma, \tau, \nu_\Delta, L, M) = A \frac{1}{4} (N - \sigma)(N + \sigma + 4) + B \frac{1}{6} \tau(\tau + 1) + CL(L + 1), \quad (2.48)$$

give rise to the spectra which corresponds to  $\gamma$  unstable nuclei [31, 45]. The parameters  $A, B, C$  are fitted in order to reproduce the measured energies.

A simple form of the  $sd$ -IBM Hamiltonian, the one used in this work, can be written in the following way:

$$\hat{H}_{sd} = \varepsilon_d \hat{n}_d + \kappa \hat{Q}^{(2)} \cdot \hat{Q}^{(2)}, \quad (2.49)$$

with  $\hat{n}_d$  representing the  $d$  boson number operator, which was discussed earlier and

$$\hat{Q}^{(2)} = \left[ d^\dagger \times s + s^\dagger \times \tilde{d} \right]^{(2)} + \chi \left[ d^\dagger \times \tilde{d} \right]^{(2)}, \quad (2.50)$$

representing the quadrupole interaction operator. While it is possible to expand the aforementioned Hamiltonian by adding more interactions, this Hamiltonian has been shown to be useful in describing the properties of the low-lying excitation spectra in many nuclei. The Hamiltonian is also constructed so that the previously discussed symmetry limits are achievable. For instance, if  $\kappa = 0$ , the  $U(5)$  symmetry limit is achieved. The  $SU(3)$  symmetry limit occurs for  $\chi = \pm\sqrt{7}/2$ , while the  $O(6)$  symmetry limit is achieved for  $\chi = 0$ . The three independent parameters,  $\varepsilon_d, \kappa, \chi$  are usually fitted to the experimental data on low-lying energies. The conditions  $\kappa < 0$  and  $-\sqrt{7}/2 \leq \chi \leq +\sqrt{7}/2$  are set in order to ensure that the calculated spectra are physically possible. Since the symmetry limit conditions are rarely met, the problem of finding the eigenvalues of the Hamiltonian has to be solved numerically.

### 2.3.2 $sdg$ -IBM

One possible extension of the  $sd$ -IBM is the inclusion of the  $g$  boson, defined by the total angular momentum  $J^\pi = 4^+$ . Along with the 6 bosonic operator of the  $sd$ -IBM, defined in Eq. (2.37), the 9 bosonic operators:

$$g_{\mu}; \mu = \{-4, -3, -2, -1, 0, 1, 2, 3, 4\}, \quad (2.51)$$

make up a total of 15 bosonic operators. This leads to a total of 225 tensor products  $G_{\kappa}^{(k)}(l, l')$  of Eq. (2.39), which represent the generators of the  $U(15)$  group [31]. The dynamical symmetry

chains typically considered in the  $sdg$ -IBM are the  $[U(6) \supset U(5)] \otimes U(9)$ ,  $SU(3)$  and  $O(15)$  limits [61–63].

In the  $[U(6) \supset U(5)] \otimes U(9)$  symmetry limit, the  $s, d$  and  $g$  bosons are decoupled. The  $[U(6) \supset U(5)]$  limit represents the  $U(5)$  limit of the  $sd$ -IBM from Eq. (2.43), defined by the same quantum numbers  $n_d, \nu, n_\Delta, L, M$ . The chain:

$$U(9) \supset O(9) \supset O(3), \quad (2.52)$$

is defined by the quantum numbers  $n_g$ , being the  $g$  boson number, the  $g$  boson seniority  $\nu_g$  and  $g$  boson angular momentum  $L_g$  [61]. The energy eigenvalues can be expressed as:

$$\begin{aligned} E(n_d, \nu_d, L_d, n_g, \nu_g, L_g, L) = & \varepsilon_d n_d + \alpha_d n_d(n_d + 5) + \beta_d \nu_d(\nu_d + 3) + \gamma_d L_d(L_d + 1) \\ & + \varepsilon_g n_g + \alpha_g n_g(n_g + 9) + \beta_g \nu_g(\nu_g + 7) \\ & + \gamma_g L_g(L_g + 1) + \gamma L(L + 1). \end{aligned} \quad (2.53)$$

One can notice that the number of independent parameters to fit has increased from 4  $sd$ -parameters in Eq. (2.44) to 9 parameters in total. The spectrum of the nucleus generated by the aforementioned symmetry limit corresponds to that of a double phonon [62].

The  $SU(3)$  chain is the shortest possible chain:

$$U(15) \supset SU(3) \supset O(3), \quad (2.54)$$

with the quantum numbers being the  $SU(3)$  representation numbers  $(\lambda, \mu)$ , angular momentum  $L$  and the  $SU(3)$ -seniority quantum number  $W = \frac{1}{2}(N - \nu)$ , first introduced by Akiyama [64]. The energy eigenvalues are:

$$E(\lambda, \mu, W, L) = \alpha(\lambda^2 + \mu^2 + \lambda\mu + 3(\lambda + \mu)) + \frac{\beta}{\sqrt{375}} W(2N - W + 3) + \gamma L(L + 1), \quad (2.55)$$

with  $\alpha, \beta$  and  $\gamma$  being the parameters which need to be determined from the fit [62, 64]. This symmetry limit, just like in the  $sd$ -IBM case, gives rise to rotational bands of axially deformed nuclei [62].

Finally, the  $O(15)$  chain:

$$U(15) \supset O(15) \supset O(14) \supset O(5) \supset O(3), \quad (2.56)$$

is described with the quantum numbers  $\sigma_{sdg}$ , characterizing the irreducible representation of the

O(15) group, the seniority number  $\nu_{dg}$  of the O(14) group, seniority numbers  $\tau_1, \tau_2$  of the O(5) group, and the angular momentum number  $L$  [61, 62]. The energy eigenvalues can be written in the following form:

$$E(\sigma_{sdg}, \nu_{dg}, \tau_1, \tau_2, L) = A \frac{1}{4} (N - \sigma_{sdg})(N + \sigma_{sdg} + 13) + B \nu_{dg} (\nu_{dg} + 12) + C[\tau_1(\tau_1 + 1) + \tau_2(\tau_2 + 1)] + DL(L + 1). \quad (2.57)$$

This represents the extension of Eq. (2.48), and the parameters  $A, B, C, D$  have to be determined from the fit to the experimental data. The O(15) symmetry gives rise to spectra of  $\gamma$  unstable nuclei, just like the O(6) symmetry limit in the  $sd$ -IBM [62].

A typical  $sdg$ -IBM Hamiltonian can be written in the following way, similar to [40]:

$$\hat{H} = \varepsilon_d \hat{n}_d + \varepsilon_g \hat{n}_g + \kappa_2 \hat{Q}^{(2)} \cdot \hat{Q}^{(2)} + \kappa_4 \hat{Q}^{(4)} \cdot \hat{Q}^{(4)}, \quad (2.58)$$

with  $\hat{n}_d$  being the  $d$  boson number operator from Eq. (2.49),  $\hat{n}_g = \sqrt{9} [d^\dagger \times \tilde{d}]^{(0)}$  being the  $g$  boson number operator, while

$$\hat{Q}^{(2)} = [d^\dagger \times s + s^\dagger \times \tilde{d}]^{(2)} + \chi_{dd}^{(2)} [d^\dagger \times \tilde{d}]^{(2)} + \chi_{dg}^{(2)} [d^\dagger \times \tilde{g} + g^\dagger \times \tilde{d}]^{(2)} + \chi_{gg}^{(2)} [g^\dagger \times \tilde{g}]^{(2)}, \quad (2.59)$$

and

$$\hat{Q}^{(4)} = [g^\dagger \times s + s^\dagger \times \tilde{g}]^{(4)} + \chi_{dd}^{(4)} [d^\dagger \times \tilde{d}]^{(4)} + \chi_{dg}^{(4)} [d^\dagger \times \tilde{g} + g^\dagger \times \tilde{d}]^{(4)} + \chi_{gg}^{(4)} [g^\dagger \times \tilde{g}]^{(4)}, \quad (2.60)$$

represent the quadrupole and hexadecapole interaction operators, respectively. As can be seen from Eqs. (2.58, 2.59, 2.60), this Hamiltonian contains 10 independent parameters that need to be determined. This significantly complicates the IBM calculations. In order to avoid this problem, one can make use of the  $[U(6 \supset U(5))] \otimes U(9)$ ,  $SU(3)$  and O(15) symmetry limits to construct the Hamiltonian in the following way, similar to the Hamiltonian from Ref. [65]:

$$\hat{H}_{sdg} = \varepsilon_d \hat{n}_d + \varepsilon_g \hat{n}_g + \kappa \hat{Q}^{(2)} \cdot \hat{Q}^{(2)} + \kappa(1 - \chi^2) \hat{Q}^{(4)} \cdot \hat{Q}^{(4)}, \quad (2.61)$$

with

$$\hat{Q}^{(2)} = [d^\dagger \times s + s^\dagger \times \tilde{d}]^{(2)} + \chi \left( \frac{11\sqrt{10}}{28} [d^\dagger \times \tilde{d}]^{(2)} - \frac{9}{7} \sigma [d^\dagger \times \tilde{g} + g^\dagger \times \tilde{d}]^{(2)} + \frac{3\sqrt{55}}{14} [g^\dagger \times \tilde{g}]^{(2)} \right) \quad (2.62)$$

and

$$\hat{Q}^{(4)} = \left[ g^\dagger \times s + s^\dagger \times \tilde{g} \right]^{(4)} \quad (2.63)$$

representing the quadrupole and hexadecapole interaction operators, respectively. If the condition  $\sigma = 1$  is met, the Hamiltonian and its operators become equivalent to the Hamiltonian from Ref. [65]. The  $[U(6 \supset U(5)) \otimes U(9)]$  symmetry limit is realised for  $\kappa = 0$ , while the  $SU(3)$  and  $O(15)$  limits are realised for  $(\chi, \sigma) = (\pm 1, \pm 1)$  and  $\chi = 0$ , respectively [65]. The factors that appear in the quadrupole operator in Eq. (2.62) are set in order to ensure that for  $(\chi, \sigma) = (\pm 1, \pm 1)$  condition, the  $\hat{Q}^{(2)}$  becomes an  $SU(3)$  generator, and the factor  $(1 - \chi^2)$  in front of the hexadecapole interactions ensures that the  $SU(3)$  and  $O(15)$  symmetry limits will be achieved for  $\chi = \pm 1$  and  $\chi = 0$ , respectively [61, 62, 65]. Other conditions that need to be imposed on the system to ensure that the solution will be physical are  $\epsilon_d \leq \epsilon_g$ ,  $\kappa < 0$ ,  $-1 \leq \chi \leq +1$  [65] and  $-1 \leq \chi\sigma \leq +1$ . All of this reduces the number of Hamiltonian parameters from 10 to 5, which significantly simplifies the calculations in the  $sdg$ -IBM framework. Due to the increase in the number of bosonic parameters in the  $sdg$ -IBM, compared to the simpler  $sd$ -IBM, the Hamiltonian matrices that need to be diagonalized, become larger, making the calculations significantly more difficult and time-consuming. In order to avoid this problem, the maximum number of  $g$  bosons in the configuration can be reduced to  $N_{G_{\max}}=3$ . This can be done, since the hexadecapole collectivity in nuclei is often overshadowed by the dominant quadrupole effects in the low-lying excitation spectra, so the configurations containing 4 or more  $g$  bosons are not expected to have any significant contributions in the generated spectra.

### 2.3.3 Electric transitions in the IBM

Electric transition strengths  $B(E\lambda; J \rightarrow J')$  are defined as [47]:

$$B(E\lambda; J \rightarrow J') = \frac{1}{2J+1} \left| \langle J' | \hat{T}^{(E\lambda)} | J \rangle \right|^2, \quad (2.64)$$

where  $\hat{T}^{(E\lambda)}$  represents the  $E\lambda$  transition operator of rank  $\lambda$  and  $|J\rangle$  and  $\langle J'|$  represent the wave functions of the initial and final states in the transition, respectively. The electric transitions, which are relevant for this work, are the quadrupole ( $\lambda = 2$ ), hexadecapole ( $\lambda = 4$ ) and monopole ( $\lambda = 0$ ) transitions.

The quadrupole electric transition operator is defined both in the  $sd$ - and  $sdg$ -IBM as:

$$\hat{T}^{(E2)} = e_2^{sd, sdg} \hat{Q}^{(2)}, \quad (2.65)$$

where  $e_2^{sd, sdg}$  represent the quadrupole effective charges of the  $sd$ - and  $sdg$ -IBM, respectively, and  $\hat{Q}^{(2)}$  corresponds to the quadrupole operator of Eq. (2.50) in the  $sd$ -IBM, as well as to the quadrupole operator of Eq. (2.62) in the  $sdg$ -IBM. The quadrupole effective charges are fitted in order to reproduce the strength of the first  $B(E2; 2^+ \rightarrow 0^+)$  transition in the ground state band.

The hexadecapole transition operator is defined in the  $sd$ -IBM in the following way:

$$\hat{T}^{(E4)} = e_4^{sd} \left[ d^\dagger \times \tilde{d} \right]^{(4)}. \quad (2.66)$$

In the  $sdg$ -IBM, the hexadecapole transition operator can be defined as:

$$\hat{T}^{(E4)} = e_4^{sdg} \left( \left[ g^\dagger \times s + s^\dagger \times \tilde{g} \right]^{(4)} + \left[ d^\dagger \times \tilde{d} \right]^{(4)} \right). \quad (2.67)$$

Given the definition of the  $\hat{Q}^{(4)}$  operator in the Eq. (2.60), it is possible to expand the  $sdg$ -IBM hexadecapole transition operator with more terms, however, the two terms in the Eq. (2.67) are expected to be dominant in the calculations of  $E4$  transitions. Furthermore, by constructing the operator this way, it is possible to directly examine the impact of  $g$  bosons on  $E4$  transitions by comparing the obtained results to the ones obtained with a simpler  $sd$ -IBM hexadecapole transition operator. The  $e_4$  effective charges are fitted in order to reproduce the strength of the first  $B(E4; 4^+ \rightarrow 0^+)$  transition in the ground state band.

In the case of monopole transitions, the  $sd$ -IBM operator is defined as [66]:

$$\hat{T}^{(E0)} = (e_n N + e_p Z) \eta \frac{\hat{n}_d}{N_B}, \quad (2.68)$$

while the equivalent  $sdg$ -IBM operator is defined as:

$$\hat{T}^{(E0)} = (e_n N + e_p Z) \left( \eta \frac{\hat{n}_d}{N_B} + \gamma \frac{\hat{n}_g}{N_B} \right). \quad (2.69)$$

Here,  $e_n$  and  $e_p$  represent the effective neutron and proton charges, respectively. It should be noted that if bare nucleon charges are considered, then  $e_n = 0$  and  $e_p = e$ , however, by assigning an effective charge to neutrons, the polarization of protons in the nucleus due to neutrons is taken into consideration [66]. The parameter  $N_B$  corresponds to the number of valence bosons in a particular nucleus. Instead of calculating  $B(E0)$  monopole transition strengths, the so-called squared monopole strengths  $\rho^2(E0)$  are usually considered. They are defined as [66]:

$$\rho(E0) = \frac{\langle J' | \hat{T}^{(E0)} | J \rangle}{eR^2}, \quad (2.70)$$

with  $R = 1.2A^{1/3}$  fm being the nuclear radius. The parameters  $e_n, e_p, \eta$  and  $\gamma$  can, in principle, be fitted to the measured monopole strengths for each nucleus, however, following Ref. [66], they were fixed for all nuclei. More on that in Chapter 3.

## 2.4 Nucleon-to-boson mapping

Given the fact that the IBM is a collective model, and the collective modes of motion are described with deformations of the nuclear surface, it is natural to connect the IBM to the geometric models of the nucleus, where the energy is expressed as a function of nuclear deformation parameters, defined in Eq. (2.1) [67, 68]. In fact, it has been shown that any quantum system described by a Hamiltonian that can be expressed via generators of a compact Lie algebra, can be interpreted in the framework of a geometric model [69]. In the case of the IBM, this can be done by constructing the boson coherent state wave function, which is the intrinsic wave function of the boson system [70], and calculating the expectation value of the IBM Hamiltonian in that state. In order to describe this process, it is useful to start from the simple  $sd$ -IBM and then extend it to include the  $g$  boson.

### 2.4.1 Geometric interpretation of the $sd$ -IBM

In the  $sd$ -IBM, the coherent state can be written as [67]:

$$|\Phi(N_B, \{a_\mu\})\rangle = \frac{1}{\sqrt{N_B! (1 + \sum_\mu a_\mu^2)^{N_B}}} \left( s^\dagger + \sum_\mu a_\mu d_\mu^\dagger \right)^{N_B} |0\rangle, \quad (2.71)$$

where  $N_B$  is the number of valence bosons, and  $|0\rangle$  corresponds to the boson vacuum. The set of parameters  $\{a_\mu\}$  is defined with axial and triaxial quadrupole deformations as [45]:

$$a_0 = \beta \cos \gamma, \quad a_{\pm 1} = 0, \quad a_{\pm 2} = \frac{1}{\sqrt{2}} \beta \sin \gamma. \quad (2.72)$$

Here the parameters can take values in the range  $0 \leq \beta < +\infty$  and  $0^\circ \leq \gamma \leq 60^\circ$ , with  $\gamma = 0^\circ$  corresponding to axial prolate and  $\gamma = 60^\circ$  corresponding to axial oblate shapes. By inserting the parameter values into Eq. (2.71), a following relation for the boson coherent state is obtained [45]:

$$|\Phi(N_B, \beta, \gamma)\rangle = \frac{1}{\sqrt{N_B! (1 + \beta^2)^{N_B}}} \left[ s^\dagger + \beta \cos \gamma d_0^\dagger + \frac{1}{\sqrt{2}} \beta \sin \gamma (d_{+2}^\dagger + d_{-2}^\dagger) \right]^{N_B} |0\rangle. \quad (2.73)$$

For any operator  $\hat{O}$ , the expectation value of that operator in the boson coherent state is defined as [45]:

$$\langle \hat{O} \rangle = \langle \Phi(N_B, \beta, \gamma) | \hat{O} | \Phi(N_B, \beta, \gamma) \rangle. \quad (2.74)$$

In order to calculate the bosonic energy surface, the bosonic analogue of the PES of mean-field models, the expectation value of the Hamiltonian  $\hat{H}$  needs to be calculated in the boson coherent state. If a Hamiltonian from Eq. (2.49) is taken, by applying methods from Refs. [71, 72], the IBM surface is obtained:

$$\langle \hat{H} \rangle = \frac{\epsilon_d N_B \beta_B^2}{1 + \beta_B^2} + N_B (N_B - 1) \kappa \frac{\beta_B^2}{1 + \beta_B^2} \left[ 4 - 4\sqrt{\frac{2}{7}} \chi \beta_B \cos 3\gamma_B + \frac{2}{7} \chi^2 \beta_B^2 \right], \quad (2.75)$$

with  $(\beta_B, \gamma_B)$  representing the bosonic deformation parameters, which are different from the fermionic deformation parameters in the mean-field models. If only axial quadrupole deformations are considered, then  $\gamma_B = 0$  and the parameter  $\beta_B \equiv \beta_{2B}$  can now take on the values in the range  $-\infty < \beta_{2B} < +\infty$ , with  $\beta_{2B} < 0$  corresponding to oblate and  $\beta_{2B} > 0$  corresponding to prolate shapes. The expectation value of the Hamiltonian can then be written as:

$$\langle \hat{H} \rangle = \frac{\epsilon_d N_B \beta_{2B}^2}{1 + \beta_{2B}^2} + N_B (N_B - 1) \kappa \frac{\beta_{2B}^2}{1 + \beta_{2B}^2} \left[ 4 - 4\sqrt{\frac{2}{7}} \chi \beta_{2B} + \frac{2}{7} \chi^2 \beta_{2B}^2 \right]. \quad (2.76)$$

This way, the energy of the *sd*-IBM is expressed as a function of the bosonic quadrupole deformation, so the IBM is directly connected to the geometric model.

## 2.4.2 Geometric interpretation of the *sdg*-IBM

In the case of the *sdg*-IBM, the boson coherent state can be expanded with 9 more  $a_\mu$  parameters [65]:

$$|\Phi(N_B, \{a_\mu\})\rangle = \frac{1}{\sqrt{N_B! (1 + \sum_\mu a_\mu^2)^{N_B}}} \left[ s^\dagger + \sum_\mu a_\mu d_\mu^\dagger + \sum_\nu a_\nu g_\nu^\dagger \right]^{N_B} |0\rangle. \quad (2.77)$$

The boson coherent state is now defined with two quadrupole deformation parameters  $\beta_2$  and  $\gamma_2$  and three hexadecapole parameters  $\beta_4, \gamma_4$  and  $\delta_4$ , with  $\gamma_4$  appearing in the  $a_{\nu=\pm 2}$  parameter and  $\delta_4$  appearing in the  $a_{\nu=\pm 4}$  parameter [73]. Here, the deformation parameters are also bosonic parameters ( $\beta_2 \equiv \beta_{2B}, \beta_4 \equiv \beta_{4B}, \dots$ , but are written without the index  $B$  for simplicity. In order to reduce the number of deformation parameters, the triaxial hexadecapole parameters  $\gamma_4, \delta_4$  can be parametrized in terms of the quadrupole triaxial parameter  $\gamma_2$  [74]. The bosonic state



can then be written in the following way [65]:

$$\begin{aligned}
|\Phi(N_B, \beta_2, \beta_4)\rangle = & \frac{1}{\sqrt{N_B! (1 + \beta_2^2 + \beta_4^2)^{N_B}}} \left[ s^\dagger + \beta_2 \left( \cos \gamma_2 d_0^\dagger + \sqrt{\frac{1}{2}} \sin \gamma_2 [d_{-2}^\dagger + d_{+2}^\dagger] \right) \right. \\
& + \frac{1}{6} \beta_4 \left( [5 \cos^2 \gamma_2 + 1] g_0^\dagger + \sqrt{\frac{15}{2}} \sin 2\gamma_2 [g_{-2}^\dagger + g_{+2}^\dagger] \right. \\
& \left. \left. + \sqrt{\frac{35}{2}} \sin^2 \gamma_2 [g_{-4}^\dagger + g_{+4}^\dagger] \right) \right]^{N_B} |0\rangle. \tag{2.78}
\end{aligned}$$

Here, quadrupole parameters  $\beta_2$  and  $\gamma_2$  can take on the same value as  $\beta$  and  $\gamma$  from Eq. (2.72), while  $\beta_4$  can take on values in the range  $-\infty < \beta_4 < +\infty$ . If only axial deformations are taken into consideration, then  $\gamma_2 = 0$ , and  $\beta_2$  can take on any values in the range  $\langle -\infty, +\infty \rangle$ , just like  $\beta_4$ . The coherent state then becomes:

$$|\Phi(N_B, \beta_2, \beta_4)\rangle = \frac{1}{\sqrt{N_B! (1 + \beta_2^2 + \beta_4^2)^{N_B}}} (s^\dagger + \beta_2 d_0^\dagger + \beta_4 g_0^\dagger)^{N_B} |0\rangle. \tag{2.79}$$

The expectation value of the Hamiltonian from Eq. (2.61) is given by the following relation:

$$\begin{aligned}
\langle \hat{H}_{sdg} \rangle = & \frac{N_B \epsilon_d \beta_2^2}{1 + \beta_2^2 + \beta_4^2} + \frac{N_B \epsilon_g \beta_4^2}{1 + \beta_2^2 + \beta_4^2} + \frac{N_B (N_B - 1) \kappa}{(1 + \beta_2^2 + \beta_4^2)^2} \left[ 4\beta_2^2 - \chi \left( \frac{72}{7} \sqrt{\frac{2}{7}} \sigma \beta_2^2 \beta_4 \right. \right. \\
& + \frac{2}{7} \sqrt{\frac{5}{7}} [11\beta_2^3 + 10\beta_2 \beta_4^2] \left. \right) + \chi^2 \left( \frac{605}{1372} \beta_2^4 + \left[ \frac{648}{343} \sigma^2 + \frac{550}{588} \right] \beta_2^2 \beta_4^2 + \frac{3125}{6174} \beta_4^4 \right. \\
& \left. \left. + \frac{18\sqrt{10}}{343} \sigma [11\beta_2^3 \beta_4 + 10\beta_2 \beta_4^3] - \frac{25}{6174} [33\beta_2^2 \beta_4^2 + 35\beta_4^4] \right) \right] \\
& + \frac{4N_B (N_B - 1) \kappa (1 - \chi^2) \beta_4^2}{(1 + \beta_2^2 + \beta_4^2)}. \tag{2.80}
\end{aligned}$$

Using this equation, the IBM PES of the  $sdg$ -IBM model can be created. If  $\sigma = 1$ , the expectation value becomes equivalent to that of the Ref. [65].

### 2.4.3 The mapping method

In the mapping method [41, 42, 45, 47], the parameters of the IBM Hamiltonian are fitted so that the IBM PES approximates the SCMF PES in the vicinity of the minimum:

$$E_{SCMF}(\beta_{2F}, \beta_{4F}) \approx E_{IBM}(\beta_{2B}, \beta_{4B}). \quad (2.81)$$

Since the deformation parameters of the SCMF model are fermionic, and those of the IBM are bosonic, the question is how to relate them. In the case of the axial quadrupole - octupole mapping [47], it has been shown that a successful approximation can be created by assuming that the relationship between the parameters is linear:

$$\beta_{\lambda B} = C_{\lambda} \beta_{\lambda F}. \quad (2.82)$$

In this work, the same assumption was made for the axial quadrupole-hexadecapole mapping,  $\beta_{2B} = C_2 \beta_{2F}$ ,  $\beta_{4B} = C_4 \beta_{4F}$ . This leads, in the case of the *sdg*-IBM, to 7 independent parameters  $\epsilon_d, \epsilon_g, \kappa, \chi, \sigma, C_2$  and  $C_4$  that are determined by fitting the IBM PES of Eq. (2.80) to the SCMF PES. The IBM PES should reproduce some of the basic properties of the SCMF PES, such as the position of the minimum and the saddle point, as well as the overall shape of the SCMF PES. Due to the restricted boson space of the IBM, the IBM PES will almost always be somewhat larger and softer around the minimum than the SCMF PES, which is to be expected, since the SCMF calculations of the PES are significantly more complex. An illustration of the mapping method with axial quadrupole and axial hexadecapole deformation coordinates is shown in Figure 2.2. This way, a complete microscopic model, consisting of the RMF and *sdg*-IBM calculations, is constructed, and can be utilised to study and predict the effects of axial quadrupole and hexadecapole collectivity in nuclei.

In the case of the mapped *sd*-IBM, which was used in order to compare the results with the *sdg*-IBM results and examine the effects of hexadecapole correlations via the *g* boson, the mapping is simplified, since the only deformation parameter is the quadrupole one, and the relation between the bosonic and the fermionic parameter is  $\beta_{2B} = C_2 \beta_{2F}$ . This leads to a total of 4 independent parameters  $\epsilon_d, \kappa, \chi, C_2$  that need to be determined by fitting the one-dimensional *sd*-IBM PES of Eq. (2.76) to the SCMF PES along the  $\beta_4 = 0$  line in the vicinity of the minimum. Some of the properties that need to be reproduced are the positions of the minimum and the saddle point, as well as the energy of the spherical  $\beta_2 = 0$  maximum. With this, a microscopic model, designed for describing axial quadrupole collectivity in nuclei, is constructed, and is used for a comparison with the more complex *sdg*-IBM, in order to study

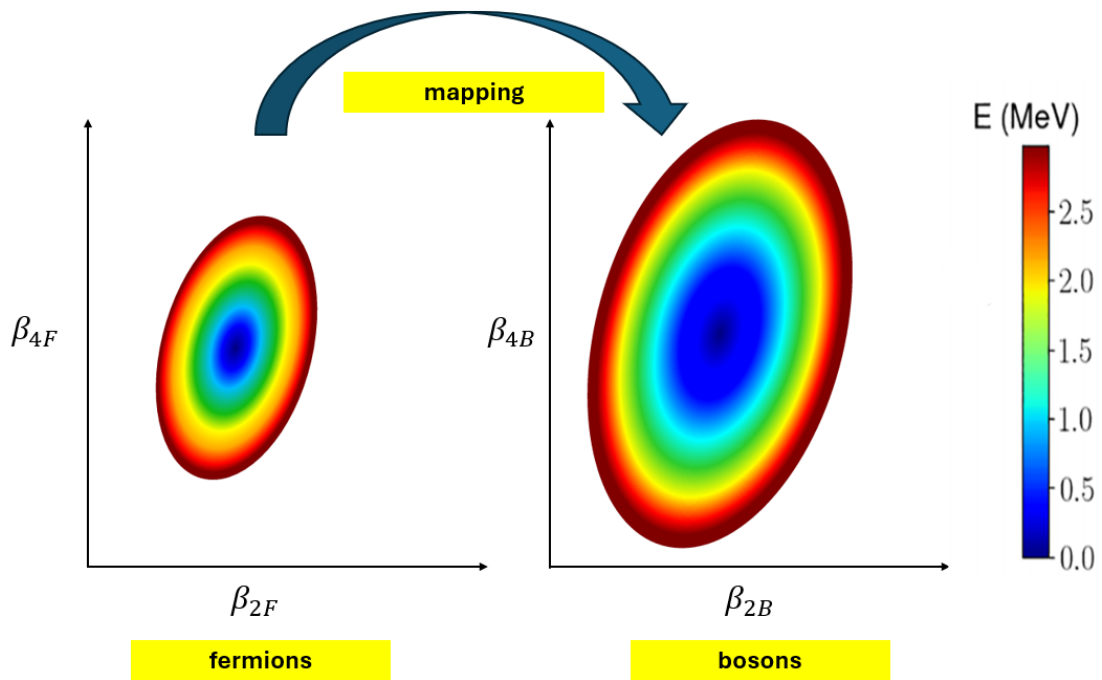


Figure 2.2: An illustration of the mapping method in the axial quadrupole-hexadecapole plane. The SCMF PES is shown on the left, and the IBM approximation of the SCMF PES is shown on the right. The energy is shown up to 3 MeV.

the effects of axial hexadecapole collectivity in nuclei.

# Chapter 3

## Results

In this chapter, results of the mapped *sdg*-IBM are presented, as well as the results of the mapped *sd*-IBM for comparison. In the first part, results of the RMF calculations are presented, as well as the IBM reproductions of the RMF PESs. Parameter values of the *sdg*- and *sd*-IBM, obtained from the fit, are also presented. In the second part, the energies of the yrast band, as well as those of the  $0^+$  and  $\gamma$ -vibrational band, are calculated by both *sdg*- and *sd*-IBM and compared, and the necessity of including the *g* boson in the IBM is discussed. Finally, in the last part, the calculated quadrupole, hexadecapole and monopole transition strengths are shown and discussed. All the calculated energies and transition strengths are compared with the available experimental data. For SCMF calculations, the code MDCRHB [54] was used. For IBM calculations of energies and transition strengths, both *sdg*- and *sd*-IBM, the code ARBMODEL [75] was used, which lets the user construct its own Hamiltonian. The experimental data are taken from the NNDC website [50], unless indicated otherwise.

### 3.1 SCMF calculations and the mapping method

#### 3.1.1 SCMF calculations

The axially symmetric quadrupole  $\beta_2$  and hexadecapole  $\beta_4$  PESs of  $^{144-154}\text{Nd}$ ,  $^{146-156}\text{Sm}$ ,  $^{148-158}\text{Gd}$ ,  $^{150-160}\text{Dy}$  and  $^{152-162}\text{Er}$ , obtained from the SCMF calculations with the DD-PC1 functional, are shown in Figures 3.1–3.5. Figures are taken from Ref. [76]. The energy difference between the neighbouring contours is 0.1 MeV, and the PESs are shown in the energy range up to 2.7 MeV. The positions of the energy minima are indicated by the open downward triangle. The  $N = 96$  nuclei are left out due to their PESs being similar to the  $N = 94$  nuclei. The results are consistent with previous constrained mean-field calculations in the  $\beta_2 - \beta_4$

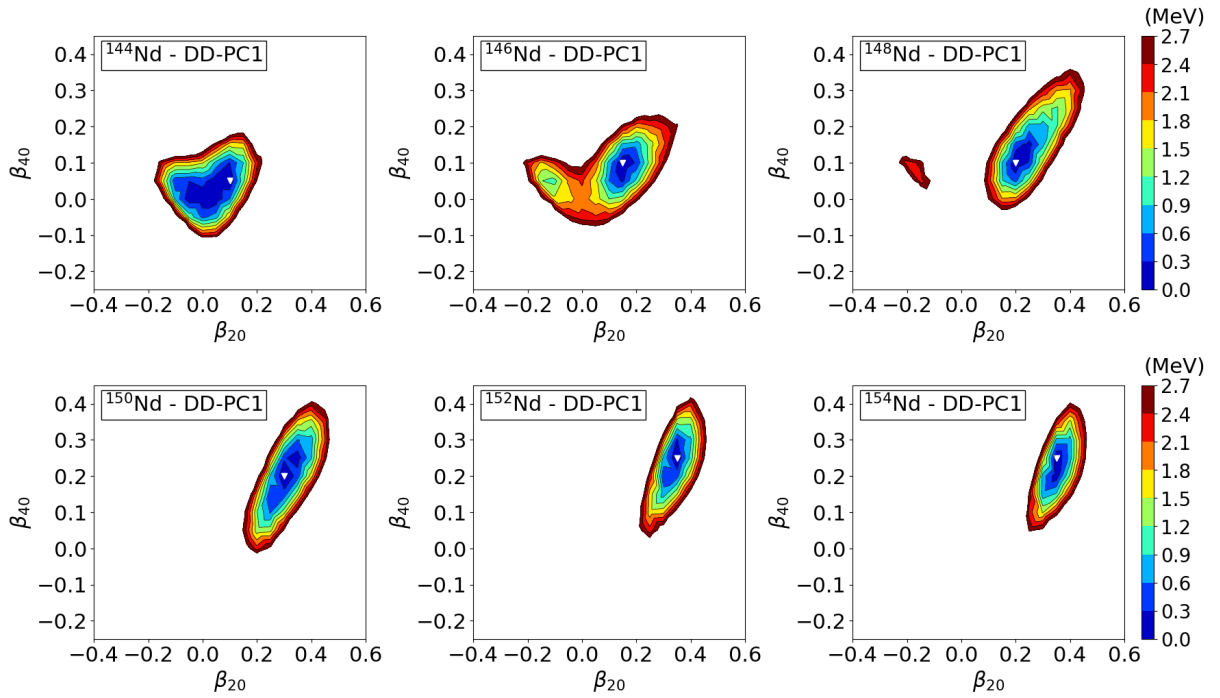
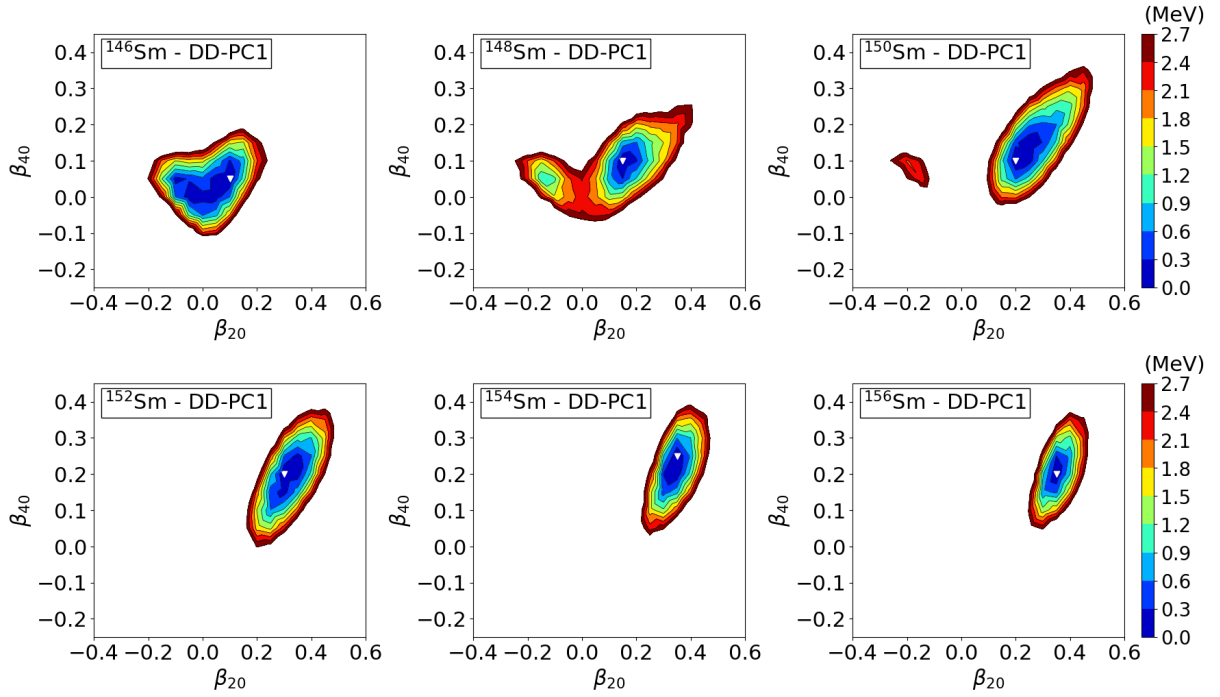
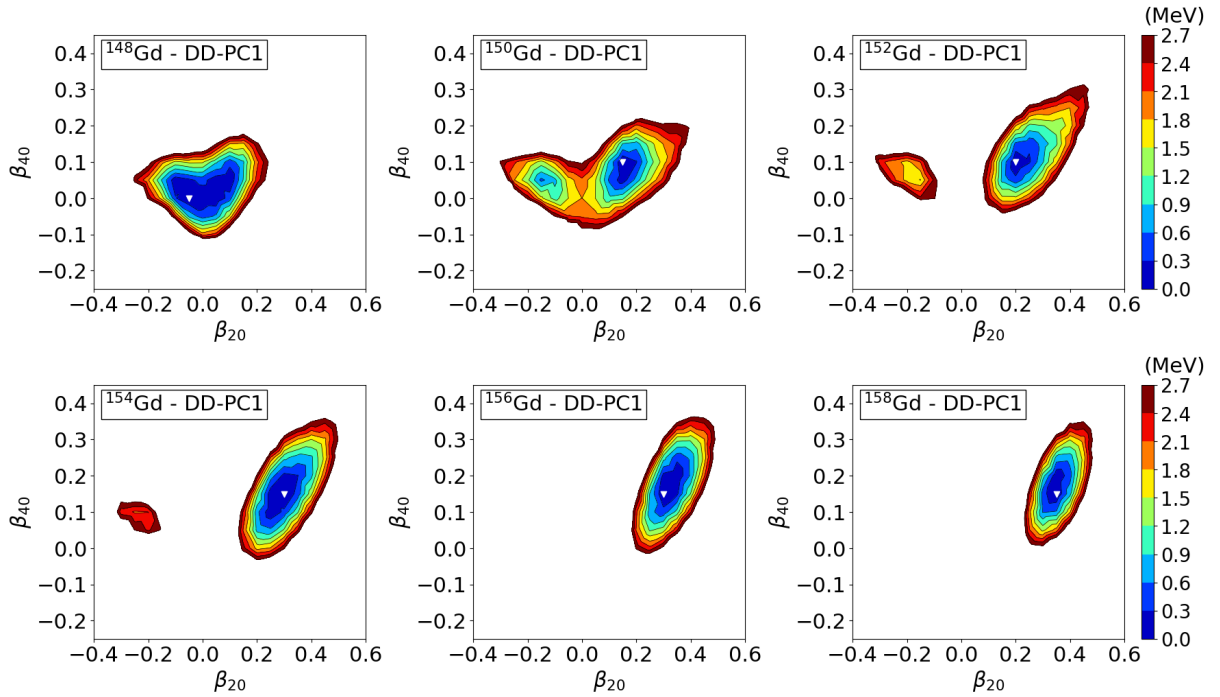
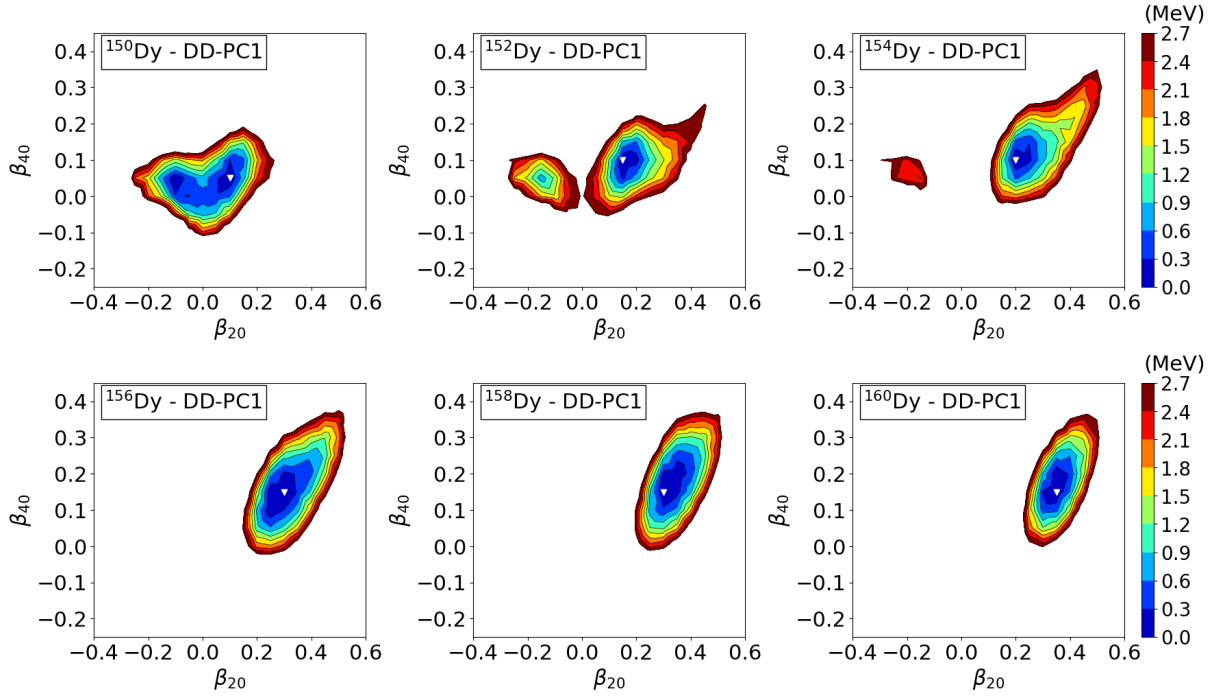
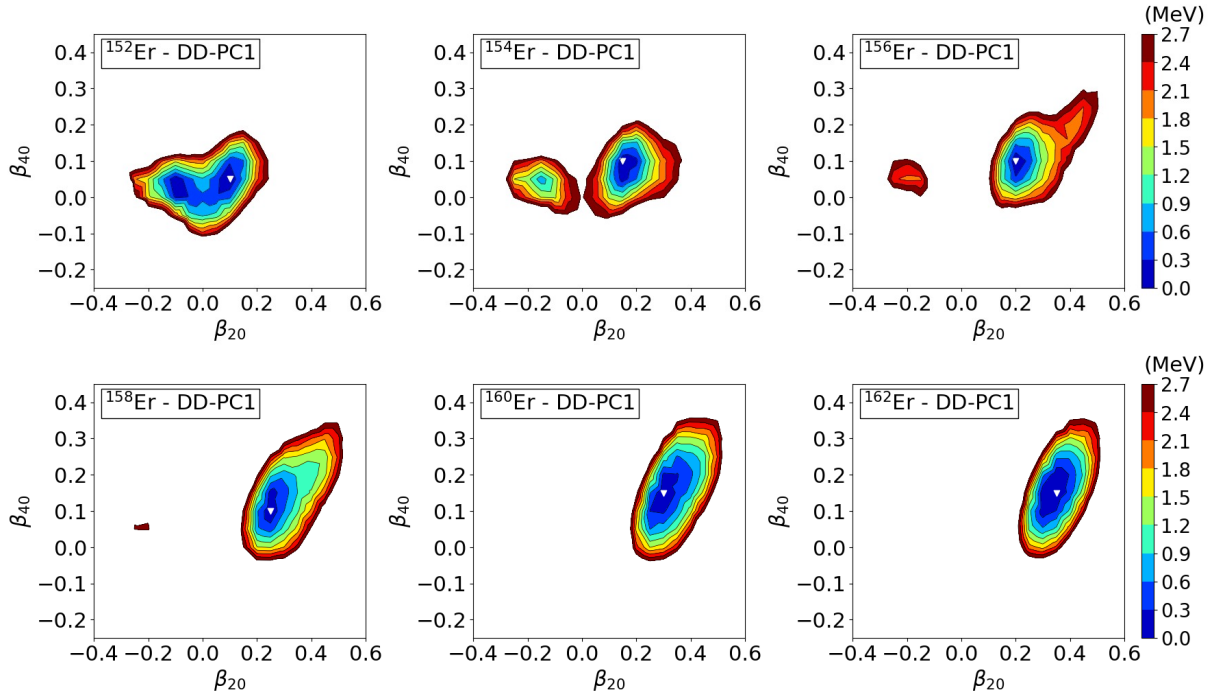


Figure 3.1: Axially-symmetric quadrupole ( $\beta_{20}$ ) and hexadecapole ( $\beta_{40}$ ) constrained energy surfaces for the  $^{144-154}\text{Nd}$  isotopes calculated within the relativistic Hartree-Bogoliubov method using the DD-PC1 energy density functional and the pairing force of finite range. Energy difference between neighbouring contours is 0.1 MeV, and the absolute minimum is indicated by an open triangle. Figure is taken from Ref. [76]

plane, which have been performed using the axially-deformed Woods-Saxon potential [74, 77] and the Gogny force [78].

The energy evolution, with respect to the neutron number  $N$ , in the  $\beta_2$  direction is similar for all nuclei. In near-spherical  $N = 84$  nuclei, the PES shows a considerable softness in the  $\beta_2$  direction, which is more pronounced in lighter  $^{144}\text{Nd}$  and  $^{146}\text{Sm}$  isotopes, compared to the heavier  $^{148}\text{Gd}$ ,  $^{150}\text{Dy}$  and  $^{152}\text{Er}$  isotopes. The minimum in  $N = 84$  isotones is located at  $\beta_{2\text{min}} = 0.1$ , except for  $^{148}\text{Gd}$ , which has an oblate quadrupole minimum at  $\beta_{2\text{min}} = -0.05$  MeV. This is not surprising given that the energy differences between energies in the oblate and prolate region near  $\beta_2 = 0$  are very small, so the SCMF calculations could yield an oblate minimum instead of the prolate one. The softness in energy disappears in  $N = 86$  nuclei, and the saddle point in the oblate region becomes higher in energy as the  $N$  increases, and disappears from the PES in  $N > 90$  nuclei. The quadrupole deformation in the minimum increases with  $N$ , with the maximum quadrupole deformation in the minimum being  $\beta_{2\text{min}} = 0.35$ . In Nd and Sm isotopes, this  $\beta_{2\text{min}}$  value appears for  $N \geq 92$ , while in Gd, Dy and Er, it is achieved for neutron numbers

Figure 3.2: Same as the caption for Fig. 3.1, but for  $^{146-156}\text{Sm}$ Figure 3.3: Same as the caption for Fig. 3.1, but for  $^{148-158}\text{Gd}$ . SCMF calculations for Gd can also be found in Ref. [79].

Figure 3.4: Same as the caption for Fig. 3.1, but for  $^{150-160}\text{Dy}$ Figure 3.5: Same as the caption for Fig. 3.1, but for  $^{152-162}\text{Er}$

$N = 94, 96$ .

In the  $\beta_4$  direction, the evolution is also similar for all nuclei. In  $N = 84$  nuclei, the energy surface is also characterized by a considerable softness, especially pronounced in the  $^{144}\text{Nd}$  and  $^{146}\text{Sm}$ . The softness disappears in  $N = 86$  nuclei, and the energy in the region of negative hexadecapole deformations becomes larger than 2.7 MeV in  $N > 86$  nuclei, so the energy surface is not visible in that region. In  $N = 84$  isotones, the hexadecapole minimum is located at  $\beta_{4\text{min}} = 0.05$ , except for  $^{148}\text{Gd}$ , which is predicted to have no presence of hexadecapole deformation in the ground state. Due to the softness of the PES, the hexadecapole correlations are still expected to play a role in  $^{148}\text{Gd}$ . As  $N$  increases, the hexadecapole minima also increase in value, just like quadrupole deformation minima. The difference is that, the hexadecapole minima remain the same ( $\beta_{4\text{min}} = 0.1$ ) when moving from the spherical vibrational  $N = 86$  region into the transitional  $N = 88$  region. The value of  $\beta_{4\text{min}}$  continues to increase in the deformed region. The larger  $\beta_{4\text{min}}$  values are calculated in deformed Nd and Sm isotopes, with the largest value of  $\beta_{4\text{min}} = 0.25$  obtained for  $^{152,154}\text{Nd}$  and  $^{154}\text{Sm}$ , while the  $\beta_{4\text{min}} = 0.2$  value is calculated in  $^{150}\text{Nd}$  and  $^{152,156}\text{Sm}$ . On the other hand, the largest hexadecapole minimum value in Gd, Dy and Er isotopes is  $\beta_{4\text{min}} = 0.15$ , which indicates a smaller presence of hexadecapole collectivity in those isotopes.

### 3.1.2 Mapping the SCMF calculations onto the *sdg*-IBM space

The *sdg*-IBM approximations of SCMF PESs from Subsection 3.1.1 are shown in Figures 3.6-3.10. The IBM PESs were calculated using the expectation value of the Hamiltonian from Eq. (2.80). Figures can also be found in Ref. [76]. What can be seen from the figures is that the *sdg*-IBM successfully reproduces some of the basic properties of SCMF PESs such as the position of the absolute minimum, the saddle point, and the reproduction of the shape of the PES is satisfying. The PESs are significantly enlarged compared to the SCMF ones. This is not surprising, since, as was discussed in Chapter 2, the SCMF calculations are significantly more complex and can account for more interaction effects between the nucleons, and the boson model space is very restricted. This problem appears both in the case of the axial - triaxial quadrupole mapping, performed on Sm isotopes [42], and especially in the case of axial quadrupole - octupole mapping, performed on a wide range of nuclei, from medium-heavy to actinides [47]. The characteristic "tail-like" shape in  $N = 88$  transitional nuclei, predicted by the SCMF calculations, is not predicted in the IBM, which can again be attributed to the simplicity of the IBM PES calculations compared to the SCMF calculations. One can also notice that the shape of the  $N = 84, 86$  nuclei is better reproduced in Nd and Sm isotopes, compared to the heavier isotopes. This can be attributed to the fact that the fit in those nuclei yielded larger values of the  $\sigma$



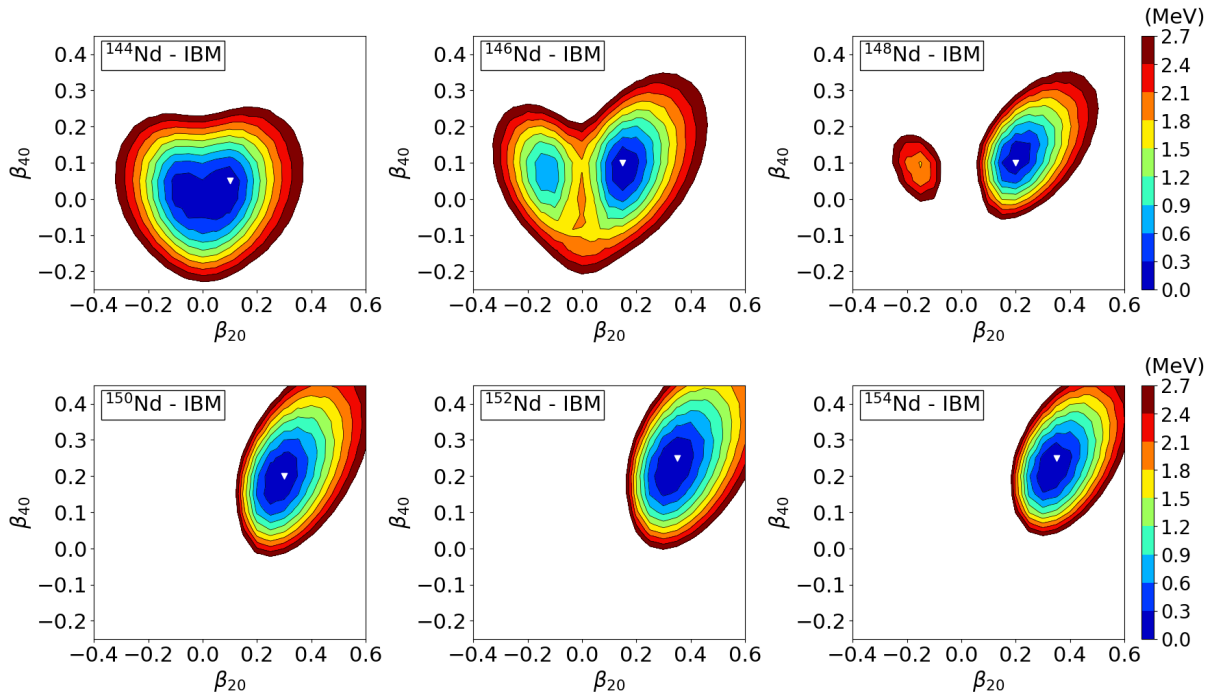
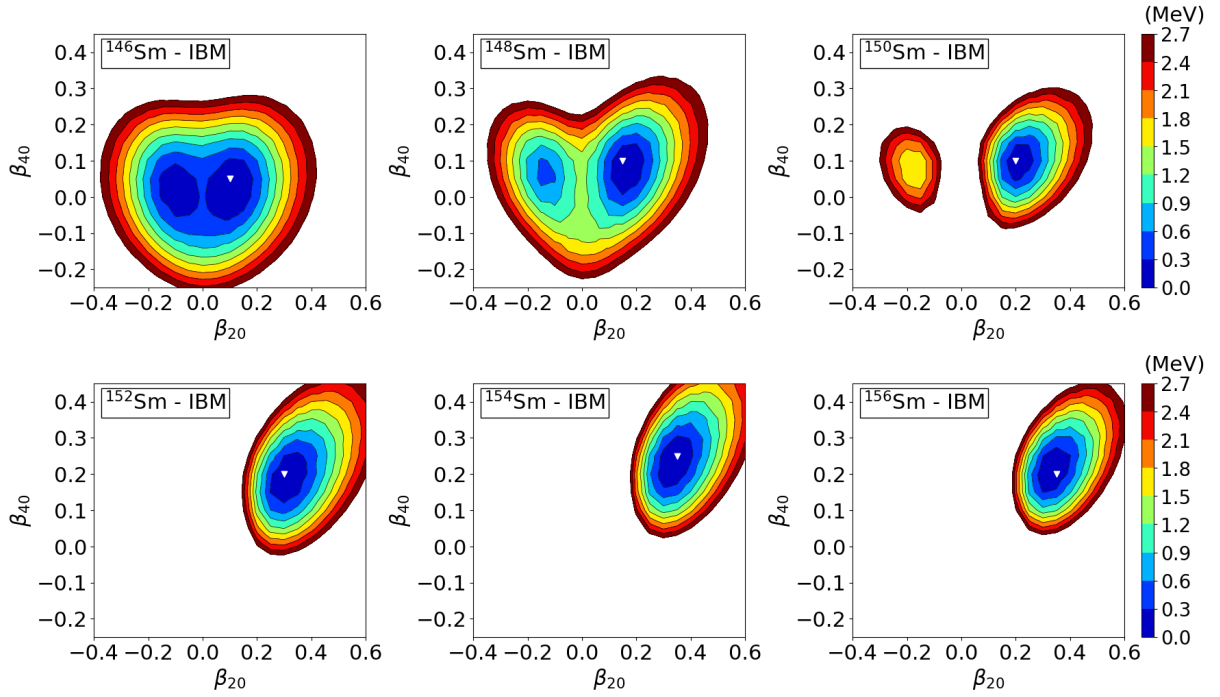
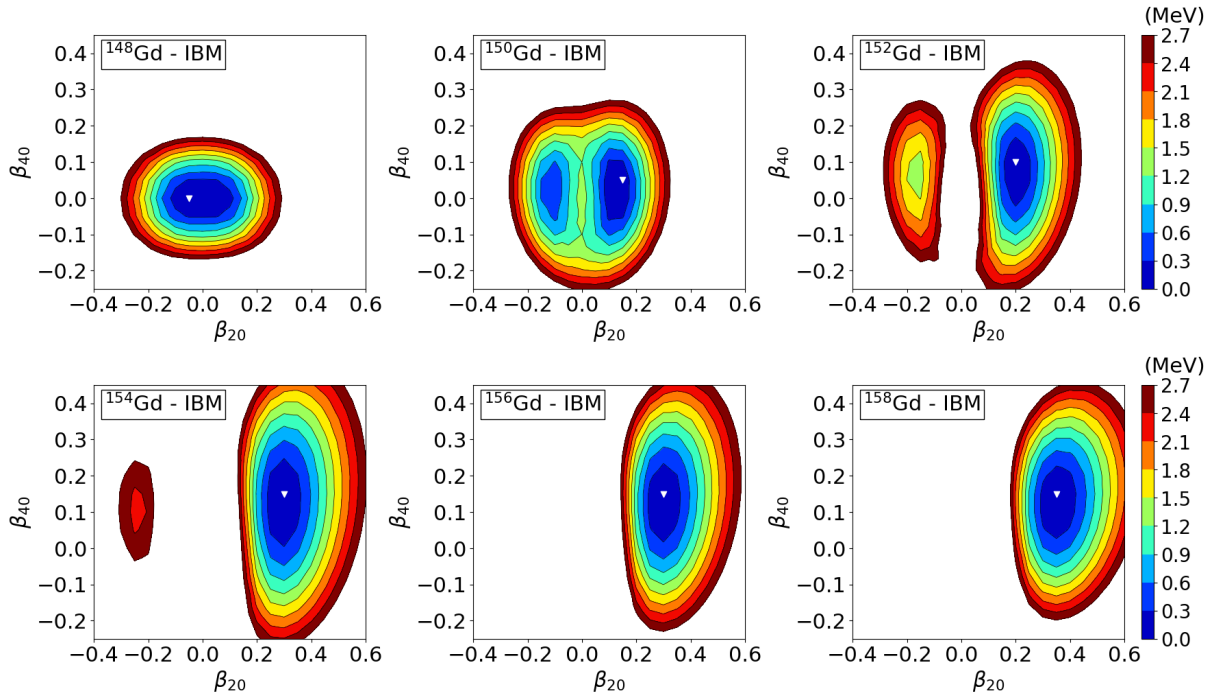
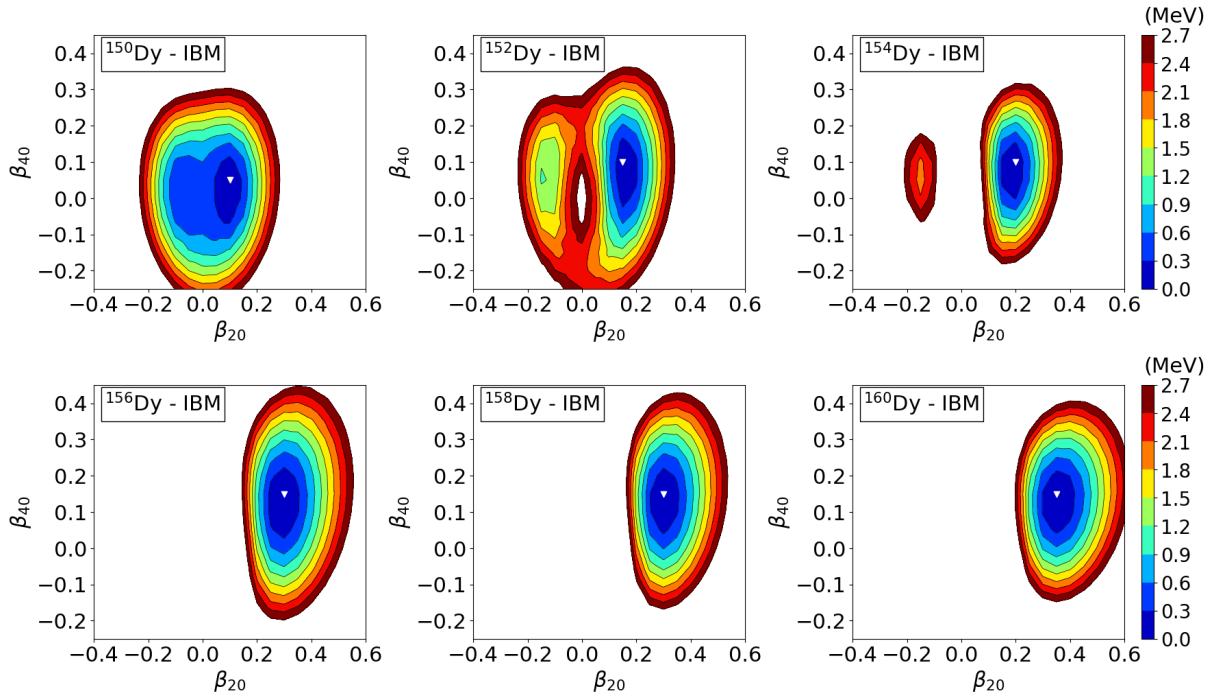
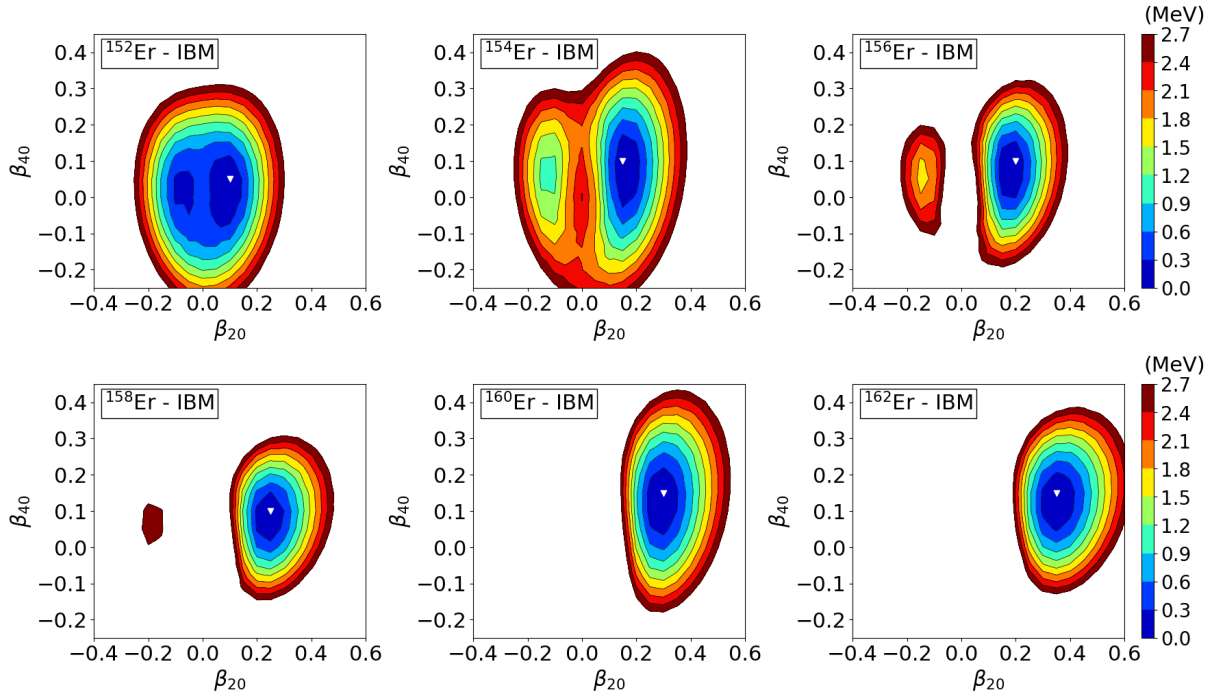


Figure 3.6: The *sdg*-IBM axially-symmetric quadrupole ( $\beta_{20}$ ) and hexadecapole ( $\beta_{40}$ ) PESs of  $^{144-154}\text{Nd}$  isotopes. The energies are shown up to 2.7 MeV, and the energy difference between the neighbouring contours is 0.1 MeV. Figure is taken from Ref. [76].

parameter of the quadrupole operator from Eq. (2.62). Larger values of  $\sigma$  cause the shapes to "bend" and become less symmetrical in both  $\beta_2$  and  $\beta_4$  directions. It should be noted that the inclusion of more two-body interactions in the *sdg*-IBM could lead to a better reproduction of the PES, however, this would also lead to more independent parameters and the symmetry limit conditions would become significantly more complicated, so such an extension to the model is left for a different study. The inclusion of three-body terms could also potentially improve the IBM PES calculations, as was shown in the case of the quadrupole axial-triaxial mapping [44], however, such terms are rarely included in the Hamiltonian, and the inclusion of *g* bosons would significantly complicate those terms, so this is also left for a separate study.

Figure 3.11 shows the values of the *sdg*-IBM Hamiltonian parameters, and the values of parameters  $C_2$  and  $C_4$ , as a function of the valence boson number  $N_B$ . The parameter not shown in the figure is the  $\sigma$  parameter. The obtained  $\sigma$  values are  $\sigma = 3.5$  for  $^{144,146}\text{Nd}$  and  $^{146,148}\text{Sm}$ , and  $\sigma = 2.8$  for the remaining Nd and Sm isotopes. In Gd, Dy and Er isotopes, the obtained value from the fit is  $\sigma = 1.0$ . The reason for  $\sigma$  being equal to 1.0 in heavier isotopes is that these isotopes are characterized by larger valence boson numbers  $N_B$ , and the obtained hexadecapole minima could not be reproduced with  $\sigma > 1.0$  in those isotopes. It should also be mentioned

Figure 3.7: Same as the caption for Fig. 3.6, but for  $^{146-156}\text{Sm}$ Figure 3.8: Same as the caption for Fig. 3.6, but for  $^{148-158}\text{Gd}$ . The *sdg*-IBM PES calculations for Gd can also be found in Ref. [79].

Figure 3.9: Same as the caption for Fig. 3.6, but for  $^{150-160}\text{Dy}$ Figure 3.10: Same as the caption for Fig. 3.6, but for  $^{152-162}\text{Er}$

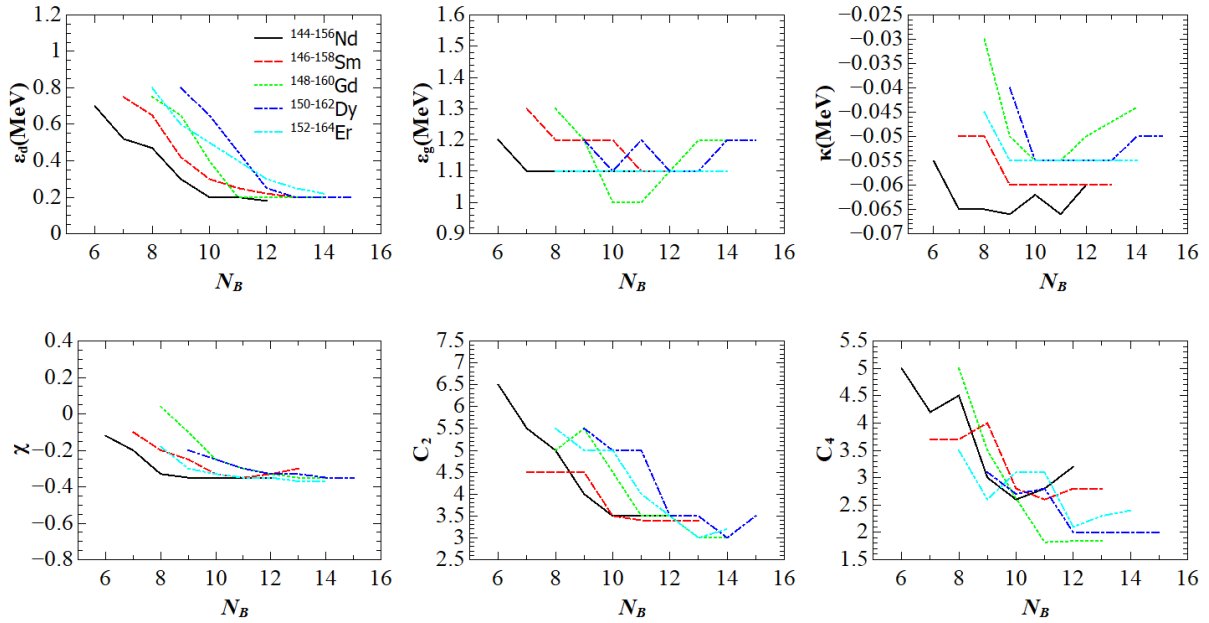


Figure 3.11: Parameters of the *sdg*-IBM Hamiltonian of Eq. (2.61), and the  $C_2, C_4$  parameters relating fermionic and bosonic deformation parameters. The figure can be found in Ref. [76].

that the positive  $\sigma$  values correspond to positive, while negative  $\sigma$  values correspond to negative hexadecapole deformations in the minimum. The  $d$  boson energy  $\epsilon_d$  achieves its maximum in spherical vibrational nuclei, and decreases as the number of valence bosons increases. The smaller values of  $\epsilon_d$  correspond to larger quadrupole deformations in the ground state. The  $g$  boson energy,  $\epsilon_g$ , fluctuates between 1.0 and 1.3 MeV. The  $\epsilon_g$  parameter affects the hexadecapole deformations in the minimum, with larger  $\epsilon_g$  values corresponding to smaller  $\beta_{4\min}$  values. The  $\kappa$  parameter tends to increase in absolute value when moving into the deformed region, and usually decrease at the end of the deformed region, where the deformation parameter values in the minima stop increasing, or even start decreasing in certain isotopes, e.g.  $^{162}\text{Dy}$ . The  $\chi$  parameter is negative in value, which corresponds to prolate quadrupole deformations in the minimum, except for  $^{148}\text{Gd}$ , where the  $\chi = 0.04$  positive value is required in order to reproduce the small oblate  $\beta_{2\min} = -0.05$  quadrupole deformation in the minimum. The  $\chi$  parameter decreases with the valence boson number  $N_B$ , with the lowest value  $\chi = -0.35$  achieved in the well-deformed region. Finally, parameters  $C_2$  and  $C_4$  decrease with the valence boson number, since smaller values of  $C_2$  and  $C_4$  correspond to larger quadrupole and hexadecapole deformation values in the minimum, respectively. In the  $C_4$  graph, one can see that there is a slight increase in the  $C_4$  value when moving from the  $N = 86$  to the transitional  $N = 88$  nuclei. This happens because

the hexadecapole deformation does not increase with the neutron number, while the quadrupole deformation does, so the larger  $C_4$  value in the  $N = 88$  nucleus gives a better PES reproduction. It should also be noted that the smaller  $C_4$  values tend to enlarge the energy surface, while also increasing the  $\beta_{4\min}$  value.

### 3.1.3 Mapping the SCMF calculations onto the $sd$ -IBM space

The  $sd$ -IBM approximations of SCMF PESs along the  $\beta_4 = 0$  line are shown in Figures 3.12–3.16. The results of the SCMF calculations with the DD-PC1 functional are represented by a solid black line, while the  $sd$ -IBM approximations of the SCMF calculations along the  $\beta_4 = 0$  line are represented by a solid red line. The results for  $N = 96$  nuclei are not shown due to their similarity with the results for  $N = 94$  nuclei. The  $\beta_4 = 0$  PES of the  $sd$ -IBM was calculated using the expectation value of the  $sd$ -IBM Hamiltonian of Eq. (2.76). What can be seen from the figures is that the energy line in near-spherical nuclei is symmetrical near  $\beta_2 = 0$ , however, the symmetry disappears for  $|\beta_2| > 0.2$ , as the calculated energies in the oblate deformed region become significantly larger from the energies in the prolate deformed region. The symmetry around  $\beta_2 = 0$  disappears as  $N$  increases, with the maximum at  $\beta_2 = 0$  becoming more pronounced and larger in energy, and with the saddle point in the oblate region becoming significantly larger in energy from the absolute minimum. The calculated quadrupole minima are smaller in value from the ones obtained in the  $\beta_2 - \beta_4$  constrained calculations, which is expected, since hexadecapole deformation parameters are excluded from the calculations. The  $sd$ -IBM calculations approximate the SCMF energies well. The minima and the energies around the minima are well reproduced, as well as the energy maximum at  $\beta_2 = 0$  and the saddle point in the oblate region. The energies calculated for large  $\beta_2$  values, particularly in the oblate region, are significantly underestimated compared to the energies of the SCMF calculations. This is analogous to the enlargement of the PES in the  $sdg$ -IBM surfaces, and is expected, since the  $sd$ -IBM is a significantly simpler model for calculating the energy as a function of the  $\beta_2$  deformation parameter, and since the  $sd$  boson space is very restricted. A very small  $\beta_2 = 0$  maximum is predicted by the SCMF calculations in  $^{154}\text{Gd}$ , as can be seen from Figure 3.14. This cannot be reproduced with the  $sd$ -IBM calculations, which overestimate the energy of this maximum by almost 2 MeV. This does not occur in other  $N = 90$  nuclei, and can probably be attributed to the choice of the EDF for this particular nucleus.

Figure 3.17 shows the values of the  $sd$ -IBM Hamiltonian parameters, and the values of the parameter  $C_2$ , as functions of the boson number  $N_B$ . It is useful to compare the values of the  $\varepsilon_d, \kappa, \chi$  and  $C_2$  parameters to their  $sdg$ -IBM analogues. The  $\varepsilon_d$  parameter, representing the  $d$  boson energy, shows a similar behaviour in both models. In near spherical nuclei, the values

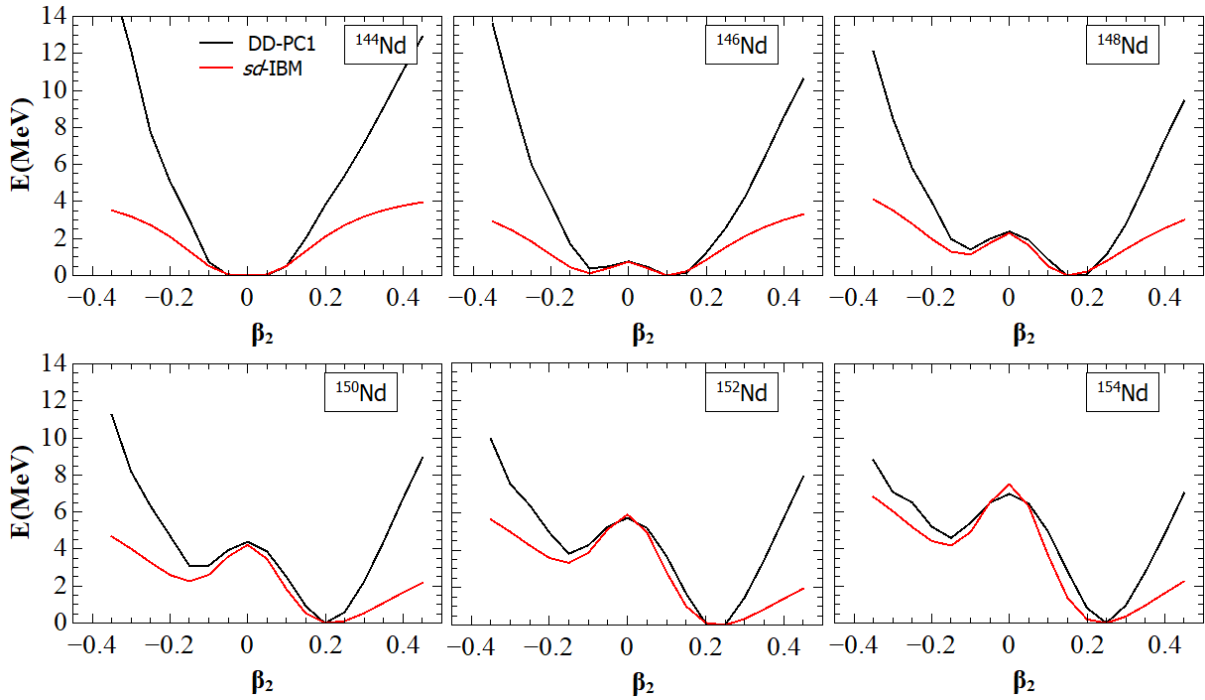
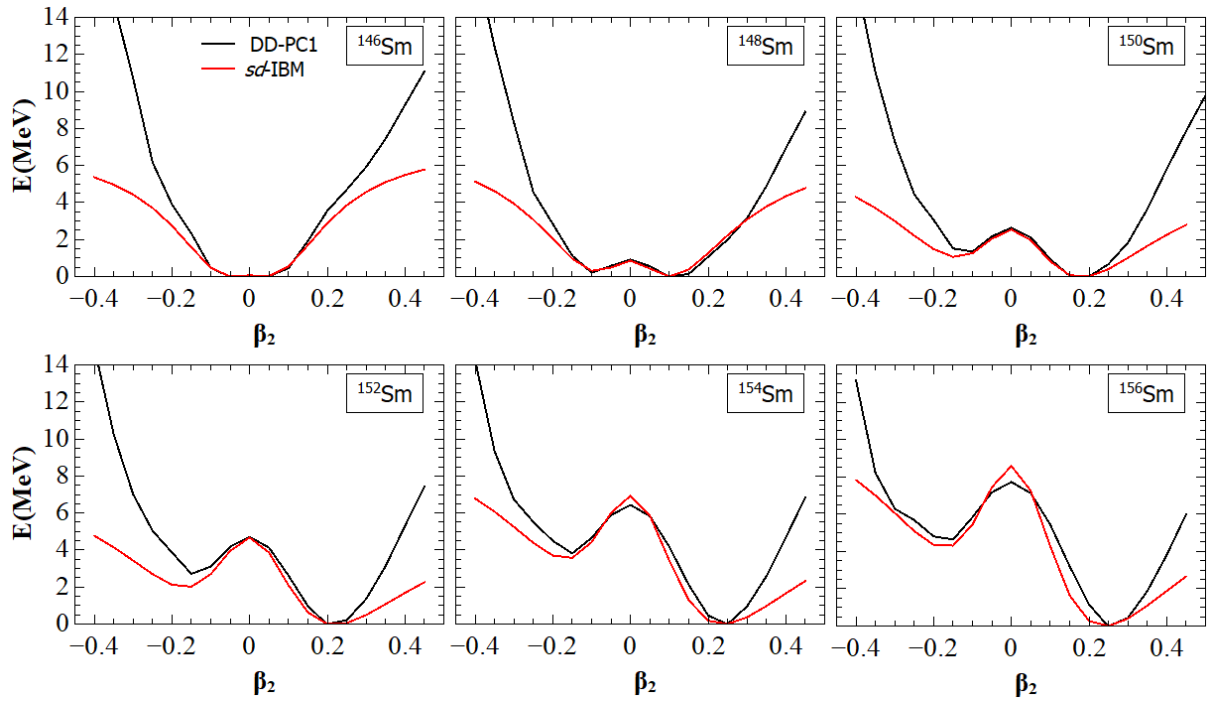
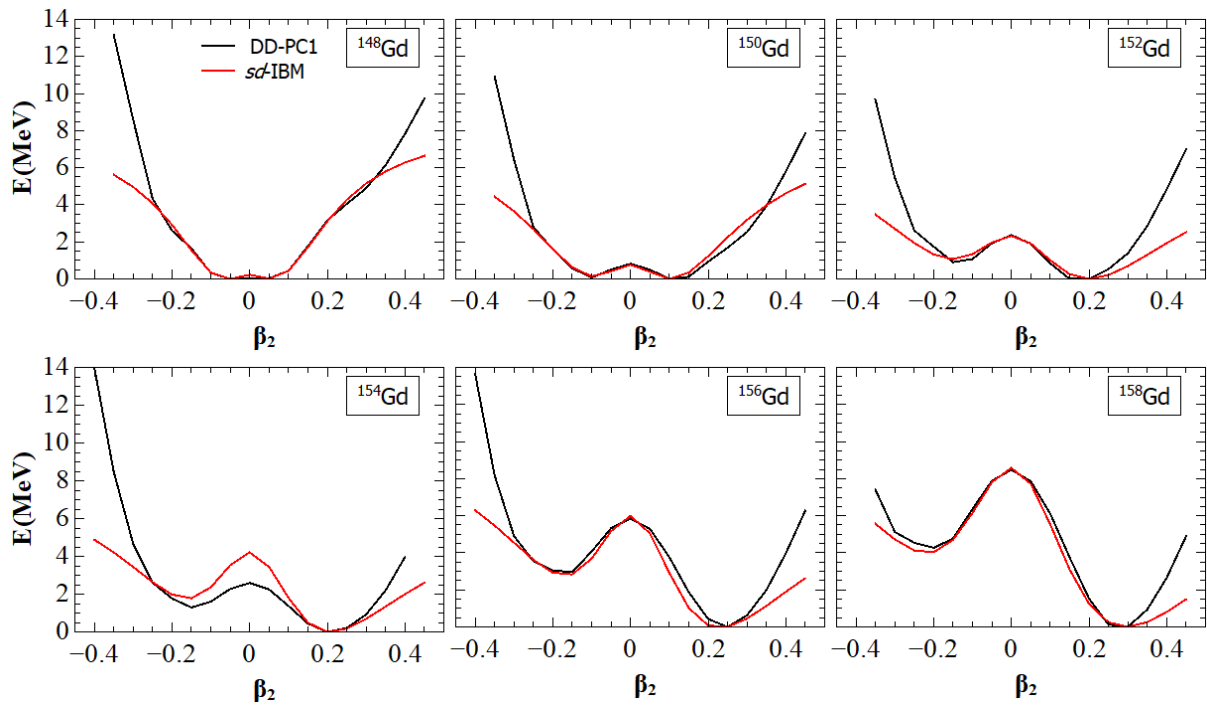
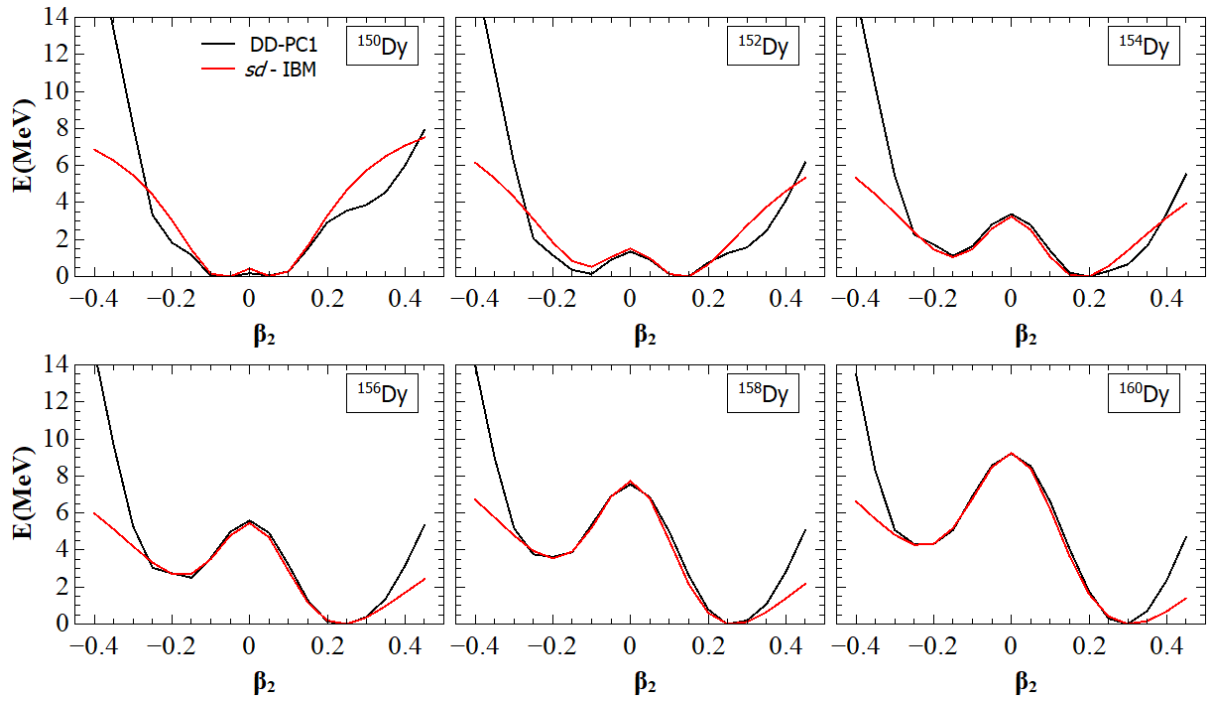
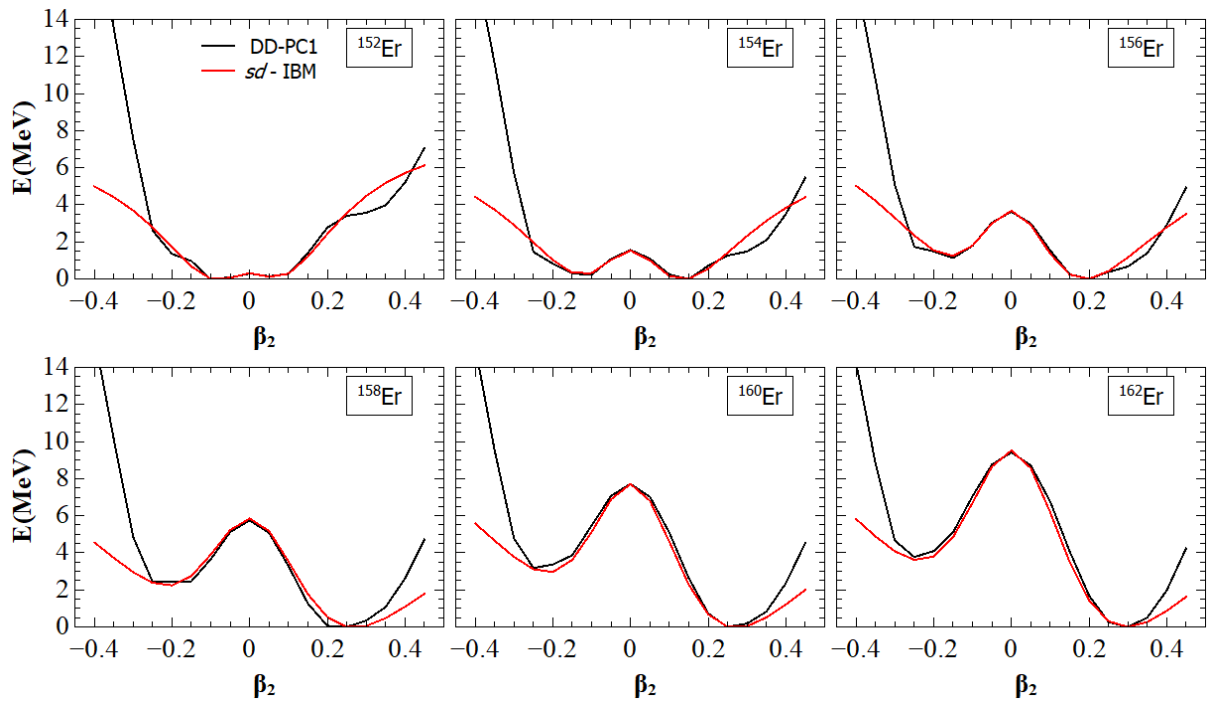


Figure 3.12: The energies of the SCMF calculations (solid black line) and *sd*-IBM approximations of those energies (solid red line), as functions of the axial quadrupole deformation parameter  $\beta_2$  for  $^{144}$ – $^{154}$ Nd isotopes. The energies are shown up to 14 MeV.

of the *d* boson energies are around  $\varepsilon_d \approx 1.0$  MeV, and the values decrease as the  $N_B$  increases. The predicted  $\varepsilon_d$  values near neutron shell closure are somewhat larger than the ones predicted by the mapped *sdg*-IBM model, which are around  $\varepsilon_d \approx 0.8$  MeV. This can be attributed to the fact that most of the minima of near-spherical nuclei in the SCMF  $\beta_2 - \beta_4$  calculations are predicted to be around  $\beta_2 = 0.1, \beta_4 = 0.05$  for  $N = 84$  nuclei, and  $\beta_2 = 0.15, \beta_4 = 0.1$  for  $N = 86$  nuclei, while in the SCMF  $\beta_2, \beta_4 = 0$  calculations, the predicted minima are in the oblate region for  $N = 84$  nuclei, and while the minimum is predicted to be around  $\beta_2 = 0.15$  in  $N = 86$  nuclei, the energy difference from the  $\beta_2 = -0.15$  saddle point is very small. To reproduce this, large  $\varepsilon_d$  values are required. In the well-deformed region, the values of  $\varepsilon_d$  are similar in both models. The  $\kappa$  parameter behaves similarly in both models. It increases in absolute value as  $N_B$  increases, and starts increasing at the end of the well-deformed region. The exception to this are the Gd isotopes, where  $\kappa$  starts increasing in absolute value after  $^{154}\text{Gd}$ . This can be attributed to the very low  $\beta_2 = 0$  energy maximum predicted by the SCMF calculation in Figure 3.14. The  $\chi$  parameter follows a similar trend in both models, decreasing as  $N_B$  increases. The main difference is that, in the *sd*-IBM, the  $\chi$  parameter starts from positive values in near-spherical nuclei, which can be explained by the oblate deformations being predicted in the minima by

Figure 3.13: Same as the caption for Fig. 3.12, but for  $^{146-156}\text{Sm}$ Figure 3.14: Same as the caption for Fig. 3.12, but for  $^{148-158}\text{Gd}$ .

Figure 3.15: Same as the caption for Fig. 3.12, but for  $^{150-160}\text{Dy}$ Figure 3.16: Same as the caption for Fig. 3.12, but for  $^{152-162}\text{Er}$



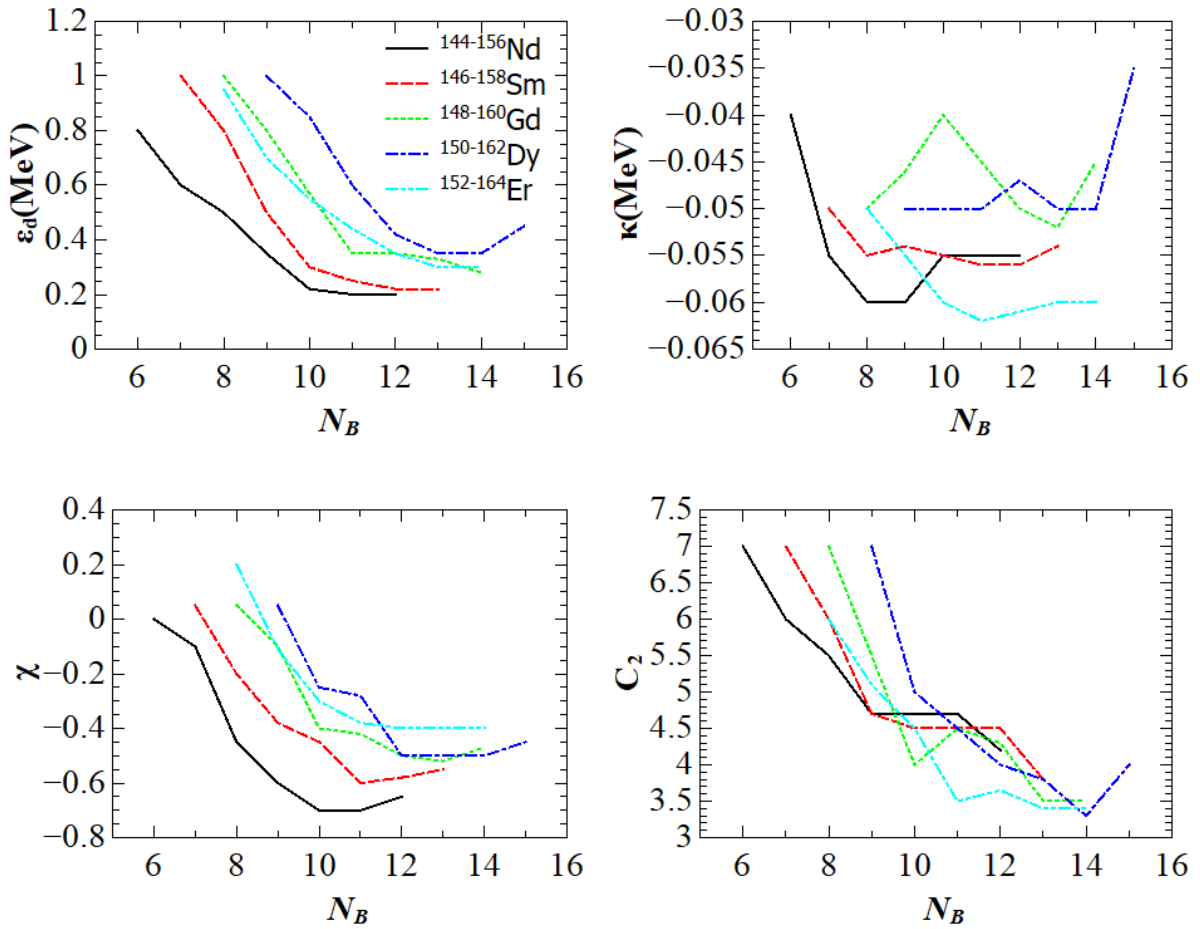


Figure 3.17: Parameters of the  $sd$ -IBM Hamiltonian of Eq. (2.49), and the  $C_2$  parameter relating the fermionic and bosonic  $\beta_2$  deformation parameter. The figure can be found in Ref. [76].

the  $\beta_4 = 0$  SCMF calculations, and decreases more sharply when moving into the deformed region. The values of  $\chi$  in the deformed region are significantly lower from those obtained by the mapped  $sdg$ -IBM. The behaviour of the  $C_2$  parameter is similar to that of the  $\epsilon_d$ . It also has a tendency to decrease as  $N_B$  increases, similarly to the  $C_2$  parameter in the  $sdg$ -IBM, however, larger values are obtained by the  $sd$ -IBM for near-spherical nuclei.

## 3.2 Results of the spectroscopic calculations

In this section, the excitation energies and transition strengths, calculated by both the mapped  $sdg$ -IBM and the mapped  $sd$ -IBM, are shown. The results are compared with the data from the

NNDC website [50].

### 3.2.1 Excitation energies

#### Ground state band

The calculated excitation energies of the yrast band states with spin  $J^\pi = 2^+ - 14^+$  are plotted as functions of the neutron number  $N$ , and are shown in Figure 3.18. The *sdg*-IBM provides a significant improvement in the description of the  $J^\pi \geq 6^+$  energy states in  $N = 84, 86$  nuclei over the simpler *sd*-IBM, which significantly overestimates the energies compared to the measured values. As  $N$  increases, the differences between the energies calculated by the *sdg*- and *sd*-IBM become less pronounced, and in the well-deformed region, there are no significant differences between the results obtained with the two models. The exception to this are isotopes of Nd and Sm, where the *sdg*-IBM provides an improvement of the  $J^\pi = 12^+, 14^+$  states even in some nuclei with  $N \geq 88$ , albeit a less significant improvement than the one in near-spherical nuclei. The lowering of the energy of the yrast states is associated with the presence of the  $g$  boson in those states, which is shown in Figure 3.19. As can be seen from the Figure, the  $g$  boson is present in  $J^\pi \geq 6^+$  states in near-spherical  $N = 84, 86$  nuclei. As  $N$  increases, the expectation value of the  $\hat{n}_g$  decreases, and in the deformed regions of Gd, Dy and Er, none of the yrast band states seem to have the presence of the  $g$  boson. This is different from the Nd and Sm isotopes, in which the  $g$  boson is present in the  $J^\pi = 12^+, 14^+$  states even in  $N = 94$  deformed nuclei. The presence of the  $g$  bosons lowers the energies of the yrast band states, and makes them closer in value to the experimentally observed energies. This shows the necessity of including the hexadecapole correlations in the description of the low-lying excitation energy spectra of rare-earth nuclei.

Another aspect of the yrast band that can be examined is the  $R_{4/2} = \frac{E_x(4^+)}{E_x(2^+)}$  ratio between the energies of the  $4^+$  and  $2^+$  states in near-spherical nuclei. The ratios are shown in Table 3.1. In  $N = 84$  nuclei, the *sdg*-IBM predicts the  $R_{4/2}$  to be less than 2, which is in agreement with the experiment. The *sd*-IBM, on the other hand, cannot predict such values, which means that such effects can be considered to be the products of hexadecapole collectivity. The values predicted by the *sd*-IBM are all above 2.10. A significantly low  $R_{4/2} = 1.54$  ratio is predicted by the *sdg*-IBM in  $^{152}\text{Er}$ , compared to the experimental value  $R_{4/2} = 1.83$ . This is because the *sdg*-IBM predicts a  $4_1^+$  state in  $^{152}\text{Er}$  to be somewhat lower in energy from the measured value. This could potentially be improved by considering the values of  $\sigma$  parameter to be larger than 1.0, however, the IBM PES would not approximate the SCMF PES as well as it does for  $\sigma = 1.0$  parameter value. Also, even though the predicted ratio is somewhat lower from the experimental value,

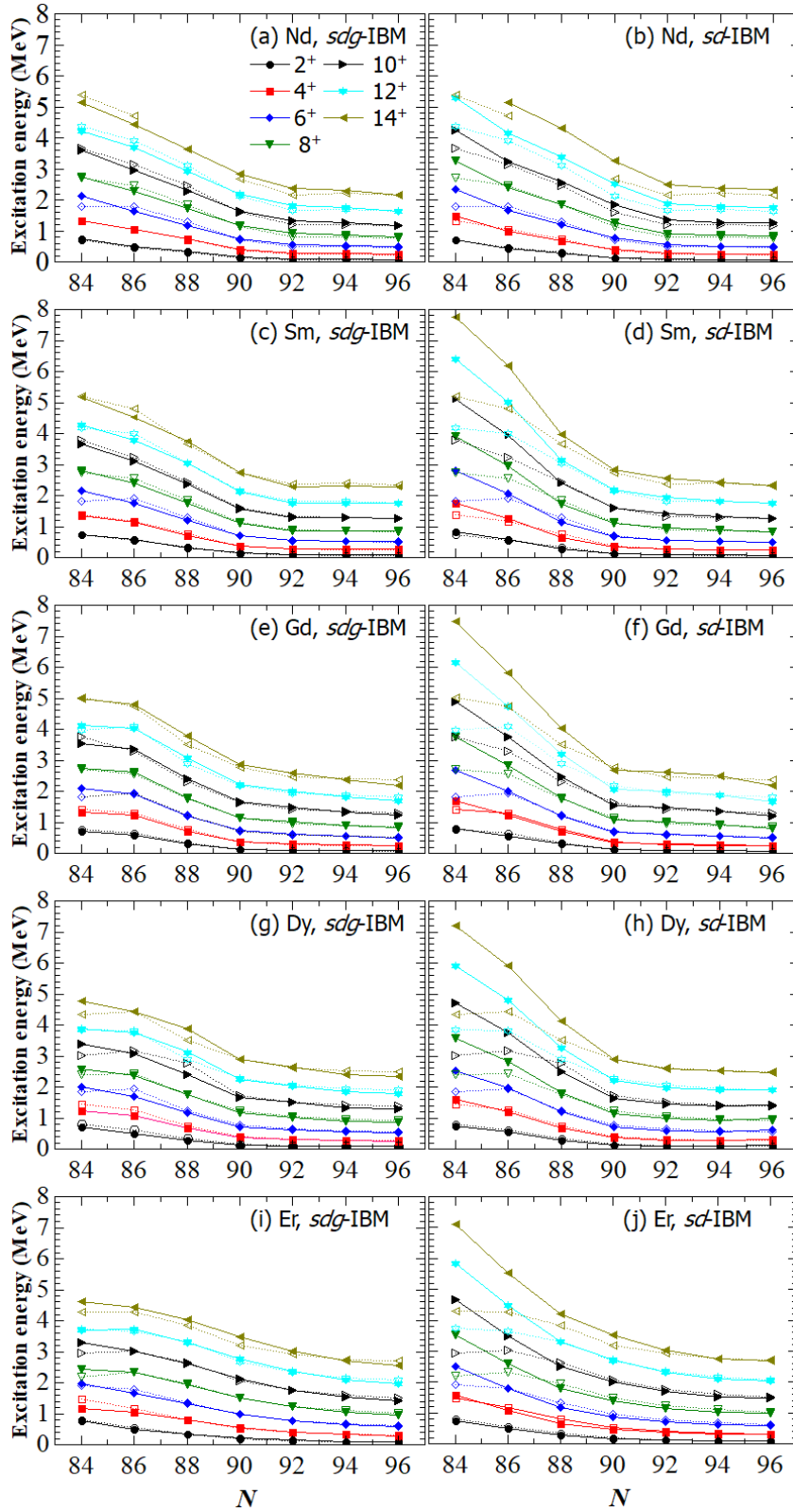


Figure 3.18: Calculated excitation energies of the yrast band states up to spin  $J^\pi = 14^+$  as functions of the neutron number  $N$  within the mapped *sdg*-IBM (left column) and *sd*-IBM (right column), represented by solid symbols connected by solid lines. Experimental data are taken from Ref. [50], and are depicted as open symbols connected by dotted lines. The figure is taken from Ref. [76].

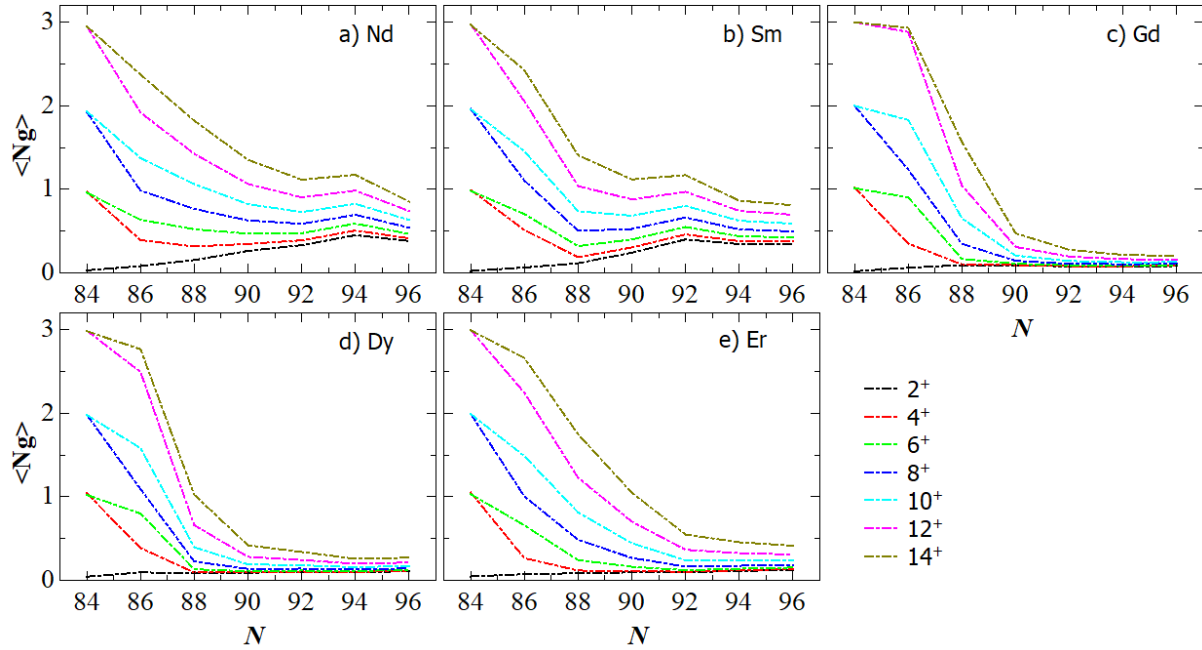


Figure 3.19: The expectation value of the  $g$  boson number operator  $\hat{n}_g$  in yrast band states up to  $J^\pi = 14^+$ , plotted as a function of the neutron number  $N$ .

it nevertheless represents an improvement over the simpler  $sd$ -IBM, which predicts the  $R_{4/2}$  value in  $^{152}\text{Er}$  to be 2.14. In  $N = 86$  all the measured ratios are larger than 2, however, most of them are below 2.10 in value. The  $sdg$ -IBM does significantly improve the calculated ratio  $^{146}\text{Nd}$ , and only slightly improves the calculated ratios in  $^{150}\text{Gd}$ ,  $^{152}\text{Dy}$  and  $^{154}\text{Er}$ . In the  $^{148}\text{Sm}$  isotope, the  $sdg$ -IBM predicts the ratio to be lower than 2 in value,  $R_{4/2} = 1.98$ , which is not in agreement with the experiment, since the experimental value  $R_{4/2} = 2.14$  is significantly larger than all other ratios in  $N = 86$  nuclei. The lowering of the calculated ratios is associated with the presence of the  $g$  boson in  $4_1^+$  states, which lowers the energy of those states to be closer to  $2_1^+$  states. From Figure 3.19, it can be seen that in the  $N = 84$  nuclei, the  $4_1^+$  states are predicted to contain one  $g$  boson in their configurations. In  $N = 86$  nuclei, the expectation value of  $\hat{n}_g$  in those states is below 1.0, so the  $R_{4/2}$  ratios are above 2 in value.

The lowering of energies in the yrast band as a consequence of the  $g$  boson presence in near-spherical nuclei deserves a comment. While the IBM is a collective model, and while single-particle modes are expected to play a role in describing the low-lying spectra of near-spherical nuclei, the fact that the  $sdg$ -IBM significantly improves the description of the yrast band in those nuclei, indicates that the inclusion of the  $g$  boson can also account for single-particle modes in the yrast band. It should also be noted that the IBM has been successfully

Table 3.1: Energy ratios  $R_{4/2} = E_x(4_1^+)/E_x(2_1^+)$  for  $N=84$  and  $86$  isotones calculated with the mapped  $sd$ - and  $sdg$ -IBM, and compared to the experimental values [50]. The table is taken from Ref. [76].

Nucleus	$sd$ -IBM	$sdg$ -IBM	Experiment
$^{144}\text{Nd}$	2.11	1.78	1.89
$^{146}\text{Nd}$	2.25	2.05	2.02
$^{146}\text{Sm}$	2.12	1.83	1.85
$^{148}\text{Sm}$	2.20	1.98	2.14
$^{148}\text{Gd}$	2.13	1.86	1.81
$^{150}\text{Gd}$	2.18	2.15	2.02
$^{150}\text{Dy}$	2.15	1.71	1.81
$^{152}\text{Dy}$	2.21	2.16	2.05
$^{152}\text{Er}$	2.14	1.54	1.83
$^{154}\text{Er}$	2.24	2.17	2.07

applied to many near-spherical nuclei and has been shown to be able to accurately describe various properties of the low-lying excitation energy spectra. Also, other theoretical studies, based on different microscopic models, have indicated that the  $2_1^+$  and  $4_1^+$  states in some near-spherical nuclei, e.g.  $^{144}\text{Nd}$  and  $^{146}\text{Sm}$ , are collective in nature [80].

### $0^+$ and $\gamma$ -vibrational band

Figure 3.20 shows the calculated energies of the  $0_2^+$ ,  $2_3^+$  and  $4_3^+$  states, associated with the  $K^\pi = 0^+$  band in deformed nuclei. It should be noted that the  $0_2^+$  level in  $^{160}\text{Dy}$  is taken to be the  $0^+$  level at 1.28 MeV energy. However, there is also a possibility of the existence of two lower  $0^+$  levels at 0.681 MeV and 0.703 MeV energies in this isotope [50]. Since the parity and spin of those levels are not fully established, the  $0^+$  state at 1.28 MeV is taken to be the bandhead of the  $K^\pi = 0^+$  band. The calculated  $0_2^+$  states are not improved by the  $sdg$ -IBM compared to the  $sd$ -IBM. This is not unusual, since the expectation value of the  $g$  boson number operator in those states is  $\langle \hat{n}_g \rangle \approx 0$ . On the other hand, a  $g$  boson is predicted to be present in the  $2_3^+$  and  $4_3^+$  states in  $N \leq 88$  nuclei. As a result, the energies of these states are significantly lowered compared to the  $sd$ -IBM results, and are closer to the experimental values. However, the predicted  $2_3^+$  and  $4_3^+$  energies are almost identical in energy, which is not in agreement with the experiment. In the  $N \geq 90$  deformed region, there are no significant differences between the energies of the aforementioned states calculated by the  $sdg$ - and  $sd$ -IBM. Overall, it can be said that the  $sdg$ -IBM provides an improvement of the  $2_3^+$  and  $4_3^+$  energies in  $N \leq 88$  nuclei, however, the band structure is not reproduced by the  $sdg$ -IBM. There are, on the other hand, no significant differences between the energies of the  $0_2^+$  states calculated by the  $sdg$ - and  $sd$ -IBM.

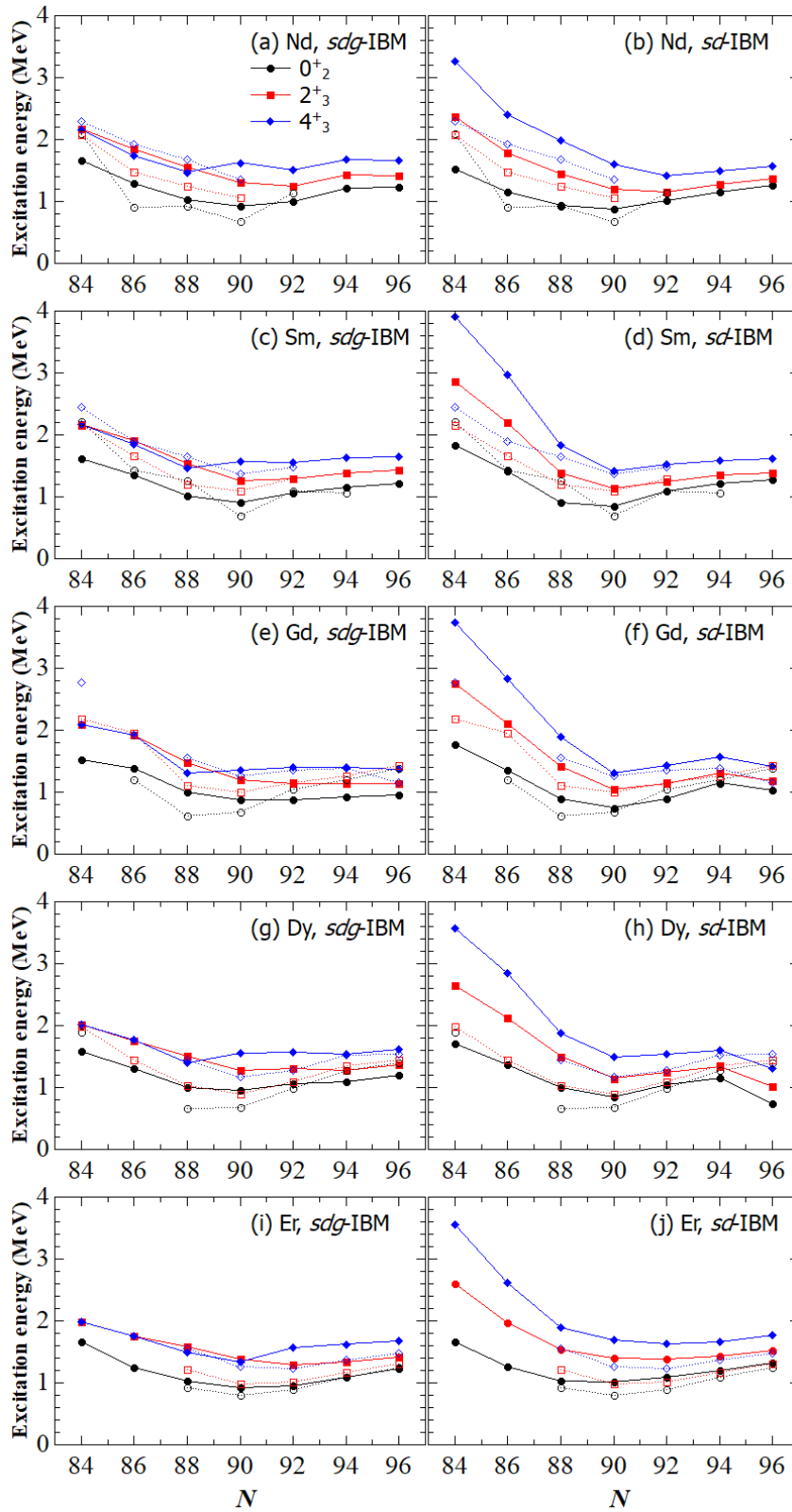


Figure 3.20: Same caption as Figure 3.18, but for the  $0_2^+$ ,  $2_3^+$  and  $4_3^+$  states.

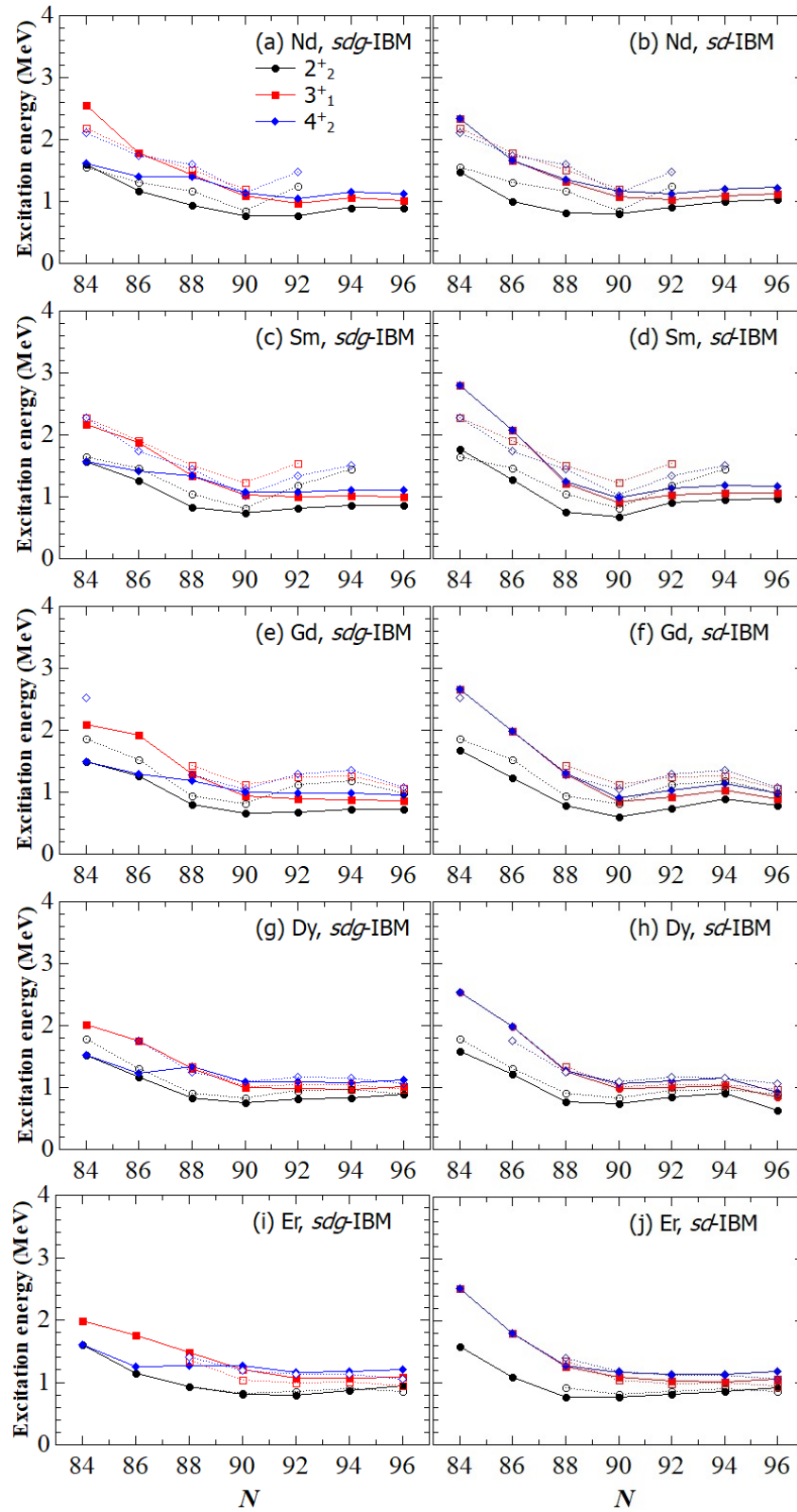
Figure 3.21: Same caption as Figure 3.18, but for the  $2^+_{2}$ ,  $3^+_{1}$  and  $4^+_{2}$  states.

Figure 3.21 shows the calculated excitation energies of the  $2_2^+$ ,  $3_1^+$  and  $4_2^+$  states, associated with the  $\gamma$ -vibrational band in deformed nuclei. The *sdg*-IBM does provide some slight improvements in the description of  $2_2^+$  and  $3_1^+$  energy states in  $N \leq 88$  Nd and Sm isotopes. On the other hand, the  $4_2^+$  state is significantly lower in energy compared to the *sd*-IBM results. In fact, in  $N \leq 86$  nuclei, the  $4_2^+$  state is predicted by the *sdg*-IBM to be so low in energy as to be near the  $2_2^+$  state. In the  $N \geq 88$  nuclei, there are no significant differences between the energies calculated by the *sdg*- and *sd*-IBM, and the results in those nuclei are in a good agreement with the experiment. The fact that the  $4_2^+$  state is predicted to be low in energy shows that the chosen Hamiltonian may not be suitable for description of such states in near shell-closure nuclei. The problem could potentially be solved by including more terms and independent parameters in the Hamiltonian, however, such extensions of the *sdg*-IBM Hamiltonian would make the calculations significantly more involved. Also, since the parameters of the Hamiltonian were fitted to a PES obtained from the SCMF calculation with a specific EDF and a specific choice of the pairing interaction, which are not tailored for a particular nucleus, a different choice of the EDF and the pairing interaction could lead to different results in certain bands. These two problems are left for a separate study.

A comment deserves to be made on differences between the *sdg*- and *sd*-IBM energy results in the  $N \geq 90$  deformed region. The states of the ground state band, the  $0^+$  band and the  $\gamma$ -vibrational band are almost equally well described by both models, with some exceptions being the  $12^+$  and  $14^+$  yrast band states in some deformed Nd and Sm isotopes. This is expected, since the *sd*-IBM has been shown to be adequate in describing the low-lying spectra of deformed nuclei. The differences between the two models in this region are visible only in higher-lying states, e.g.  $2_n^+$  ( $n \geq 6$ ) and  $3_n^+$  ( $n \geq 3$ ) states. The problem is that the experimental data on those states is very limited. The *g* boson is predicted to be present in these states, and, as a consequence, the energies of those states are lower and in a better agreement with the experiment compared to the same states calculated with the *sd*-IBM. The differences between the two models in this region can also be observed in the calculated  $B(E2)$  and  $B(E4)$  transition strengths, which will be discussed in the following section.

## 3.3 Transition strengths

### 3.3.1 Effective charges

The quadrupole effective charges  $e_2^{sd,sdg}$  of Eq. (2.65) were fitted in order to reproduce the  $B(E2; 2_1^+ \rightarrow 0^+)$  transition strengths from the first  $2^+$  state to the  $0^+$  ground state. The hex-



adecapole effective charges  $e_4^{sd,sdg}$  of Eqs. (2.66, 2.67), respectively, were fitted in order to reproduce the  $B(E4; 4_1^+ \rightarrow 0^+)$  transition strength from the first  $4^+$  state to the ground state. For isotopes with no available experimental data on such transitions, the hexadecapole effective charges were fitted so that the transition strengths are lower in values in near shell-closure nuclei, peak in value around  $N = 92$  nuclei, and then decrease again. On the other hand, following Ref. [66], the monopole transition operator parameters  $e_n, e_p, \eta$  and  $\gamma$  of Eqs. (2.68, 2.69), were fixed for all isotopes. The chosen values are  $e_n = 0.50e, e_p = e, \eta = \gamma = 0.75 \text{ fm}^2$ . While the effective neutron and proton charge values are the same as in Ref. [66], the  $\eta$  and  $\gamma$  values were increased to better reproduce the available experimental data on monopole strengths [50, 81]. This is not surprising, since the Hamiltonian used in this work is different from the one used in Ref. [66].

The values of the quadrupole and hexadecapole effective charges  $e_2^{sd,sdg}, e_4^{sd,sdg}$  are shown in Figure 3.22. The reason for plotting them as a function of the valence boson number  $N_B$  instead of the neutron number  $N$  is to prevent the overlapping between the effective charge values of different nuclei with the same  $N$  in the graph. The quadrupole effective charges of the  $sdg$ - and  $sd$ -IBM do not differ significantly in value. This can be explained by the fact that these charges were fitted in order to reproduce the transition strength from the first  $2^+$  state, which does not have a presence of the  $g$  boson, as can be seen from Fig. 3.19. The hexadecapole effective charges, on the other hand, differ significantly in value between the  $sdg$ - and  $sd$ -IBM. While in the deformed region, the  $e_4^{sd}$  charges are somewhat larger in value than  $e_4^{sdg}$ , in near-spherical nuclei, the  $e_4^{sd}$  charges must be set to extremely high values in order for the  $sd$ -IBM to reproduce the same  $B(E4)$  transition strength as the  $sdg$ -IBM. These extremely high  $e_4^{sd}$  values point to the necessity of including the  $g$  boson in the calculations of  $B(E4)$  transition strengths.

### 3.3.2 Quadrupole transitions

Figure 3.23 shows the  $B(E2; J \rightarrow J - 2)$  transition strengths between the ground state band states in well deformed  $N = 90, 92$  nuclei. The reason for choosing these nuclei lies in the fact that most of the available experimental data on  $E2$  transitions in the ground state band can be found in these nuclei, which makes them the ideal candidates for comparing the calculated  $B(E2)$  transition strengths between  $sdg$ - and  $sd$ -IBM. One can notice a significant difference in the  $B(E2)$  transition strengths, predicted by the  $sdg$ -IBM, between lighter isotopes of  $^{150,152}\text{Nd}$  and  $^{152,154}\text{Sm}$ , and heavier isotopes. In Nd and Sm nuclei, the predicted transition strengths between  $J^\pi \geq 6^+$  states are significantly larger in the  $sdg$ -IBM compared to the  $sd$ -IBM, which is not the case in the isotopes of Gd, Dy and Er. This can be attributed to the fact that the  $(d^\dagger \times \tilde{g} + g^\dagger \times \tilde{d})^{(2)}$  term in the  $\hat{Q}^{(2)}$  operator of Eq. (2.62), contributes more to the  $B(E2)$  transition

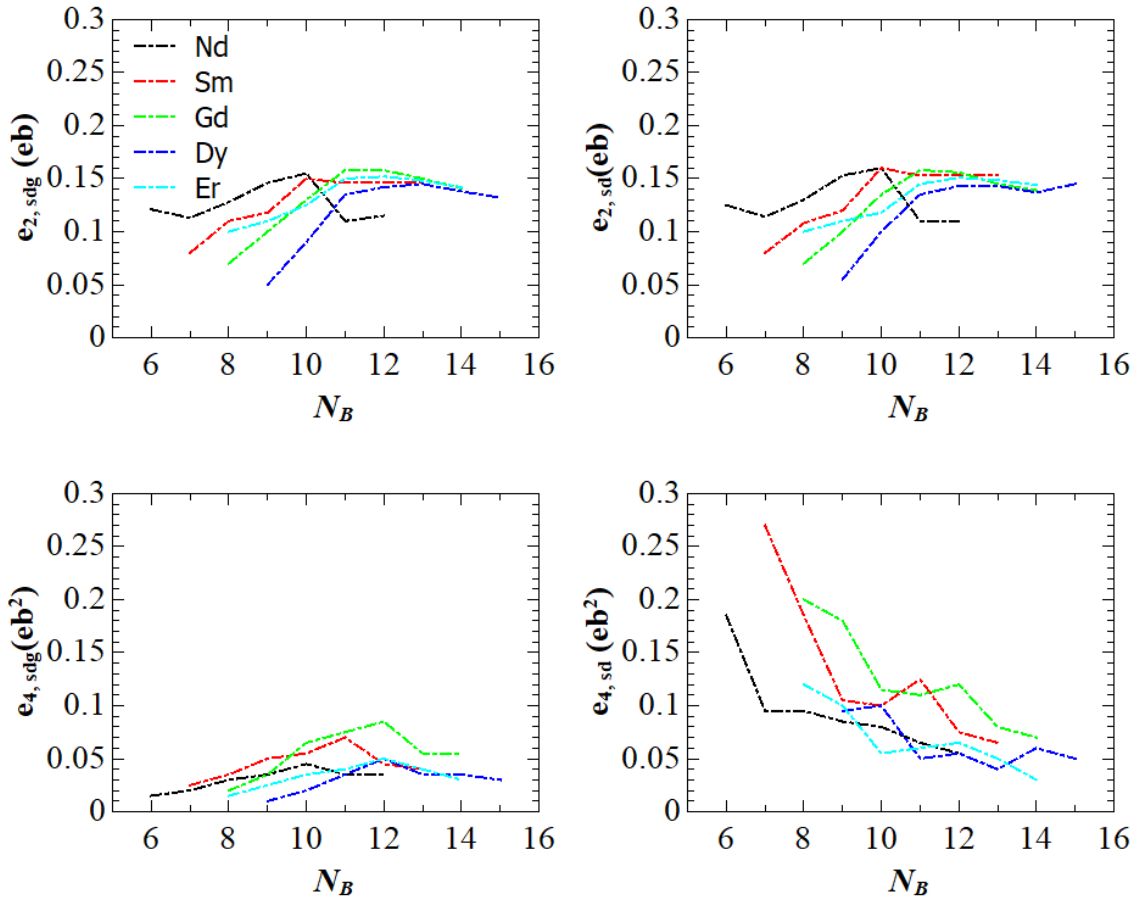


Figure 3.22: First row: The values of the quadrupole effective charges  $e_2^{sdg}$  (left) and  $e_2^{sd}$  (right). Second row: The values of the hexadecapole effective charges  $e_4^{sdg}$  (left) and  $e_4^{sd}$  (right). All effective charges are plotted as a function of the valence boson number  $N_B$

strengths in the Nd and Sm isotopes, due to the  $\sigma$  parameter being larger than 1.0 in those nuclei. The obtained  $B(E2)$  transitions in Sm resemble the results of the axial rotor calculations from Refs. [39, 40]. The  $sdg$ -IBM mostly improves the description of transition between the yrast  $J^\pi \geq 6^+$  states, which is in agreement with the previously performed phenomenological calculations [39, 40].

In the heavier isotopes of Gd, Dy and Er, the differences between the  $sdg$ - and  $sd$ -IBM calculated transitions are significantly smaller, which can be attributed to the  $\sigma = 1.0$  parameter values in those nuclei. The transitions in  $N = 90$  nuclei are underestimated by both models, with the  $sdg$ -IBM providing only a small improvement to the results, while in the  $N = 92$  nuclei, both models predict the values of transition strengths to be in good agreement with the experiment.

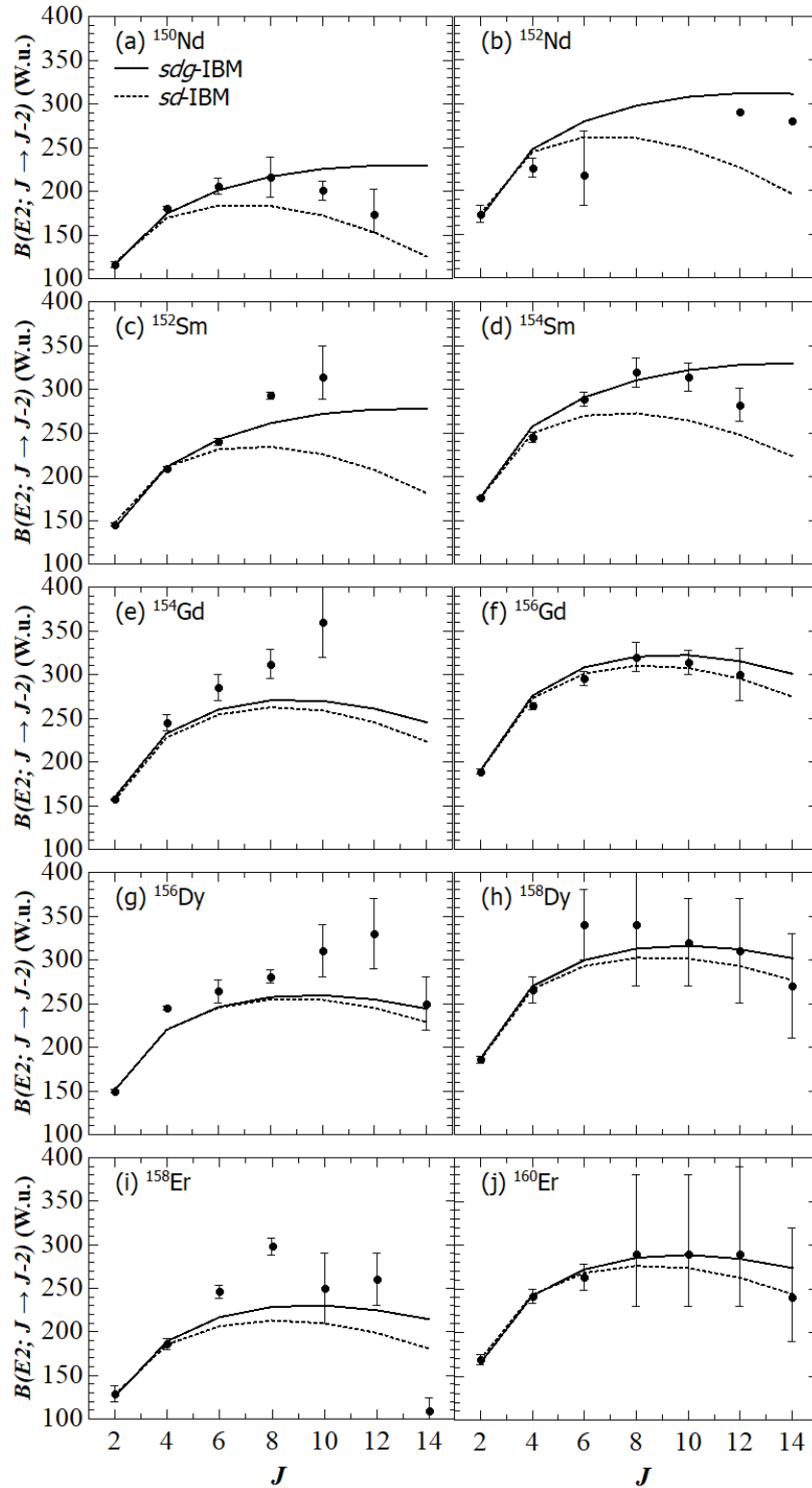


Figure 3.23:  $B(E2)$  transition strengths in the ground state band of the well-deformed  $N = 90$  (left) and  $N = 92$  (right) isotopes as functions of spin  $J$ , calculated with the mapped  $sdg$ -IBM (solid curves) and  $sd$ -IBM (dotted curves). The experimental data, represented by solid circles, are adopted from Ref. [50]. The figure is taken from Ref. [76].

Due to the margins of error of the measured transition strengths being very large, it is not possible to determine whether the *sdg*-IBM provides some improvements in the description of quadrupole transition strengths in those nuclei.

### 3.3.3 Hexadecapole transitions

Figure 3.24 shows the calculated  $B(E4; 4_n^+ \rightarrow 0^+)$  ( $n = 1, 2, 3, 4$ ) transition strengths from the  $4_n^+$  states to the  $0^+$  ground states. The transition strengths are plotted as a function of the nucleon number  $A$ , to avoid the overlapping of the calculated values between different nuclei with the same neutron number  $N$ . Since the  $e_4^{sd, sdg}$  effective charges were fitted to reproduce the  $B(E4; 4_1^+ \rightarrow 0^+)$  transition strengths, the more interesting  $E4$  transitions to examine are those from the  $4_{n \geq 2}^+$  states to the ground state. The *sdg*-IBM predicts several large  $B(E4)$  transition strengths from those states to the ground state in deformed isotopes, which corresponds to the *sdg*-IBM predicting the existence of the  $K^\pi = 4^+$  hexadecapole band in deformed rare-earth nuclei. On the other hand, these large  $B(E4)$  values are not predicted by the *sd*-IBM, which points to the necessity of including the  $g$  boson in describing the  $E4$  transitions. The experimental data on such transitions is only available in  $^{146}\text{Nd}$  isotope. The measured  $B(E4)$  transition strengths in this isotope are low in value, and the *sdg*-IBM does provide a slight improvement over the *sd*-IBM in the description of the  $B(E4; 4_2^+ \rightarrow 0^+)$  strength, while both models underestimate the  $B(E4; 4_4^+ \rightarrow 0^+)$  strength. The large  $B(E4)$  values from higher  $4^+$  states have been observed in nuclei such as  $^{194, 196, 198}\text{Pt}$  [40, 50], however, these nuclei are predicted to have a significant presence of quadrupole triaxial correlations [49], which would have to be separately included, so the study of those nuclei in the framework of the mapped *sdg*-IBM is left for a future study.

### 3.3.4 Monopole transitions

Figure 3.25 shows the squared values of monopole strengths  $\rho^2(E0; 0_i^+ \rightarrow 0_j^+)$  with  $i = 2, 3$  and  $j = 1, 2$  for Sm and Gd isotopes. These results are shown only for Sm and Gd because the experimental data on monopole strengths can only be found for these isotopes [50, 81]. As can be seen from the figure, the *sdg*-IBM does not significantly improve the description of the monopole strengths compared to the *sd*-IBM. Both models seem to overestimate the values of the  $\rho^2(E0; 0_2^+ \rightarrow 0_1^+)$  strength in  $^{150, 152}\text{Sm}$ , and both models predict that the strengths of the  $0_3^+ \rightarrow 0_1^+$  transitions become larger than the strengths of  $0_3^+ \rightarrow 0_2^+$  transitions in the deformed region, which contradicts the available experimental data in  $^{152}\text{Sm}$  and  $^{156}\text{Gd}$ . The *sdg*-IBM slightly improves the description of the  $0_3^+ \rightarrow 0_2^+$  transition in  $^{152}\text{Sm}$  and the  $0_3^+ \rightarrow 0_1^+$  transi-

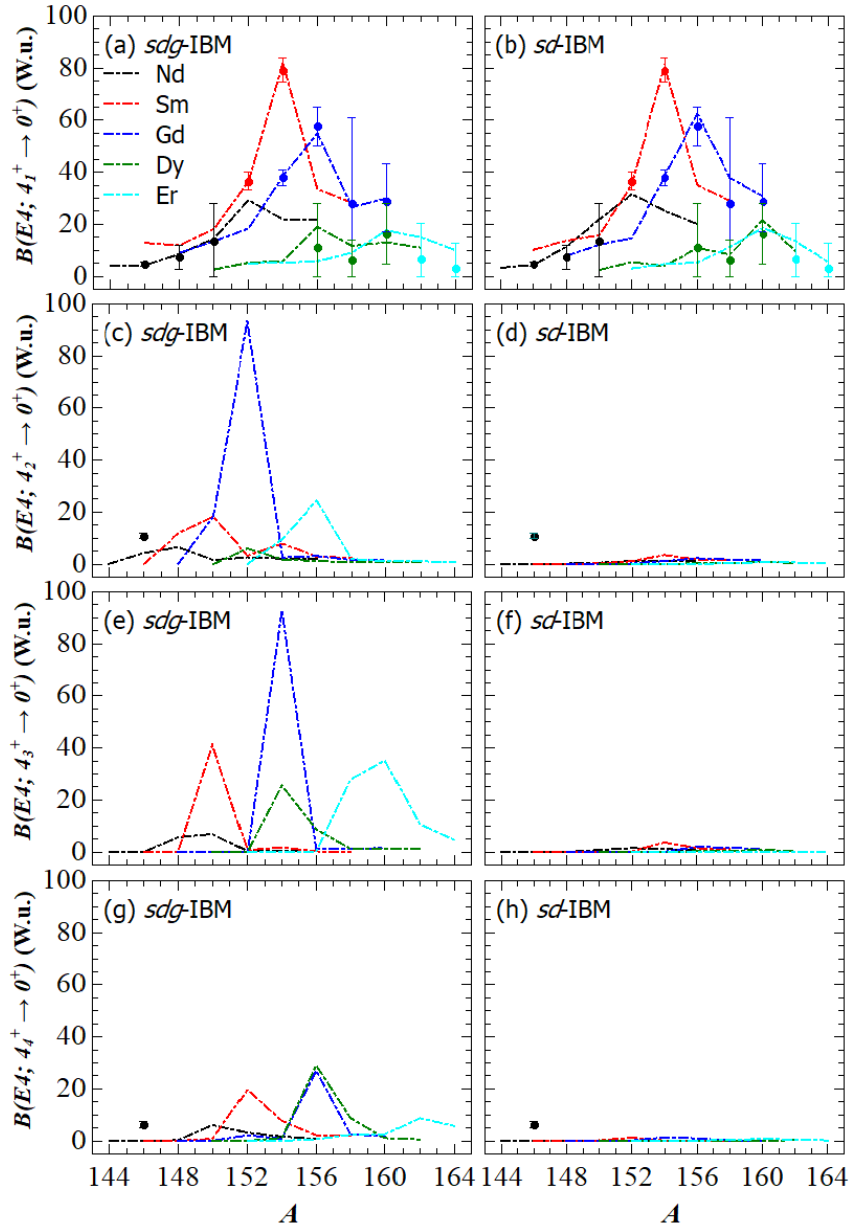


Figure 3.24:  $B(E4)$  transition strengths in W.u. for transitions between the first (panels (a) and (b)), second (panels (c) and (d)), third (panels (e) and (f)) and the fourth (panels (g) and (h))  $4^+$  states and the  $0^+$  ground state, plotted as functions of the nucleon number  $A$ . The *sdg*-IBM results are shown in the left column, while the *sd*-IBM results are shown in the right column. The experimental data, represented by solid circles, are adopted from Refs. [14–16, 50]. The figure is taken from Ref. [76].

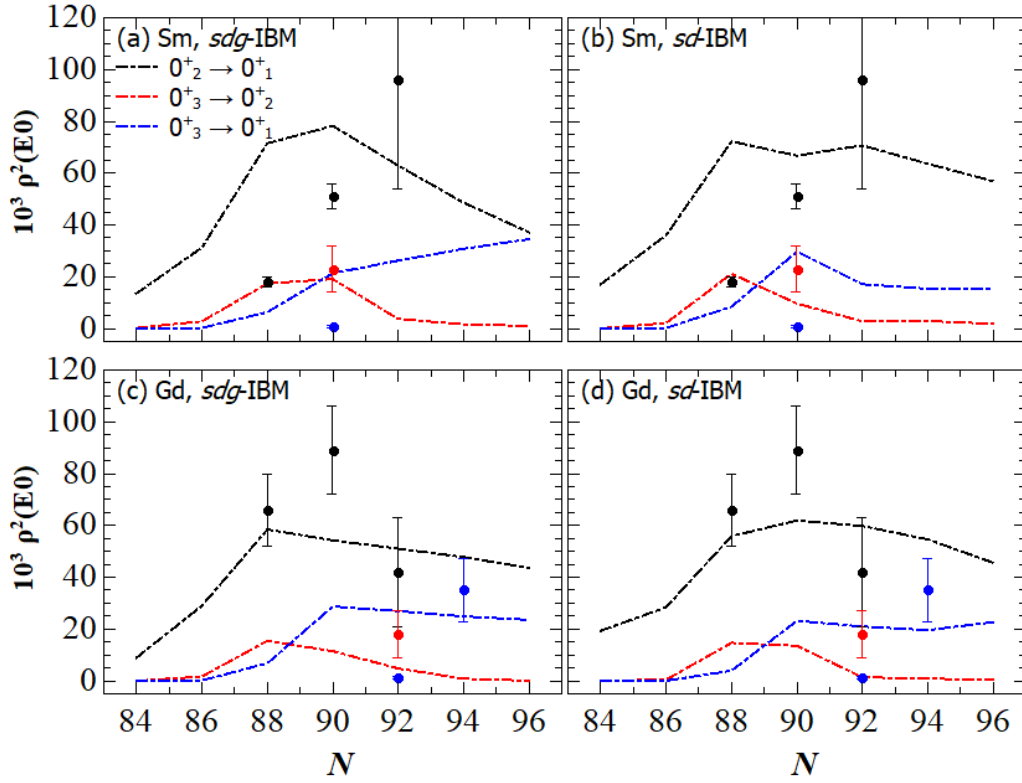


Figure 3.25: Squared values of the monopole strengths  $\rho^2(E0; 0_i^+ \rightarrow 0_j^+)$  in Sm and Gd isotopes, plotted as functions of the neutron number  $N$ . The experimental data, represented by solid circles, are taken from Refs. [50, 81]. The figure is taken from Ref. [76].

tion in  $^{158}\text{Gd}$ . Overall, it cannot be said that the *sdg*-IBM provides an improved description of monopole transition strengths. This is not surprising, since the  $0_n^+$  states up to  $n = 3$  are not predicted to contain a *g* boson in their configuration. For example, the first  $0^+$  state in  $^{154}\text{Sm}$ , that is predicted to be of one *g* boson content, is the  $0_5^+$  state, and there are no available experimental data on monopole transitions between  $0_{n \geq 4}^+$  states.

# Chapter 4

## Thesis summary and outlook

### 4.1 Summary of this Thesis

This thesis represents a first attempt to systematically study the effects of axial quadrupole and hexadecapole correlations in the framework of a microscopic model. It is shown that the  $g$  boson can be included in the IBM microscopically, by applying the mapping method to the  $sdg$ -IBM Hamiltonian and fitting the Hamiltonian parameters to the PES calculated in the framework of the RMF model with the DD-PC1 functional, with constraints set on the axial quadrupole and hexadecapole deformation parameters. The obtained model was applied to even-even isotopes of Nd, Sm, Gd, Dy and Er in the neutron number range  $N = 84 - 96$  and was shown to provide some significant improvements over the simpler  $sd$ -IBM. Firstly, the description of the  $J^\pi \geq 6^+$  states of the ground state band in  $N \leq 88$  nuclei is significantly improved by the mapped  $sdg$ -IBM. It was shown that this model can account for the ratio  $R_{4/2}$  between energies of the yrast states  $4^+$  and  $2^+$  being less than 2 in value in  $N = 84$  nuclei. The description of  $E2$  transitions between higher-lying yrast band states in deformed  $N = 90, 92$  nuclei is also improved by the aforementioned model. Finally, the mapped  $sdg$ -IBM is able to predict the existence of the  $K^\pi = 4^+$  bands in deformed nuclei with enhanced  $B(E4)$  transition strengths to the  $0^+$  ground state. These predicted transition strengths could be of interest to experimentalist who are doing research on nuclear structure. Other properties of the low-lying spectra, e.g. the  $0^+$  and the  $\gamma$ -vibrational band, as well as the monopole transitions between  $0^+$  states, are not significantly improved by the mapped  $sdg$ -IBM, and can be accounted for by the simpler  $sd$ -IBM. This is not surprising, since quadrupole correlations are expected to be dominant in describing most of the properties of the low-lying excitation energy spectra. Nevertheless, this work shows that the inclusion of hexadecapole correlations is necessary in describing various properties of the nucleus, and should represent an integral part in any theoretical study which aims to achieve a

precise description of the excitation energy spectra in rare-earth nuclei.

## 4.2 Outlook

This work could potentially be expanded in the future to study the spectra and transitions of odd- $A$  and odd-odd rare-earth nuclei. This could also lead to a systematic study of the effects of hexadecapole correlations on  $\beta$ -decays in rare-earth nuclei. A systematic study of the sensitivity of the results on the choice of the EDF and the pairing interactions could also be useful and bring us to a better understanding of hexadecapole correlations in nuclei. The model could be further expanded to include triaxial quadrupole deformations along with axial quadrupole and hexadecapole deformations. That model could then be applied to various other nuclei, such as Pt, Os, and actinides. Finally, this model could be expanded to the *sdg*-IBM-2 model, in which proton and neutron bosons are separately considered, and be used to study phenomena beyond the reach of the IBM-1, such as scissor modes.



# Bibliography

1. Mayer, M. G. On Closed Shells in Nuclei. II. *Phys. Rev.* **75**, 1969–1970. <https://link.aps.org/doi/10.1103/PhysRev.75.1969> (12 June 1949).
2. Haxel, O., Jensen, J. H. D. & Suess, H. E. On the "Magic Numbers" in Nuclear Structure. *Phys. Rev.* **75**, 1766–1766. <https://link.aps.org/doi/10.1103/PhysRev.75.1766.2> (11 June 1949).
3. Bohr, A. & Mottelson, B. R. *Nuclear Structure* (Benjamin, New York, USA, 1975).
4. Ring, P. & Schuck, P. *The Nuclear Many-Body Problem* (Springer-Verlag, Berlin, 1980).
5. Gaffney, L., Butler, P. A., Scheck, M., *et al.* Studies of pear-shaped nuclei using accelerated radioactive beams. *Nature* **497**, 199–204 (2013).
6. Taniuchi, R., Santamaria, C., Doornenbal, P., *et al.*  $^{78}\text{Ni}$  revealed as a doubly magic stronghold against nuclear deformation. *Nature* **569**, 53–58 (2019).
7. Doornenbal, P. *et al.* In-Beam  $\gamma$ -Ray Spectroscopy of  $^{34,36,38}\text{Mg}$ : Merging the  $N=20$  and  $N=28$  Shell Quenching. *Phys. Rev. Lett.* **111**, 212502. <https://link.aps.org/doi/10.1103/PhysRevLett.111.212502> (21 Nov. 2013).
8. Holl, M. *et al.* Proton inelastic scattering reveals deformation in  $^8\text{He}$ . *Physics Letters B* **822**, 136710. ISSN: 0370-2693. <https://www.sciencedirect.com/science/article/pii/S037026932100650X> (2021).
9. Heyde, K. *Basic Ideas and Concepts in Nuclear Physics: An Introductory Approach, Third Edition* (IOP Publishing, Bristol, UK, 2004).
10. Gupta, Y. *et al.* Determination of hexadecapole (4) deformation of the light-mass nucleus  $^{24}\text{Mg}$  using quasi-elastic scattering measurements. *Physics Letters B* **806**, 135473. ISSN: 0370-2693. <https://www.sciencedirect.com/science/article/pii/S037026932030277X> (2020).

11. Gupta, Y. *et al.* Precise determination of quadrupole and hexadecapole deformation parameters of the sd-shell nucleus,  $^{28}\text{Si}$ . *Physics Letters B* **845**, 138120. ISSN: 0370-2693. <https://www.sciencedirect.com/science/article/pii/S0370269323004549> (2023).
12. Hendrie, D. *et al.* Determination of Y40 and Y60 components in the shapes of rare earth nuclei. *Physics Letters B* **26**, 127–130. ISSN: 0370-2693. <https://www.sciencedirect.com/science/article/pii/0370269368905029> (1968).
13. Erb, K. A., Holden, J. E., Lee, I. Y., Saladin, J. X. & Saylor, T. K. Quadrupole and Hexadecapole Deformations in Rare-Earth Nuclei. *Phys. Rev. Lett.* **29**, 1010–1014. <https://link.aps.org/doi/10.1103/PhysRevLett.29.1010> (15 Oct. 1972).
14. Wollersheim, H. & W. Elze, T. Electric quadrupole and hexadecapole moments in the transitional nuclei  $^{150}\text{Nd}$ ,  $^{152}\text{Sm}$ ,  $^{154}\text{Sm}$ ,  $^{154}\text{Gd}$  and  $^{156}\text{Gd}$ . *Nuclear Physics A* **278**, 87–94. ISSN: 0375-9474. <https://www.sciencedirect.com/science/article/pii/0375947477901865> (1977).
15. Ronningen, R. M. *et al.*  $E2$  and  $E4$  reduced matrix elements of  $^{154,156,158,160}\text{Gd}$  and  $^{176,178,180}\text{Hf}$ . *Phys. Rev. C* **16**, 2208–2217. <https://link.aps.org/doi/10.1103/PhysRevC.16.2208> (6 Dec. 1977).
16. Ronningen, R. M. *et al.* Coulomb excitation measurements of reduced  $E2$  and  $E4$  transition matrix elements in  $^{156,158}\text{Dy}$ ,  $^{162,164}\text{Er}$ , and  $^{168}\text{Yb}$ . *Phys. Rev. C* **16**, 2218–2222. <https://link.aps.org/doi/10.1103/PhysRevC.16.2218> (6 Dec. 1977).
17. Bemis, C. E. *et al.*  $E2$  and  $E4$  Transition Moments and Equilibrium Deformations in the Actinide Nuclei. *Phys. Rev. C* **8**, 1466–1480. <https://link.aps.org/doi/10.1103/PhysRevC.8.1466> (4 Oct. 1973).
18. Zamfir, N., Hering, G., Casten, R. & Paul, P. Hexadecapole deformations in actinide and trans-actinide nuclei. *Physics Letters B* **357**, 515–520. ISSN: 0370-2693. <https://www.sciencedirect.com/science/article/pii/037026939500978T> (1995).
19. Ryssens, W., Giacalone, G., Schenke, B. & Shen, C. Evidence of Hexadecapole Deformation in Uranium-238 at the Relativistic Heavy Ion Collider. *Phys. Rev. Lett.* **130**, 212302. <https://link.aps.org/doi/10.1103/PhysRevLett.130.212302> (21 May 2023).
20. Chi, J., Qiang, Y., Gao, C. & Pei, J. Role of hexadecapole deformation in fission potential energy surfaces of  $^{240}\text{Pu}$ . *Nuclear Physics A* **1032**, 122626. ISSN: 0375-9474. <https://www.sciencedirect.com/science/article/pii/S0375947423000295> (2023).

21. Engel, J. & Menéndez, J. Status and future of nuclear matrix elements for neutrinoless double-beta decay: a review. *Rep. Prog. Phys.* **80**, 046301. <https://doi.org/10.1088%2F1361-6633%2Faa5bc5> (Mar. 2017).
22. Bertulani, C. A. *Nuclear Physics in a Nutshell* STU - Student edition. ISBN: 9780691125053. <http://www.jstor.org/stable/j.ctt7shsk> (2024) (Princeton University Press, 2007).
23. Bender, M., Heenen, P.-H. & Reinhard, P.-G. Self-consistent mean-field models for nuclear structure. *Rev. Mod. Phys.* **75**, 121–180. <https://link.aps.org/doi/10.1103/RevModPhys.75.121> (1 Jan. 2003).
24. Nikšić, T., Vretenar, D. & Ring, P. Relativistic nuclear energy density functionals: Mean-field and beyond. *Progress in Particle and Nuclear Physics* **66**, 519–548. ISSN: 0146-6410. <https://www.sciencedirect.com/science/article/pii/S0146641011000561> (2011).
25. Vretenar, D. & Nikšić, T. *Nuclear Structure Models Based on Relativistic Energy Density Functionals* in *Basic Concepts in Nuclear Physics: Theory, Experiments and Applications* (eds García-Ramos, J.-E., Alonso, C. E., Andrés, M. V. & Pérez-Bernal, F.) (Springer International Publishing, Cham, 2016), 113–165. ISBN: 978-3-319-21191-6.
26. Vretenar, D., Afanasjev, A., Lalazissis, G. & Ring, P. Relativistic Hartree–Bogoliubov theory: static and dynamic aspects of exotic nuclear structure. *Physics Reports* **409**, 101–259. ISSN: 0370-1573. <https://www.sciencedirect.com/science/article/pii/S0370157304004545> (2005).
27. Wa Wong, C. Generator-coordinate methods in nuclear physics. *Physics Reports* **15**, 283–357. ISSN: 0370-1573. <https://www.sciencedirect.com/science/article/pii/S0370157375900368> (1975).
28. Delaroche, J.-P. *et al.* Structure of even-even nuclei using a mapped collective Hamiltonian and the D1S Gogny interaction. *Physical Review C* **81**, 014303. <https://api.semanticscholar.org/CorpusID:119255158> (2009).
29. Nikšić, T. *et al.* Beyond the relativistic mean-field approximation. III. Collective Hamiltonian in five dimensions. *Phys. Rev. C* **79**, 034303. <https://link.aps.org/doi/10.1103/PhysRevC.79.034303> (3 Mar. 2009).
30. Xia, S. Y. *et al.* Spectroscopy of reflection-asymmetric nuclei with relativistic energy density functionals. *Phys. Rev. C* **96**, 054303. <https://link.aps.org/doi/10.1103/PhysRevC.96.054303> (5 Nov. 2017).

31. Iachello, F. & Arima, A. *The interacting boson model* (Cambridge University Press, Cambridge, 1987).
32. Puddu, G., Scholten, O. & Otsuka, T. Collective quadrupole states of Xe, Ba and Ce in the interacting boson model. *Nuclear Physics A* **348**, 109–124. ISSN: 0375-9474. <https://www.sciencedirect.com/science/article/pii/0375947480905485> (1980).
33. Zhang, M. *et al.* Structure of the actinides by the interacting boson model. *Phys. Rev. C* **32**, 1076–1079. <https://link.aps.org/doi/10.1103/PhysRevC.32.1076> (3 Sept. 1985).
34. Rikovska, J. & Bonatsos, D. Structure of even-even actinides in the interacting boson model and the  $N = 152$  subshell closure. *Physics Letters B* **211**, 259–264. ISSN: 0370-2693. <https://www.sciencedirect.com/science/article/pii/0370269388908994> (1988).
35. Casten, R. F. & Warner, D. D. The interacting boson approximation. *Reviews of Modern Physics* **60**, 389–469. <https://api.semanticscholar.org/CorpusID:122909017> (1988).
36. Baker, F. T. E4 systematics and the interacting boson model. *Phys. Rev. C* **32**, 1430–1431. <https://link.aps.org/doi/10.1103/PhysRevC.32.1430> (4 Oct. 1985).
37. Otsuka, T. & Sugita, M. Proton-neutron sdg boson model and spherical-deformed phase transition. *Physics Letters B* **215**, 205–210. ISSN: 0370-2693. <https://www.sciencedirect.com/science/article/pii/0370269388914219> (1988).
38. Devi, Y. D. & Kota, V. K. B. Spectroscopy of samarium isotopes in the sdg interacting boson model. *Phys. Rev. C* **45**, 2238–2246. <https://link.aps.org/doi/10.1103/PhysRevC.45.2238> (5 May 1992).
39. Kuyucak, S. & Lac, V.-S. Comment on “Spectroscopy of samarium isotopes in the sdg interacting boson model”. *Phys. Rev. C* **47**, 1815–1818. <https://link.aps.org/doi/10.1103/PhysRevC.47.1815> (4 Apr. 1993).
40. Kuyucak, S. Hexadecapole degree of freedom in the interacting boson model. *Nucl. Phys. A* **570**, 187–194. ISSN: 0375-9474. <https://www.sciencedirect.com/science/article/pii/0375947494902828> (1994).
41. Nomura, K., Shimizu, N. & Otsuka, T. Mean-Field Derivation of the Interacting Boson Model Hamiltonian and Exotic Nuclei. *Phys. Rev. Lett.* **101**, 142501 (14 Sept. 2008).
42. Nomura, K., Shimizu, N. & Otsuka, T. Formulating the interacting boson model by mean-field methods. *Phys. Rev. C* **81**, 044307 (4 Apr. 2010).

43. Nomura, K., Otsuka, T., Shimizu, N. & Guo, L. Microscopic formulation of the interacting boson model for rotational nuclei. *Phys. Rev. C* **83**, 041302 (4 Apr. 2011).
44. Nomura, K., Shimizu, N., Vretenar, D., Nikšić, T. & Otsuka, T. Robust Regularity in  $\gamma$ -Soft Nuclei and Its Microscopic Realization. *Phys. Rev. Lett.* **108**, 132501 (13 Mar. 2012).
45. Nomura, K. *Interacting Boson Model from Energy Density Functionals* (Springer, Tokyo, 2013).
46. Nomura, K., Vretenar, D. & Lu, B.-N. Microscopic analysis of the octupole phase transition in Th isotopes. *Phys. Rev. C* **88**, 021303 (2 Aug. 2013).
47. Nomura, K., Vretenar, D., Nikšić, T. & Lu, B.-N. Microscopic description of octupole shape-phase transitions in light actinide and rare-earth nuclei. *Phys. Rev. C* **89**, 024312. <https://link.aps.org/doi/10.1103/PhysRevC.89.024312> (2 Feb. 2014).
48. Nikšić, T., Vretenar, D. & Ring, P. Relativistic nuclear energy density functionals: Adjusting parameters to binding energies. *Phys. Rev. C* **78**, 034318. <https://link.aps.org/doi/10.1103/PhysRevC.78.034318> (3 Sept. 2008).
49. Hilaire, S. & Girod, M. Large-scale mean-field calculations from proton to neutron drip lines using the D1S Gogny force. *Eur. Phys. J. A* **33**, 237–241. <https://link.springer.com/article/10.1140/epja/i2007-10450-2> (2007).
50. Brookhaven National Nuclear Data Center. <http://www.nndc.bnl.gov>.
51. Butler, P. A. & Nazarewicz, W. Intrinsic reflection asymmetry in atomic nuclei. *Rev. Mod. Phys.* **68**, 349–421. <https://link.aps.org/doi/10.1103/RevModPhys.68.349> (2 Apr. 1996).
52. Hohenberg, P. & Kohn, W. Inhomogeneous Electron Gas. *Phys. Rev.* **136**, B864–B871. <https://link.aps.org/doi/10.1103/PhysRev.136.B864> (3B Nov. 1964).
53. Kohn, W. & Sham, L. J. Self-Consistent Equations Including Exchange and Correlation Effects. *Phys. Rev.* **140**, A1133–A1138. <https://link.aps.org/doi/10.1103/PhysRev.140.A1133> (4A Nov. 1965).
54. Zhao, J., Lu, B.-N., Zhao, E.-G. & Zhou, S.-G. Tetrahedral shapes of neutron-rich Zr isotopes from a multidimensionally constrained relativistic Hartree-Bogoliubov model. *Phys. Rev. C* **95**, 014320. <https://link.aps.org/doi/10.1103/PhysRevC.95.014320> (1 Jan. 2017).

55. Lu, B.-N., Zhao, J., Zhao, E.-G. & Zhou, S.-G. Multidimensionally-constrained relativistic mean-field models and potential-energy surfaces of actinide nuclei. *Phys. Rev. C* **89**, 014323. <https://link.aps.org/doi/10.1103/PhysRevC.89.014323> (1 Jan. 2014).
56. Li, Z. P., Nikšić, T., Vretenar, D., Ring, P. & Meng, J. Relativistic energy density functionals: Low-energy collective states of  $^{240}\text{Pu}$  and  $^{166}\text{Er}$ . *Phys. Rev. C* **81**, 064321. <https://link.aps.org/doi/10.1103/PhysRevC.81.064321> (6 June 2010).
57. Lu, B.-N., Zhao, E.-G. & Zhou, S.-G. Potential energy surfaces of actinide nuclei from a multidimensional constrained covariant density functional theory: Barrier heights and saddle point shapes. *Phys. Rev. C* **85**, 011301. <https://link.aps.org/doi/10.1103/PhysRevC.85.011301> (1 Jan. 2012).
58. Lu, B.-N., Zhao, J., Zhao, E.-G. & Zhou, S.-G. Multidimensionally constrained relativistic mean field model and applications in actinide and transfermium nuclei. *Physica Scripta* **89**, 054028. <https://dx.doi.org/10.1088/0031-8949/89/5/054028> (Apr. 2014).
59. Talmi, I. *Simple Models of Complex Nuclei* (Routledge, London, UK, 1993).
60. Iachello, F. *Lie Algebras and Applications* in (2006). <https://api.semanticscholar.org/CorpusID:118332519>.
61. Kota, V. K. B., Van der Jeugt, J., De Meyer, H. & Vanden Berghe, G. Group theoretical aspects of the extended interacting boson model. *Journal of Mathematical Physics* **28**, 1644–1652. ISSN: 0022-2488. eprint: [https://pubs.aip.org/aip/jmp/article-pdf/28/7/1644/19126962/1644\\\_1\\\_online.pdf](https://pubs.aip.org/aip/jmp/article-pdf/28/7/1644/19126962/1644\_1\_online.pdf). <https://doi.org/10.1063/1.527471> (July 1987).
62. Devi, Y. D. & Kota, V. K. B. sdg Interacting boson model: hexadecupole degree of freedom in nuclear structure. *Pramana - J. Phys.* **39**, 413–491. <https://link.springer.com/article/10.1007/BF02847336> (5 Nov. 1992).
63. Kota, V. K. B. & Devi, Y. D. in *Symmetries in Science VII: Spectrum-Generating Algebras and Dynamic Symmetries in Physics* (eds Gruber, B. & Otsuka, T.) 307–327 (Springer US, Boston, MA, 1993). ISBN: 978-1-4615-2956-9. [https://doi.org/10.1007/978-1-4615-2956-9\\_28](https://doi.org/10.1007/978-1-4615-2956-9_28).
64. Akiyama, Y. sdg boson model in the SU(3) scheme. *Nuclear Physics A* **433**, 369–382. ISSN: 0375-9474. <https://www.sciencedirect.com/science/article/pii/0375947485902714> (1985).

65. Van Isacker, P., Bouldjedri, A. & Zerguine, S. Phase transitions in the sdg interacting boson model. *Nucl. Phys. A* **836**, 225–241. ISSN: 0375-9474. <https://www.sciencedirect.com/science/article/pii/S0375947410002952> (2010).
66. Zerguine, S., Van Isacker, P. & Bouldjedri, A. Consistent description of nuclear charge radii and electric monopole transitions. *Phys. Rev. C* **85**, 034331. <https://link.aps.org/doi/10.1103/PhysRevC.85.034331> (3 Mar. 2012).
67. Ginocchio, J. N. & Kirson, M. W. Relationship between the Bohr collective Hamiltonian and the interacting-boson model. *Physical Review Letters* **44**, 1744–1747. <https://api.semanticscholar.org/CorpusID:122888867> (1980).
68. Dieperink, A. E. L., Scholten, O. & Iachello, F. Classical Limit of the Interacting-Boson Model. *Phys. Rev. Lett.* **44**, 1747–1750. <https://link.aps.org/doi/10.1103/PhysRevLett.44.1747> (26 June 1980).
69. Gilmore, R. The classical limit of quantum nonspin systems. *Journal of Mathematical Physics* **20**, 891–893. ISSN: 0022-2488. eprint: [https://pubs.aip.org/aip/jmp/article-pdf/20/5/891/19327658/891\\\_1\\\_online.pdf](https://pubs.aip.org/aip/jmp/article-pdf/20/5/891/19327658/891\_1\_online.pdf). <https://doi.org/10.1063/1.524137> (May 1979).
70. Bohr, A. & Mottelson, B. Features of Nuclear Deformations Produced by the Alignment of Individual Particles or Pairs. *Physica Scripta* **22**, 468–474. <https://api.semanticscholar.org/CorpusID:121043288> (1980).
71. Ginocchio, J. & Kirson, M. An intrinsic state for the interacting boson model and its relationship to the Bohr-Mottelson model. *Nuclear Physics A* **350**, 31–60. ISSN: 0375-9474. <https://www.sciencedirect.com/science/article/pii/0375947480903875> (1980).
72. Van Isacker, P. & Chen, J.-Q. Classical limit of the interacting boson Hamiltonian. *Phys. Rev. C* **24**, 684–689. <https://link.aps.org/doi/10.1103/PhysRevC.24.684> (2 Aug. 1981).
73. Rohozinski, S. G. & Sobiczewski, A. Hexadecapole nuclear potential for non-axial shapes. *Acta Physica Polonica Series B* **12**, 1001–1007. ISSN: 0587-4254. [http://inis.iaea.org/search/search.aspx?orig\\_q=RN:16069947](http://inis.iaea.org/search/search.aspx?orig_q=RN:16069947) (1981).
74. Nazarewicz, W. & Rozmej, P. On the hexadecapole anomaly at the border of the rare earth region. *Nuclear Physics A* **369**, 396–412. ISSN: 0375-9474. <https://www.sciencedirect.com/science/article/pii/0375947481900270> (1981).
75. Heinze, S. computer program ARBMODEL, University of Cologne (2008). 2008.

76. Lotina, L. & Nomura, K. Microscopic description of hexadecapole collectivity in even-even rare-earth nuclei near  $N = 90$ . *Phys. Rev. C* **109**, 044324. <https://link.aps.org/doi/10.1103/PhysRevC.109.044324> (4 Apr. 2024).
77. Ganiev, E., Wyss, R. & Magierski, P. Properties of  $N = 90$  isotones within the mean field perspective. *Phys. Rev. C* **89**, 014311. <https://link.aps.org/doi/10.1103/PhysRevC.89.014311> (1 Jan. 2014).
78. Kumar, C. V. N. & Robledo, L. M. Hexadecapole axial collectivity in the rare earth region: A beyond-mean-field study. *Phys. Rev. C* **108**, 034312. <https://link.aps.org/doi/10.1103/PhysRevC.108.034312> (3 Sept. 2023).
79. Lotina, L. & Nomura, K. Impacts of hexadecapole deformations on the collective energy spectra of axially deformed nuclei. *Phys. Rev. C* **109**, 034304. <https://link.aps.org/doi/10.1103/PhysRevC.109.034304> (3 Mar. 2024).
80. Dinh, T. K., Grinberg, M. & Stoyanov, C. Interplay of collective and noncollective modes in low-lying quadrupole states of  $^{140}\text{Ba}$ ,  $^{142}\text{Ce}$ ,  $^{144}\text{Nd}$  and  $^{146}\text{Sm}$ . *Journal of Physics G: Nuclear and Particle Physics* **18**, 329. <https://dx.doi.org/10.1088/0954-3899/18/2/014> (Feb. 1992).
81. Kibédi, T. & Spear, R. Electric monopole transitions between  $0+$  states for nuclei throughout the periodic table. *Atomic Data and Nuclear Data Tables* **89**, 77–100. ISSN: 0092-640X. <https://www.sciencedirect.com/science/article/pii/S0092640X04000488> (2005).



# Curriculum vitae

Luka Lotina was born in 1996 in Zadar (Croatia). He obtained his Master's Degree from the University of Zagreb in 2020. The thesis was titled 'Microscopic description of nuclear shapes and collective excitations' and the research was carried under the supervision of dr. sc. Kosuke Nomura at the Physics Department of the University of Zagreb as a part of the Tenure Track Pilot Programme 'Exotic Nuclear Structure and Dynamics' (TTP-2018-07-3554). As of November 2020, Luka Lotina is a doctoral student at the University of Zagreb, doing the research under the supervision of dr. sc. Kosuke Nomura. Together with dr. sc. Kosuke Nomura, he has co-authored 4 papers, listed below.

## Refereed publications

### Published

- 1 Nomura, K., **Lotina, L.**, Nikšić, T., Vretenar, D., 2021, Phys. Rev. C, **103**, 054301, *Microscopic description of octupole collective excitations near  $N = 56$  and  $N = 88$*
- 2 Nomura, K., **Lotina, L.**, Rodríguez-Guzmán, R., Robledo, L. M., 2022, Phys. Rev. C, **106**, 064304, *Simultaneous description of  $\beta$  decay and low-lying structure of neutron-rich even- and odd-mass Rh and Pd nuclei*
- 3 **Lotina, L.**, Nomura, K., 2024, Phys. Rev. C, **109**, 034304, *Impacts of hexadecapole deformations on the collective energy spectra of axially deformed nuclei*
- 4 **Lotina, L.**, Nomura, K., 2024, Phys. Rev. C, **109**, 044324, *Microscopic description of hexadecapole collectivity in even-even rare-earth nuclei near  $N = 90$*